Magnetotelluric Exploration in the Rocky Mountain Foothills, Alberta

by

Wen Xiao

A thesis submitted to the Faculty of Graduate Studies and Research in partial fulfillment of the requirements for the degree of Master of Science in geophysics

Department of Physics

UNIVERSITY OF ALBERTA

Edmonton, Alberta

Fall 2004

Abstract

A magnetotelluric (MT) survey was carried out to test the possibility of imaging the complex geological structures in the Rocky Mountain Foothills with this geophysical method. This thesis provides a brief introduction to the geological structure of the Rocky Mountain Foothills and the magnetotelluric method. Details of the MT data acquisition, processing, modeling and interpretation are then described.

Magnetotelluric data were collected at a total of 26 stations in 2002. The Time series were processed using standard techniques with a remote magnetic reference. The Tensor decomposition technique was used to analyze the dimensionality of the MT data, and the static shifts were corrected. The frequency domain apparent resistivity and phase data were then converted into a model of electrical resistivity and depth with a two dimensional inversion algorithm.

The resistivity model shows that the Alberta Basin is characterized by low resistivity sedimentary rocks. These form the footwall of the Brazeau Thrust and extend 10 km west beneath the overthrust Paleozoic Carbonates. The geometry of the MT model agrees well with that derived from the seismic reflection data. The study shows that MT data is a useful tool for exploration in this environment.

Acknowledgements

I would like to thank my supervisor Professor Martyn Unsworth for his supporting and advice in this research. Comments from Wolfgang Soyer are gratefully acknowledged. Enthusiastic field help from Qingyun Di, Natalia Gomez, Damien Meilleux, Flora Paganelli, Shah Shareef, Wolfgang Soyer and Alex Walcott was greatly appreciated. Thanks to Maja Bueshkuelhe who assisted me in obtained well log information. Thanks to Phoenix Geophysics (Toronto) for technical assistance and the loan of additional MT instrumentation for the fieldwork.

Table of Contents

Chapter 1--- Introduction……..……..…....…...15

1.1 Geological Background of the Rocky Mountain Foothills……..15

1.1.1 General Introduction……..……...15

1.1.2 Evolution of Cordillera and the Western Canada Sedimentary Basin……...…16

1.1.3 Stratigraphy and Structural styles in the Foothills……19

1.2 Petroleum exploration in the Western Canadian Sedimentary Basin and the Foothills……..……..……..…22

1.2.1 Hydrocarbon potential of the WCSB and the Foothills…….……22

1.2.2 Geophysical methods used in the Rocky Mountain Foothills' exploration……...……25

Chapter 2 --- Introduction to the magnetotelluric method……..28

2.1 General Introduction……28

2.2 Introduction of equations……30

2.3 Two dimension magnetotelluric method……35

2.4 Tensor decomposition……39

2.5 Static shifts……42

Chapter 3 --- Application of the magnetotelluric method in hydrocarbon exploration……...45

3.1 The application of MT method in oil and gas exploration in early stage……....46

3.2 Recent technique development of MT method and its application in

hydrocarbon exploration……47

Chapter 4 --- Magnetotelluric data acquisition and Processing……52

4.1 Magnetotelluric data collection……52
4.2 Magnetotelluric time series analysis……...55
4.3 Tensor Decomposition……..56
4.4 MT sounding curves and pseusosections……..59
4.5 Static Shift Correction……65

Chapter 5 --- Inversion of MT data and sensitivity tests……...…69

5.1 Inversion of MT data……..69
5.2 Inversion of the Foothills MT data…..……...71
5.3 Inversion model smoothness test…..……...78
5.4 Other inversion models……79
5.5 Testing of features in the inversion model……..82

Chapter 6 --- Interpretation of the Foothills MT resistivity model……..……..88

6.1 Introduction……..……88
6.1.1 Regional Geology……...…88
6.1.2 Well logs and seismic data……92
6.2 Comparison with well logs……..……92
6.3 Interpretation……94
6.3.1 Alberta Basin……..……94
6.3.2 Triangle zone……..95
6.3.3 Brazeau Thrust Fault……97

Chapter 7 --- Conclusion, discussion and future work……..103

Bibliography……..……105

List of Tables

Table 1-1 Foothills' Stratigraphic (modified from Fox, 1959)……..20

Table 5-1 Model Inversion parameters……..72

Table 5-2 Model Inversion parameters……...80

Table 6-1 Geological divisions of well logs (data show the elevation of the bottom of the geological units)……...90

List of Figures

Figure 1-1: The structural elements of the Western Canadian Sedimentary Basin. The green lines show the geological cross section in the Figure 1-3: H-Highwood River Section, S-Sukunka River Section, TM-Tuchodi-Muskwa section. White line (MT) shows the location of the magnetotelluric survey. (Modified from Mossop & Shetsen, Geological Atlas of the WCSB, Chapter 3, 1994)……..…….18

Figure 1-2: Geological map of southern Alberta. The red line shows the location the magnetotelluric survey (modified from Geological Map of Alberta (1999); scale: 1:1,000,000; Alberta Geological Survey/Alberta Energy and Utility Board)……...18

Figure 1-3: Structural style in the Rocky Mountain Foothills (Wright et al., 1994). Locations of the profiles are shown in Figure 1-1…….23

Figure 1-4: Geological distribution of reserves of conventional crude oil (Burrowes, 2003)…….25

Figure 1-5: Resistivity log of Well: 00/05-13-037-12W5-0. Depth is below mean sea level. Location of the well is shown in Figure 4-1 (GeoWell General Well Standard Report, Alberta Geological Survey/Alberta Energy and Utility Board)..……27

Figure 2-1: Electrical resistivity of rocks (from Martyn Unsworth, Geophysics 424, at the University of Alberta)……..29

Figure 2-2: Skin depth as a function of the frequency of the MT signal and the resistivity of the Earth……32

Figure 2-3: Example of apparent resistivity and phase for a 1-D MT model……34

Figure 2-4: Configuration of EM fields for a two-dimensional geoelectric structure……..……37

Figure 2-5: The geometry of the vertical component of magnetic fields associated with TE mode electric currents flowing in a buried low resistivity body. Arrows in plan view show the induction vectors. Arrows in vertical section show directions of magnetic field components (Martyn Unsworth, Geophysics 424, University of Alberta)…….38

Figure 2-6: Sketch of the model used to explain static effects. The middle apparent resistivity curve is that which would be observed if the inlier had the same resistivity as the layer (Vozoff, 1991)……42

Figure 2-7: DC-limit (zero frequency) TM electric field response of the surface low resistivity body. ρ_1=0.5(Ωm), ρ_2=20(Ωm); The lower diagram depicts how a laterally uniform conduction current is bent upward and channeled through the surface low resistivity body. This channeling effect is manifested on the surface as the surge of secondary electric field with positive and negative lateral variations across the low resistivity body, as shown in the upper curve. Because of Faraday's Law, an average of these lateral variations will tend to zero as the observations of the electric field are extended infinitely away from the low resistivity body (Torres-Verdin and Bostick, 1992)……44

Figure 3-1: (a), Schematic cross section, based on regional well control. Elevation in kilometers. (b), Seismic section corresponding to the central part of (a). The letter A denotes the target Mardin reflector that can be identified in seismic section. (c), two-dimensional inversion of MT data (gray scale). White line represents seismic reflectors. Crossbar on well shows top of Mardin group. Inverted triangles are MT stations. Vertical scale is elevation in meters; horizontal scale is in kilometers (Watts and Pince, 1998)……..…49

Figure 4-1: Location of MT sites and well logs used in the study. Black dots denote locations of MT sites, red dots denote locations of the well logs that are used in Chapter 6. The rose diagram shows the regional geoelectric strike (frequency band: 100-0.01 Hz) determined by tensor decomposition (McNeice and Jones, 2001)……52

Figure 4-2: Geological map of study area. MM' shows the location of MT profile, blue dots show locations of the MT stations; NN' shows the location of the Nordegg Area Geological Cross Section used in Figure 6-1 (modified from Geological Map of Alberta, Alberta Geological Survey/Alberta Energy and Utility Board)…..……53

Figure 4-3: Configuration of a broadband MT recording system.……54

Figure 4-4: The geoelectric strike of the whole frequency band data at each station from the decomposition analysis. Red line shows the location of the Brazeau Thrust Fault. Dots show site locations, length of lines is inversely proportional to r.m.s misfit…….57

Figure 4-5: Shear angle, twist angle, geoelectric strike and r.m.s. misfit from the decomposition analysis of the whole frequency band of each station. The angles are in degrees clockwise from North. The red line shows the location of the Brazeau Thrust Fault……..…58

Figure 4-6: Comparison of MT data before and after tensor decomposition……60

Figure 4-7: MT data after decomposition and rotation. TE mode data are shown in red and TM mode data are shown in blue……..…64

Figure 4-8: Comparison of pseudosections of TE and TM modes. (a): Pseudosections of data after tensor decomposition but before static shifts correction. (b): data after tensor decomposition and static shift correction……..65

Figure 4-9: Comparison of apparent resistivity at the highest frequency (100 Hz). Solid line shows the apparent resistivity of highest frequency of the data before rotated to the regional geoelectric strike coordinate frame and static shift correction; Dashed line shows the apparent resistivity of highest frequency of the data after rotation to the regional geoelectric strike coordinate frame and static shift correction. The corrected MT data has been first rotated by tensor decomposition analysis…….67

Figure 5-1: (a) The optimal inversion model. Triangles at the surface with numbers on the top indicate the location of MT sites. BTF=Brazeau Thrust Fault. (b) r.m.s. misfit as a function of station number. Dashed line shows the ideal fit, red line shows location of the Brazeau Thrust Fault……73

Figure 5-2: Sounding curves and model response of MT stations. Solid line shows the model response, and dots with error bars show the observed data…76

Figure 5-3: (a), the inversion model; (b), the apparent resistivity data and the inversion model response of the TE mode; (c), the phase data and the inversion model response of the TE mode; (d), the apparent resistivity data and the inversion model response of the TM mode; (e), the phase data and the inversion model response of the TM mode. (f), the residuals in the TE mode apparent resistivity and phase data; (g), the residuals in TM mode apparent resistivity and phase data. The residual is the difference between the model response and the data normalized by the standard error. The white blocks indicate where there is no data…….77

Figure 5-4: Inversion models with different τ values……78

Figure 5-5: Variation of r.m.s. misfit with τ……79

Figure 5-6: Comparison of inversion models with different control parameters. BTF=Brazeau Thrust Fault. (a) is the prefered model that will be used in the interpretation……..…….81

Figure 5-7: The distinct resistivity features in the MT Inversion model……..82

Figure 5-8: Comparison between Forward Model D and the inversion model. Solid line is the responses of the inversion model, dash line is the responses of the forward model D. Dots with error bar is the measured MT data. The r.m.s misfit of station FH011 increases from 1.68 to 2.06. The r.m.s misfit of station FH001 increases from 1.28 to 2.95…….83

Figure 5-9: Comparison between Forward Model C and the inversion model. Solid line is the responses of the inversion model, dash line is the responses of the forward model C. Dots with error bar is the measured MT data. The r.m.s misfit of station FH002 increases from 1.41 to 3.57. The r.m.s misfit of station FH010 increases from 1.39 to 3.61…….84

Figure 5-10: Comparison between Forward Model B and the inversion model. Solid line is the responses of the inversion model, dash line is the responses of the forward model B. Dots with error bar is the measured MT data. The r.m.s misfit of station FH010 increases from 1.39 to 2.89. The r.m.s misfit of station FH004 increases from 1.49 to 2.73. The r.m.s misfit of station FH006 increases from 1.35 to 1.97……..85

Figure 5-11: Comparison between Forward Model E and the inversion model. Solid line is the responses of the inversion model, dash line is the responses of the forward model E. Dots with error bar is the measured MT data. The r.m.s

misfit of station FH016 increases from 1.41 to 3.57. The r.m.s misfit of station FH017 increases from 1.39 to 4.70. The r.m.s misfit of station FH018 increases from 1.49 to 2.32. The decrease of the fit of model responses to data with the decrease of the resistivity of feature E in the forward model shows that the feature E in the inversion model is reliable…….86

Figure 6-1: Comparison of the geological cross section, MT inversion model and well logs. (a): Nordegg area cross section from Langenberg and Kubll (2002); CF=Coliseum Fault; BRF=Brazeau Range Fault; BTF=Brazeau Thrust Fault; ATF= Ancona Trust Fault; SA= Stolberg Anticline; Tp=Paskapoo Formation; Kw=Wapiabi Formation; Kbc=Blackstone and Cardium Formations; KL=Lower Cretaceous; M=Mississippian; D=Devonian; Ca=Cambrian; (b): A, B, C, D and E denote resistivity features in the MT inversion model that are discussed in this chapter. (c): well data from Alberta Energy and Utility Board (EUB). Geological divisions are based on Geowell General Well Standard Report from EUB; actual data are shown in Table 6-1…….89

Figure 6-2: Seismic time section. Red lines denote faults; yellow lines denote interface between geological units. BTF=Brazeau Thrust Fault; BKF=Back Thrust Fault; A1=Anticline 1; A2=Anticline 2; S=Syncline. The depth in seismic section is converted from time with the velocity model from Lawton et al. (1996)…….91

Figure 6-3: Comparison of resistivity logs (solid lines) and the MT derived resistivity model (dashed lines) at two wells. The depth is relative to sea level. White lines in the inversion model show the locations of the wells. BTF=Brazeau Thrust Fault; A1= Anticline 1; A2= Anticline 2; S= Syncline…….93

Figure 6-4: Detailed comparison between Inversion model and seismic time section-Triangle Zone. BTF=Brazeau Thrust Fault; BKF=Back Thrust Fault; A1= Anticline 1; A2= Anticline 2; S= Syncline; Red lines denote faults, yellow lines

denote interfaces between geological units. The depth in seismic section is converted from time by the velocity model from Lawton et al. (1996)……...96

Figure 6-5: Synthetic test for model sensitivity below the low resistivity anticline A1. Different values of resistivity were used in the model beneath the low resistivity anticline. 5% Gaussian noise was added to the forward model responses. The r.m.s. misfits are: model 1: initial: 15.03; final: 0.882; model 2: initial: 11.91; Final: 0.897. The inversion results show that resolution of the model below the anticline A1 is poor……..……..97

Figure 6-6: Detailed comparison between MT inversion model and seismic time section. BTF=Brazeau Thrust Fault; Red lines denote faults, yellow lines denote interfaces between geological units…….98

Figure 6-7: Synthetic test for the dip angle of the Brazeau thrust fault. Left-synthetic resistivity models with different dips; Right-inversion results. Noise was added into the forward responses of the synthetic resistivity models before inversion. Red line shows the actual dip angle of the thrust fault in the synthetic models. R.m.s. misfit of 30° dipping anglemodel: initial: 5.03; final: 0.882. R.m.s. misfit of 45° dipping angle model: initial: 14.71; final: 0.985. The inversion results show that the inversion recovers the dip angle of the thrust fault reliably……99

Chapter 1

Introduction

The Rocky Mountain Foothills in Alberta are located between the Western Canadian Sedimentary Basin (WCSB) and the Rocky Mountains. This fold and thrust belt was formed by shortening of the Paleozoic and the Mesozoic rocks in late Jurassic to Eocene as terrane accretion occurred on the western margin of North America. Within the Foothills, structural shortening has been accommodated primarily by thrust faulting (Price, 1994; Wright et al, 1994; and references therein).

The Rocky Mountain Foothills are the focus of ongoing hydrocarbon exploration in Western Canada. To date, most geophysical exploration in the Rocky Mountain Foothills has used seismic exploration and has yielded clear images of three-dimensional structures. However the complicated geology and rugged terrain in the Rocky Mountain Foothills presents some challenges for the seismic method. Can other exploration methods be used in the Foothills? The large resistivity contrast between the Paleozoic carbonates and the Mesozoic clastic sedimentary rocks is potentially favorable for the magnetotelluric (MT) method. An MT survey was carried out in 2002 to test the ability of MT data to image structures in the Rocky Mountain Foothills.

1.1 Geological Background of the Rocky Mountain Foothills

1.1.1 General Introduction

The western margin of the WCSB has had a long tectonic history. This was dominated by extension from the Proterozoic to the Triassic, and compressive deformation from the Middle Jurassic to the Eocene (Wright et al, 1994). The compressive tectonic movements caused significant shortening of the western

margin of WCSB and created both the Rocky Mountains and the Foothills (Wright et al, 1994).

The tectonic setting has controlled the stratigraphy of the Rocky Mountain Foothills. The Paleozoic succession is composed mainly of marine carbonate sediments. Clastic sediments, such as shales, siltstones, and sandstones dominate the Mesozoic succession (Wright et al, 1994). Due to the intense compressive deformation, overthrust faults and folds developed in the Rocky Mountain Foothills. The structures in the Foothills are very complex, and different structural styles have developed due to varying lithology. Generally, a northward change in structural style from thrust-dominated in the south, to fold-dominated in the north can be observed (Wright et al, 1994). This is consistent with the general trend of a northward decrease in the competency of the entire Phanerozoic sedimentary sequence in the Foothills.

1.1.2 Evolution of the Canadian Cordillera and the Western Canada Sedimentary Basin

The Western Canada Sedimentary Basin (WCSB) is a northeastward-tapering wedge of supracrustal rocks overlying the Precambrian crystalline basement, which form the core of the North American Continent. The thickness of this sedimentary wedge increases gradually southwestward, over a distance of 600 to 1200 km, from zero at the exposed margin of the Canadian Shield, to between 3 and 5 km at the northeastern margin of the foreland thrust and fold belt (Wright et al, 1994; Figure 1-1).

The origin and evolution of the WCSB is linked inextricably to the origin and evolution of the Canadian Cordillera, thereby to global plate tectonic processes. The evolution of the WCSB can be divided into two main stages, (1) the Late Proterozoic to Triassic Miogeocline-platform stage and (2) the Jurassic to early Eocene foreland basin stage. A set of marine shales and carbonate sedimentary

rocks that were related to continental rifting developed during (1). This continental rifting created the initial Cordilleran continental margin of the North American Continent and its adjacent ocean basin. Subsequently, a continental terrace wedge (miogeocline) developed, which prograded outboard from this passive margin (Price, 1994).

The foreland basin stage began in the Late Jurassic with the accretion of a tectonic collage of allochthonous terranes, due to the convergence of the Pacific and North American Plates. During this stage, as a result of oblique collision between the accreted terranes and the North American craton, the outboard part of the miogeocline-platform supracrustal wedge was detached from its basement, displaced northeastward, compressed and thickened. The weight of the displaced and tectonically thickened supracrustal rocks induced subsidence of the foreland basin, and the associated uplift and erosion provided much of the sediments that accumulated in the foreland basin. The pattern of growth of the foreland fold and thrust belt, and of the foreland basin component of the supracrustal wedge, were effectively terminated by an episode of Eocene crustal extension in the central part of the Cordillera. The emerging Cordilleran mountain belt provided the source of clastic sediments for the Mesozoic succession during this stage (Price, 1994).

The present-day WCSB comprises the eastern Canadian Cordillera and two major sedimentary basins: the Alberta Basin and the Williston Basin. The Alberta Basin is a northwest-trending trough on the east side of the Canadian Cordillera. The Rocky Mountain Foothills is the elongated belt between the Rocky Mountains and the Alberta Basin (Figure 1-1). It is about 400 km long and 20-40 km wide. It has three geographic subdivisions. The southern part extends from the US-Canada border to the Bow River, the central part between the Bow and Athabasca Rivers, and the northern part extends from the Athabasca River to the British Columbia border. The MT survey described in this thesis is located in the

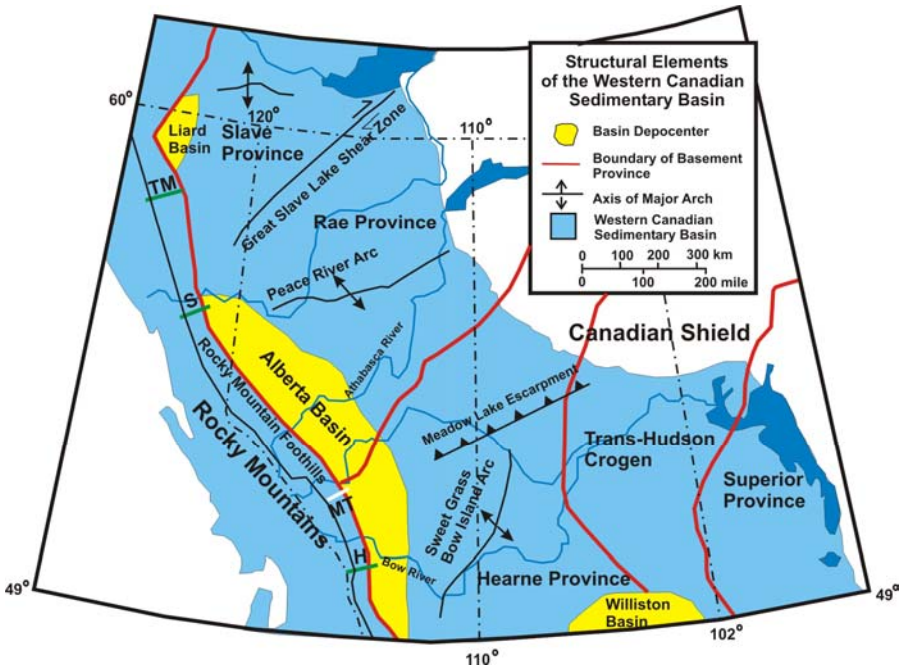

Figure 1-1: The structural elements of the Western Canadian Sedimentary Basin. The green lines show the geological cross section in the Figure 1-3: **H**-Highwood River Section, **S**-Sukunka River Section, **TM**-Tuchodi-Muskwa section. White line (**MT**) shows the location of the magnetotelluric survey. (Modified from Mossop & Shetsen, Geological Atlas of the WCSB, Chapter 3, 1994)

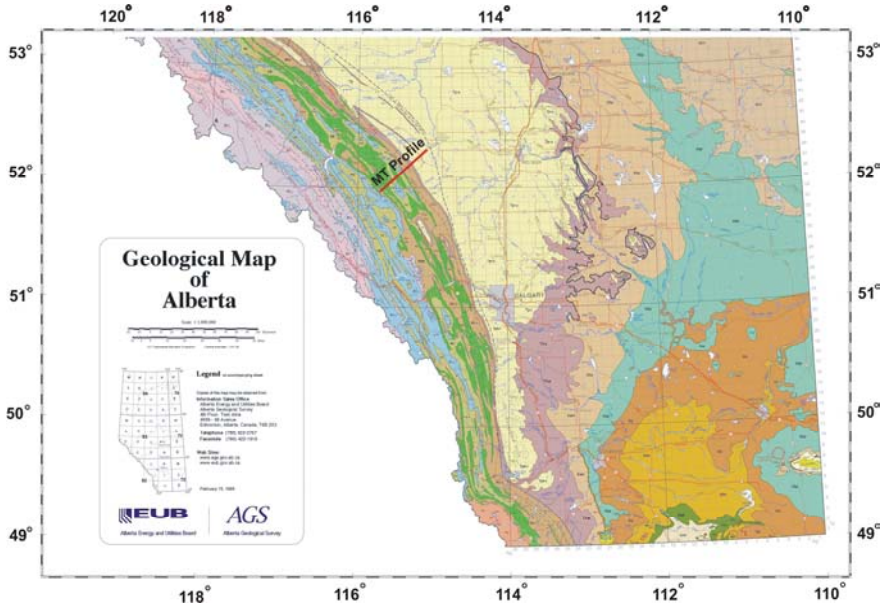

Figure 1-2: Geological map of southern Alberta. The red line shows the location the magnetotelluric survey (modified from Geological Map of Alberta (1999); scale: 1:1,000,000; Alberta Geological Survey/Alberta Energy and Utility Board).

southern central Foothills and extends from the Alberta Basin to the Rocky Mountain Front Ranges (Figure 1-1 and 1-2).

1.1.3 Stratigraphy and structural styles in the Foothills

The geological formations exposed in the Foothills range in age from the Mississippian to the Paleocene, and from wells it is known that in the subsurface there are rocks of Devonian to Cambrian age. These formations have been described in detail in many publications, and the stratigraphic succession is well established (Table 1; Fox, 1959). Generally the formations are thicker in the western Foothills than in the east. The maximum aggregate thickness represented above the Proterozoic basement is about 9000 m (Fox, 1959).

Foreland Fold and Thrust Belt in the Cordillera was formed by the Middle Jurassic to Eocene deformation of the western edge of WCSB. The competency of the existing strata has had a significant influence on the structural style. Generally, thick, competent carbonate or sandstone successions are easy to break and favour the development of thick thrust sheets. Less competent interlayered shale and sandstone, or shale and carbonate successions are easy to deform and favour the formation of folds between detachments. Several formations have evidently played a leading role in the structural evolution of the Foothills by serving as weak detachments that developed into the major thrust faults. Five major detachments have been observed in the Foothills. The two most striking detachments exist in the Fernie and Kootenay formations and the Blackstone Formation. The other three exist in the Banff Formation, Wapiabi Formation and Cambrian sequence (Fox, 1959).

The lithological character of the deformed stratigraphic sequence controls the structural style of the fold and thrust belt. A change in structural style from thrust-dominated in the south to fold-dominated in the north reflects facies changes

Table 1-1 Foothills' Stratigraphy (modified from Fox, 1959)

System	Formation	Thickness (m)	Lithological Description
Tertiary Paleocene	Paskapoo-Porcupine Hills	610	Sandstone, shale, mudstone, thin coal seams, cobble bed at base
-- -- -- -- -- -- -- -- -- -- -- -- -- -- -- -- Unconformity -- -- -- -- -- -- -- -- -- -- -- -- -- -- -- -- -- --			
	Willow Creek	30—250	Sandstone, shale, mudstone
Cretaceous Upper	Edmonton	300—460	Sandstone, shale, and coal, conglomeratic at base in places
	Bearpaw	0—180	Shale, siltstone, with thin sandstone beds
	Belly River	70—1220	Sandstone, shale, some coal, basal sandstone very massive in places
	Wapiabi	30—550	Siltstone and shale
	Bighorn (Cardium)	10—140	Sandstone, arenaceous shale, lentils of chert conglomerate
	Blackstone	140—300	Siltstone and shale
	Crowsnest	0—550	Agglomerate, tuff, essentially confined to Crowsnest area
Lower	Blairmore	300—700	Sandstone, shale, some thin limestone, bentonitic, and tuffaceous beds
-- -- -- -- -- -- -- -- -- -- -- -- -- -- -- -- Unconformity -- -- -- -- -- -- -- -- -- -- -- -- -- -- -- -- -- --			
Cretaceous	Kootenay	15—210	Sandstone, Carbonaceous shale, and coal
Jurassic	Fernie	30—270	Siltstone, shale, and fine- grained sandstone
Triassic	Spray River	0—15	Dolomite and limestone
Permian	Rocky Mountain	0—120	Arenaceous dolomite, limestone, quartzitic sandstone, siltstone, basal conglomerate in some places.
Carboniferous Mississippian	Rundle group	270—610	Limestone, dolomite, some calcareous shale, commonly cherty, in places anhydritic
	Banff	150—270	Silty dark limestone, calcareous shale
	Exshaw	3—10	Black shale
-- -- -- -- -- -- -- -- -- -- -- -- -- -- -- -- -- -- Unconformity -- -- -- -- -- -- -- -- -- -- -- -- -- -- -- -- -- --			
Devonian	Palliser	200—350	Limestone, dolomite, characteristically Massive
	Alexo	30—60	Dolomite, silty to arenaceous
	Fairholme	410—530	Dolomite, limestone, argillaceous and silty limestone, anhydrite
	Ghost River	80+	Variegated shale, dense dolomite, edgewise conglomerate
-- -- -- -- -- -- -- -- -- -- -- -- -- -- -- -- -- -- Unconformity -- -- -- -- -- -- -- -- -- -- -- -- -- -- -- -- -- --			
Cambrian		780+	Limestone, dolomite, argillaceous limestone , with sandstone or quartzite at base
-- -- -- -- -- -- -- -- -- -- -- -- -- -- -- -- -- -- Unconformity -- -- -- -- -- -- -- -- -- -- -- -- -- -- -- -- -- --			
Proterozoic		3050+	Limestone, dolomite, argillite, quartzite, shale. Known only in Lewis overthrust sheet

within the Phanerozoic section and the general northward decrease in the competency of almost the entire section. A broad transition zone, with folds more common at the surface and thrust faults more common in the subsurface, occurs between the Athabasca River and the Williston Lake-Peace River area (Wright et al., 1994).

The Highwood River section (Gordy and Frey, 1975) in Figure 1-3 gives a typical example of the structural style in the southern Foothills. Northeast verging thrust faults in the Mesozoic and the Paleozoic strata characterize the section, where numerous thrust faults cut through the Mesozoic clastic strata but fewer faults cut through the Paleozoic strata. North of the Bow River, imbrication of the Mesozoic section is less intense. A triangle zone, or zone of underthrusting, occurs at the eastern limit of deformation along most of the southern Foothills (Jones, 1982). The east-dipping backward fault at the east side of the triangle zone constitutes the western limb of the Alberta Syncline along the western edge of the essentially undeformed Alberta Basin (Wright et al., 1994).

The Tuchodi-Muskwa section (Gabrielse and Taylor, 1982) shows that large amplitude box and chevron folds in the Upper Paleozoic and the Mesozoic strata characterize the structural expression of the northern Foothills. In contrast to the complex array of faults found in the southern Foothills, low amplitude folds, developed in the Upper Paleozoic to the Lower Cretaceous strata beneath the nearly flat lying Upper Cretaceous sandstone and shale. These folds occur up to 200 km east of the northern Foothills. The northern Foothills folds have formed above a regional detachment in a thick Upper Devonian and Mississippian shale succession. The underlying Devonian and older carbonates remained essentially undeformed across the eastern part of the northern Foothills. A few simple thrust faults are thought to deform these strata under the western part of the northern Foothills (Wright et al., 1994).

The transition zone between the thrust-dominated south and the fold-dominated north contains a variety of structural styles. To a large degree these reflect changes in the structural competency of the stratigraphic sequence. As the Sukunka River section shows, in the western Foothills the folded Lower Cretaceous strata at surface are separated by a detachment from the Triassic strata with a very different structural style of faulted folds and locally imbricated thrust complexes. The underlying Mississippian strata occur in relatively simple fault structures. In the eastern Foothills the structural style is quite different. Low amplitude box folds, which are formed by fault-bend folding and fault displacement transfer, occur beneath the barely deformed Upper Cretaceous and younger strata at the surface (Wright et al., 1994).

1.2 Petroleum exploration in the Western Canadian Sedimentary Basin and the Foothills

As one of the most prolific oil and gas-bearing basins in North America, the WCSB has a long history of hydrocarbon exploration and production. It has consequently become an area of ongoing research and exploration.

1.2.1 Hydrocarbon potential of the WCSB and the Foothills

The first hydrocarbon discovery in Alberta occurred in 1788, when Peter Pond noted the Lower Cretaceous McMurray Tar Sands (Greiner and Chi, 1995). The first commercial gas field was discovered in 1904 in Upper Cretaceous rocks at Medicine Hat on the southeastern plains. However, it was not until 1947, when oil was discovered in a Devonian reef at Leduc, that widespread exploration began in the province. The WCSB holds 86% of Canada's proven natural gas reserve, 81% of proven light crude oil reserves and nearly all the proven heavy oil and bitumen reserves. Furthermore, 98% of Canadian's cumulative natural gas

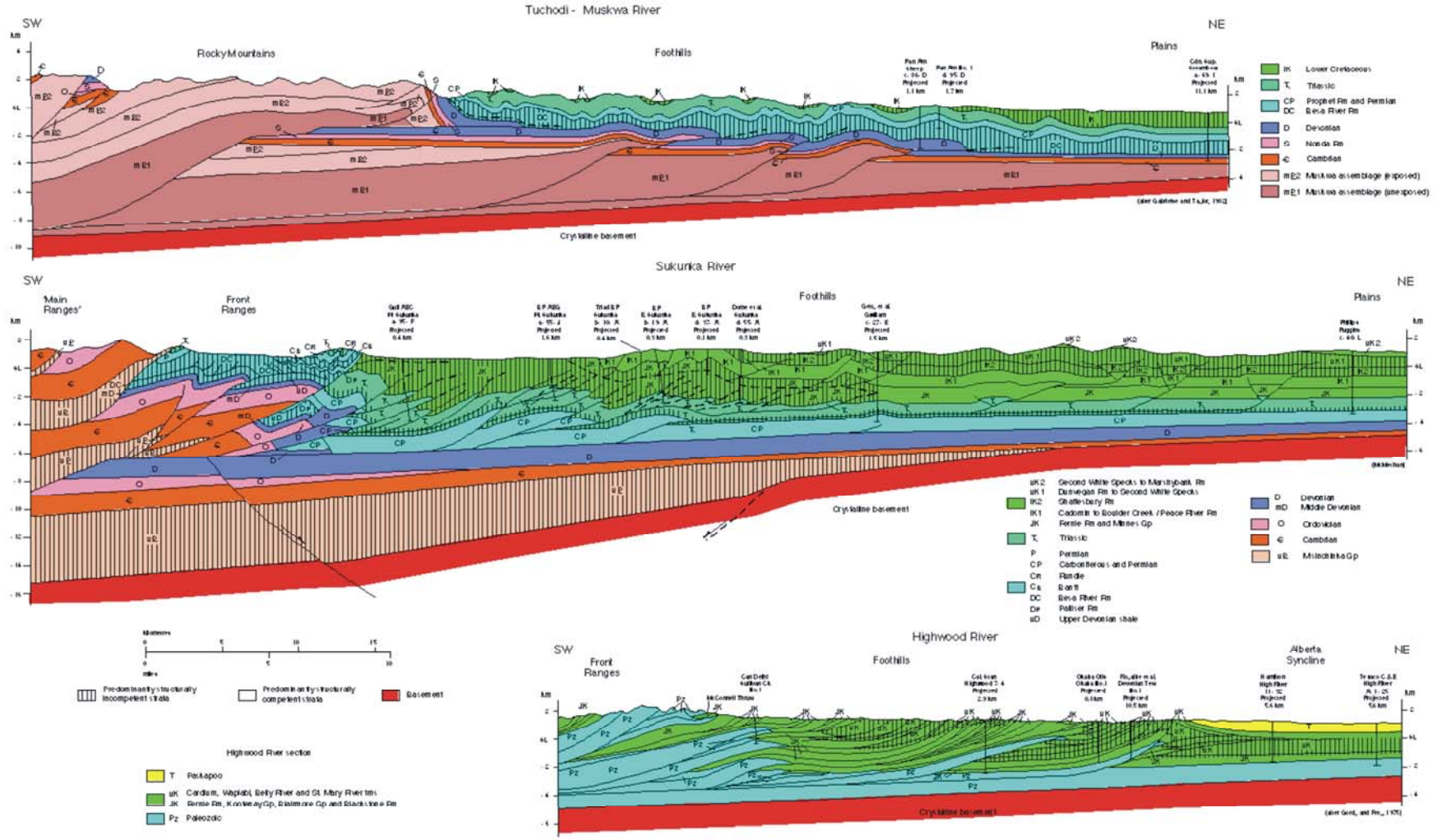

Figure 1-3: Structural style in the Rocky Mountain Foothills (Wright et al., 1994). Locations of the profiles are shown in Figure 1-1.

production and nearly all of the oil and bitumen production has occured here (Greiner and Chi, 1995).

Petroleum occurs in almost every formation of the WCSB, but the Devonian and the Cretaceous strata are the most important oil-bearing geological units. The Devonian contains 55% of Western Canada's light and medium oil potential. 90% of the Devonian reserves are found in Devonian reef complexes. The largest oil reserves have been found historically in the Leduc and Beaverhill Lake groups, but these are of lesser significance when production volumes are taken into account. The Cretaceous section contains 18% of the recoverable reserves of conventional oil in Western Canada and over 54% of Alberta's natural gas reserves. The Lower and Upper Cretaceous contain 13% and 25% respectively of the remaining recoverable oil and gas reserves in Alberta (Greiner and Chi, 1995). The largest Mesozoic oil accumulation in western Canada is in the Cardium formation. The Lower Cretaceous Mannville Group also contains the largest oil sands deposits. Production and reserve volumes of oil that were previously dominated by Devonian reef plays are being replaced by Cretaceous pools that are smaller, shallower and have a poorer recovery factor. Figure 1-4 shows the distribution of reserves of conventional crude oil in Alberta by geological period (Burrowes et. al, 2003).

As part of the WCSB, the Rocky Mountain Foothills has a long history of hydrocarbon exploration and production. Western Canada's first oil boom was initiated by the discovery of oil in 1914 at Turner Valley in the southern Foothills (Greiner and Chi, 1995). In contrast to the oil-bearing Alberta Basin, the Foothills is a prolific gas province. Up to 1995, about thirty gas fields have been developed in the Foothills, and their remaining reserves comprise at least 250 billion m^3 of gas and 1 mio.m^3 of oil (Greiner and Chi, 1995). With the increasing demand for natural gas, the Rocky Mountain Foothills has become one of the focus areas for gas exploration in North America. The Geological Survey of Canada estimates

that there is $2.35*10^{12}m^3$ of undiscovered gas in the Rocky Mountain Foothills (Stockmal et al., 2001).

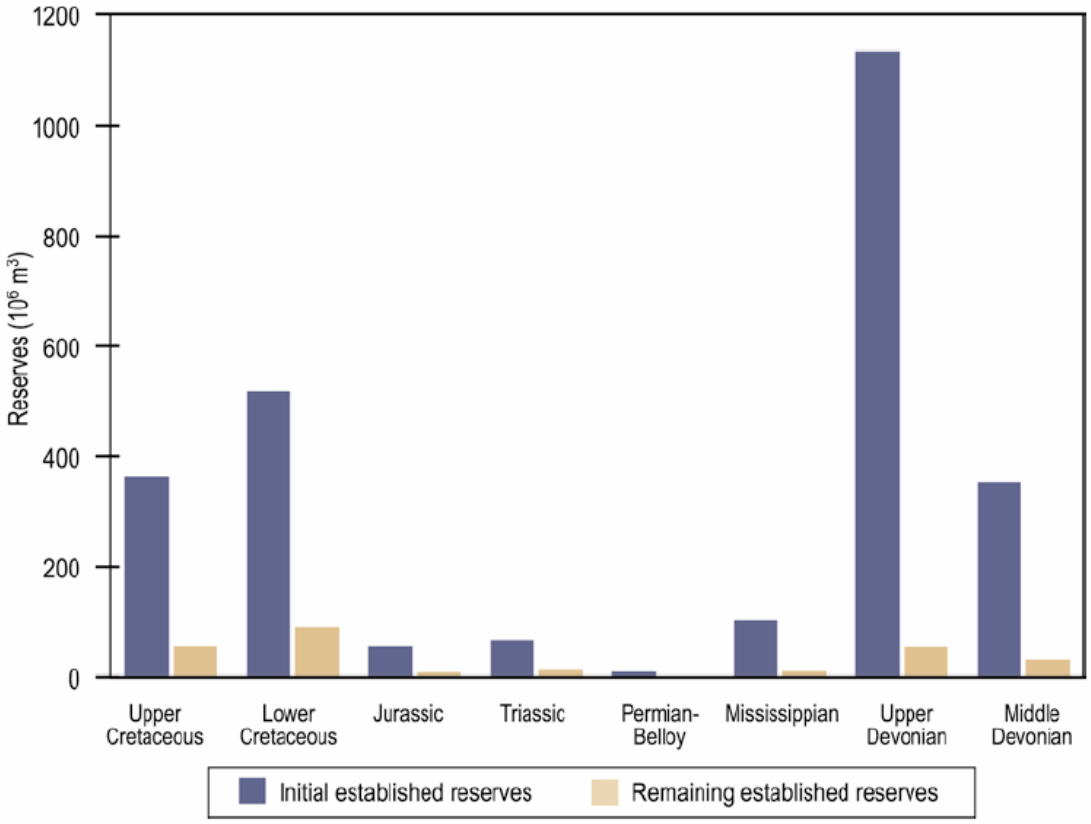

Figure 1-4: Geological distribution of reserves of conventional crude oil (Burrowes, 2003).

1.2.2 Geophysical methods used in the Rocky Mountain Foothills' exploration

Seismic reflection is by far the most important geophysical method in hydrocarbon exploration due to its high resolution and deep penetration, and has been used extensively in the Rocky Mountain Foothills. The complex geological structures in the Foothills present some challenges to the seismic method. High velocity contrasts beneath carbonate thrust sheets can cause difficulty in the imaging of the footwall of thrust faults. Some Foothills' rock formations, especially shales, may exhibit anisotropic behavior, which can cause lateral-position errors

on seismic image (Vestrum and Lawton, 1999). Due to the complexity and steep dip of some formations in the Foothills, migration is necessary during data processing. Among the many migration methods applied in Foothills' exploration, prestack depth migration gives the most accurate representation of the subsurface geology (Yan and Lines, 2001). Anisotropic depth migration has also been applied in the Foothills to correct the mispositioning caused by seismic velocity anisotropy (Vestrum and Lawton, 1999).

Other geophysical methods have been used in the exploration of the Foothills. High-resolution airborne magnetic data were used to map the near-surface lithology, and has provided structural information in the reconnaissance stages of exploration (Abaco et al., 2002). Airborne gravity and magnetic data were also used to map the structures in the overthrust belt (Peirce et al., 2002).

Electromagnetic methods have been used in overthrust belts for structural imaging in many regions of the world. The most suitable is the magnetotelluric (MT) method, which uses natural electromagnetic signals. Since MT uses natural EM signals and doesn't require power supplies, it is a cost effective technique with low environmental impact. All previous MT surveys in Alberta were carried out for tectonic research. Many MT surveys were carried out on the plains of Alberta in the 1960's and 1970's (Vozoff et al., 1963; Vozoff and Ellis, 1966; Reddy and Rankin, 1971). These surveys recorded MT data with large interstation spacing and relatively low frequency (<1 Hz). More recently, several two-dimensional magnetotelluric surveys were carried out in Alberta and the adjacent Cordillera (Hutton et al., 1987; Boerner et al., 1995; Boerner et al., 2000; Ledo and Jones, 2001). These surveys gave interpretations of the resistivity structure of the crust and upper mantle. None of them studied the upper crustal structures in the Foothills. The survey described in this thesis is the first attempt to apply magnetotellurics to structural imaging in the Rocky Mountain Foothills.

In overthrust belt exploration, the existence of Cretaceous strata beneath Paleozoic overthrust sheet is significant. However the complex structure and the velocity contrast between the high velocity hanging wall (the Paleozoic carbonate succession) and the low velocity footwall (the Mesozoic clastic succession) can make it challenging to identify the Cretaceous strata beneath overthrust sheet with seismic data. The geometry of the low resistivity Mesozoic clastic sedimentary rocks (resistivity ~ 10 Ωm) located beneath the resistive Paleozoic thrust sheets (resisitivity range from 100-1000 Ωm) has been observed in the Foothills (Figure 1-5). This feature makes the Mesozoic strata an ideal target for MT imaging because MT data are sensitive to the presence of a low resistivity layer.

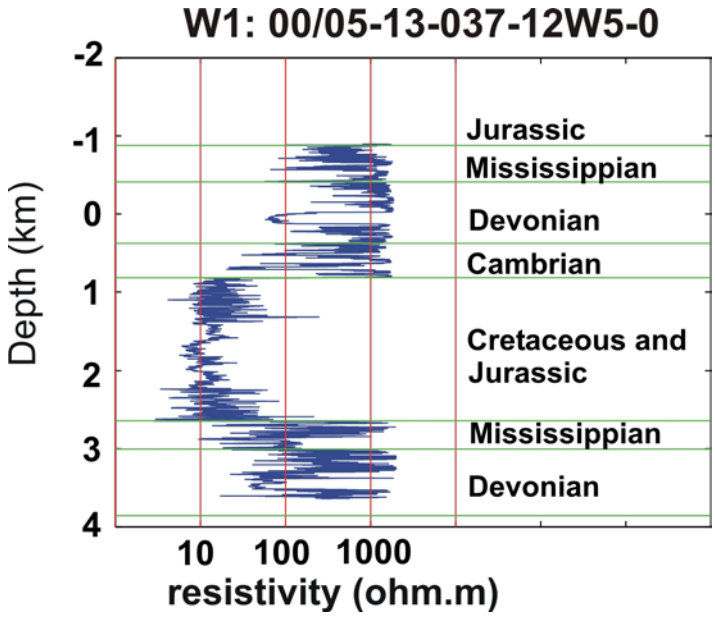

Figure 1-5: Resistivity log of Well: 00/05-13-037-12W5-0. Depth is below mean sea level. Location of the well is shown in Figure 4-1 (GeoWell General Well Standard Report, Alberta Geological Survey/Alberta Energy and Utility Board).

Chapter 2

Introduction to the magnetotelluric method

In this chapter, the magnetotelluric method is described. Readers who are familiar with the method can skip this chapter. The magnetotelluric (MT) method uses natural electromagnetic (EM) fields to map the spatial variation of the Earth's electrical resistivity. Natural electromagnetic (EM) field variations induce electric currents in the Earth. These subsurface currents generate secondary electromagnetic fields and modify the total EM field at the Earth's surface. These EM fields contain useful information about the electrical properties of the subsurface strata. By measuring the magnetic and electric fields at the Earth's surface, the apparent resistivity can be calculated as a function of frequency. Since signals with low frequency penetrate deeper into the Earth, this allows the variation of resistivity with depth to be determined.

2.1 General introduction

The electric current induced in the ground is related to the EM field and the electrical resistivity of the rocks. The electrical resistivity of rocks depends on the density of charge carriers and the geometry of current pathways. High porosity, high salinity pore fluid, high saturation of fluid, or partial melting of rock will give a high quantity of charge carriers. Good interconnection between pores can give a high density of electric current pathways. The resistivity of the rock is thus the combination of the above elements. An introduction to the electrical properties of rock and minerals can be found in Telford et al. (1990).

Archie's Law (Archie, 1942),

$$\rho = a\rho_w \varphi^{-m} s_w^{-n}$$

describes an empirical way to calculate the formation resistivity of a rock (ρ). In this equation a and m are empirical constants (depending on degree of consolidation), ρ_w is the resistivity of the formation fluid, φ is the porosity, S_w is the saturation of the fluid. The formation resistivity of sedimentary rocks can vary from 1 Ωm to 1000 Ωm (Figure 2-1) with the changes of permeability, porosity, formation fluid saturation and salinity.

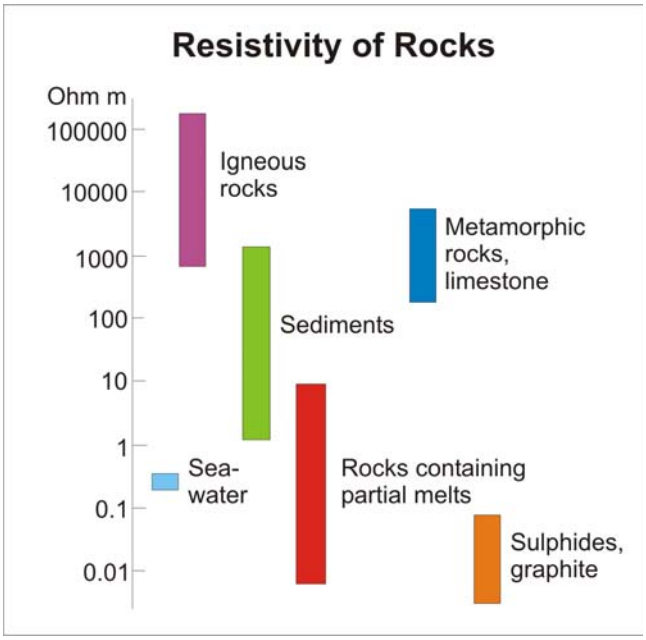

Figure 2-1: Electrical resistivity of rocks (from Martyn Unsworth, Geophysics 424, at the University of Alberta).

There are two main sources of natural EM signals that are used in MT exploration. From 1-10000 Hz, the natural EM fields are primarily generated in the Earth's atmosphere by worldwide lightning activities. These fields travel through the Earth-ionosphere waveguide. Signals between 2-5 KHz do not travel well and their amplitude is very small because their wavelength in air is comparable to the width of the waveguide. Most MT signals below 1Hz come from fluctuations of the Earth's magnetic field, which is caused by changes in the magnetosphere. The magnetosphere is a complex zone of plasmas, which is constantly being buffeted by the solar wind (Vozoff, 1991).

2.2 Introduction of equations

To understand the magnetotelluric method, consider a plane EM wave that is incident on the surface of the Earth. The resistivity of the Earth is much lower than the atmosphere, thus an EM signal travels as a wave in the air and diffuses in the Earth. The fundamental differential equations governing the behavior of electromagnetic fields are given by Maxwell's equations:

$$\nabla \cdot \mathbf{E} = p / \varepsilon \tag{2.1}$$

$$\nabla \cdot \mathbf{B} = 0 \tag{2.2}$$

$$\nabla \times \mathbf{H} = \sigma \mathbf{E} + \varepsilon \frac{\partial \mathbf{E}}{\partial t} \tag{2.3}$$

$$\nabla \times \mathbf{E} = -\frac{\partial \mathbf{B}}{\partial t} \tag{2.4}$$

where $\mathbf{E}$ is the electric field strength in *V/m*, $\mathbf{H}$ is the magnetic field strength, $\mathbf{B}$ is the magnetic flux density *W/m*^{2}, p is the volume charge density in *C/m*^{3}, σ is the conductivity in *S/m*, ε is the dielectric constant in F/m.

Because $\mathbf{J} = \sigma \mathbf{E}$ and $\mathbf{B} = \mu \mathbf{H}$, equation 2.3 can be rewritten as:

$$\nabla \times \mathbf{B} = \mu \mathbf{J} + \mu \varepsilon \frac{\partial \mathbf{E}}{\partial t} \tag{2.3a}$$

Here $\mathbf{J}$ is the current density in *A/m*^{2}, and μ is magnetic permeability in *H/m*. Usually the free space values $\mu_0 = 4\pi \times 10^{-7}\ H/m$ and $\varepsilon_0 = 8.85 \times 10^{-11}\ H/m$ are used in these equations.

Taking the curl of equation 2.4 and using equation 2.3a, a second order partial differential equation for $\mathbf{E}$ alone can be obtained:

$$\nabla^2 \mathbf{E} = \mu \sigma \frac{\partial \mathbf{E}}{\partial t} + \mu \varepsilon \frac{\partial^2 \mathbf{E}}{\partial t^2} \tag{2.5}$$

In the case of a dielectric environment, there is minimal conduction current, and the displacement current dominates. Thus equation 2.5 can be simplified to the wave equation:

$$\nabla^2 \mathbf{E} - \mu\varepsilon \frac{\partial^2 \mathbf{E}}{\partial t^2} = 0 \tag{2.6}$$

In the case of a conductive environment, the conduction current dominates and the effect of displacement current can be ignored. Thus equation 2.5 can be simplified to the diffusion equation:

$$\nabla^2 \mathbf{E} - \mu\sigma \frac{\partial \mathbf{E}}{\partial t} = 0 \tag{2.7}$$

The Earth can be treated as the conductive environment, so the diffusion equation can be used in MT data analysis. For an EM wave with a sinusoidal time variation, the electric field strength can be written as: $\mathbf{E} = \mathbf{E}_0 e^{-i\omega t}$. Substituting into equation 2.7 yields:

$$\nabla^2 \mathbf{E} + i\omega\mu\sigma\mathbf{E} = 0 \tag{2.8}$$

Note that due to the transformation of electromagnetic energy into heat, the strength of the fields decrease exponentially with depth. Consider a wave that travels in the Earth with an exponential amplitude decay in the *z* direction, equation 2.8 can be written as:

$$\frac{\partial^2 \mathbf{E}}{\partial z^2} + i\omega\mu\sigma\mathbf{E} = 0 \tag{2.8a}$$

With $\mathbf{E} = \mathbf{E}_0 e^{-i\omega t} e^{kz}$, where $\mathbf{E}_0$ is the electric field strength at the Earth's surface, equation 2.8a can be written as:

$$\mathbf{E}k^2 + i\omega\mu\sigma\mathbf{E} = 0 \tag{2.9}$$

Rearranging this formula gives:

$$\mathbf{E}(k^2 + i\omega\mu\sigma) = 0$$

Then solving for k:

$$k = \pm(1-i)\sqrt{\frac{i\omega\mu\sigma}{2}} \tag{2.10}$$

Here k is the complex wave number of the medium, E_s is the horizontal electric field at the surface. So the field propagate in Earth can be written as:

$$\mathbf{E} = \mathbf{E}_0 e^{-i\omega t} e^{i\sqrt{\frac{\omega\mu\sigma}{2}}z} e^{-\sqrt{\frac{\omega\mu\sigma}{2}}z} \tag{2.11}$$

In equation 2.11, the exponential term $e^{-\sqrt{\frac{\omega\mu\sigma}{2}}z}$ represents the decay of the amplitude as wave travels in the z direction. Skin depth is defined as the distance (δ) over which the electric field strength is attenuated by $1/e$ of the original field strength. Since

$$e^{-\sqrt{\frac{\omega\mu\sigma}{2}}\delta} = e^{-1}$$

then skin depth can be written as:

$$\delta = \sqrt{\frac{2}{\omega\mu\sigma}} \tag{2.12}$$

Rearranging equation 2.12, it can be shown that:

$$\delta \approx 503\sqrt{\frac{\rho}{f}} \text{ (m)} \tag{2.13}$$

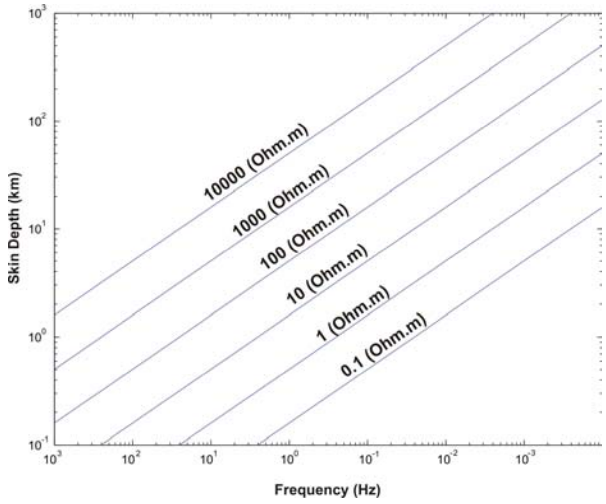

Figure 2-2: Skin depth as a function of the frequency of the MT signal and the resistivity of the Earth.

Equation 2.13 shows that the skin depth depends on two parameters: (1) the resistivity of the medium and (2) the frequency of the wave. Skin depth decreases with decreasing resistivities and increasing frequency. If the Earth's resistivity varies from 0.1-10^4 Ωm and the frequency varies from 10^3-10^{-4} Hz, then the skin depth varies from tens of meters to tens of kilometers (Figure 2-2).

The magnetic field strength of an EM wave with sinusoidal time variation can be written as $\mathbf{H} = \mathbf{H}_0 e^{-i\omega t}$. Then from equation 2.4:

$$\mathbf{H} = \frac{1}{i\omega\mu_0} \nabla \times \mathbf{E} \tag{2.14}$$

So in the Earth, comparison of the electric field strength and magnetic field strength can be written as:

$$E_x = E_0 e^{-kz} e^{-i\omega t} \tag{2.15}$$

$$H_y = \frac{1}{i\omega\mu_0} E_0 e^{-kz} e^{-i\omega t} \tag{2.16}$$

Here the electric field, E_x, is orthogonal to the magnetic field, H_y.

In order to derive useful information about the Earth's resistivity structure from measurements at the surface (z=0) the ratio of measured orthogonal E to H is used and defined as impedance:

$$Z = \frac{E}{H} \tag{2.17}$$

From equations (2.15) and (2.16), the impedance Z_{xy} is given by:

$$Z_{xy} = \frac{E_x}{H_y} = \frac{(1-i)}{\sqrt{2}} \sqrt{\omega\mu_0\rho} \tag{2.18}$$

Apparent resistivity ρ_{xy} can be solved for from equation 2.18:

$$\rho_{xy} = \frac{1}{\omega\mu_0} \left| \frac{E_x}{H_y} \right|^2 \tag{2.19}$$

and the argument of impedance Z_{xy} is defined as phase,

$$\varphi_{xy} = \arg(Z_{xy}) \tag{2.20}$$

where the angular frequency $\omega=2\pi f$. Here the apparent resistivity depends on the ratio of electric and magnetic field components. Thus the absolute amplitude of the incident EM wave does not matter, so the measurements at different times can be combined to estimate the impedance in the frequency domain.

Apparent resistivity, ρ_{xy}, represents the volume average of the Earth's resistivity over a hemisphere with radius equal to the skin depth. The phase, φ_{xy}, reflects the phase difference between the electric and magnetic field components. The apparent resistivity and phase are the two main parameters used to extract resistivity structure information from measured data. By computing the apparent resistivity as a function of frequency, the variation of resistivity with depth can be determined.

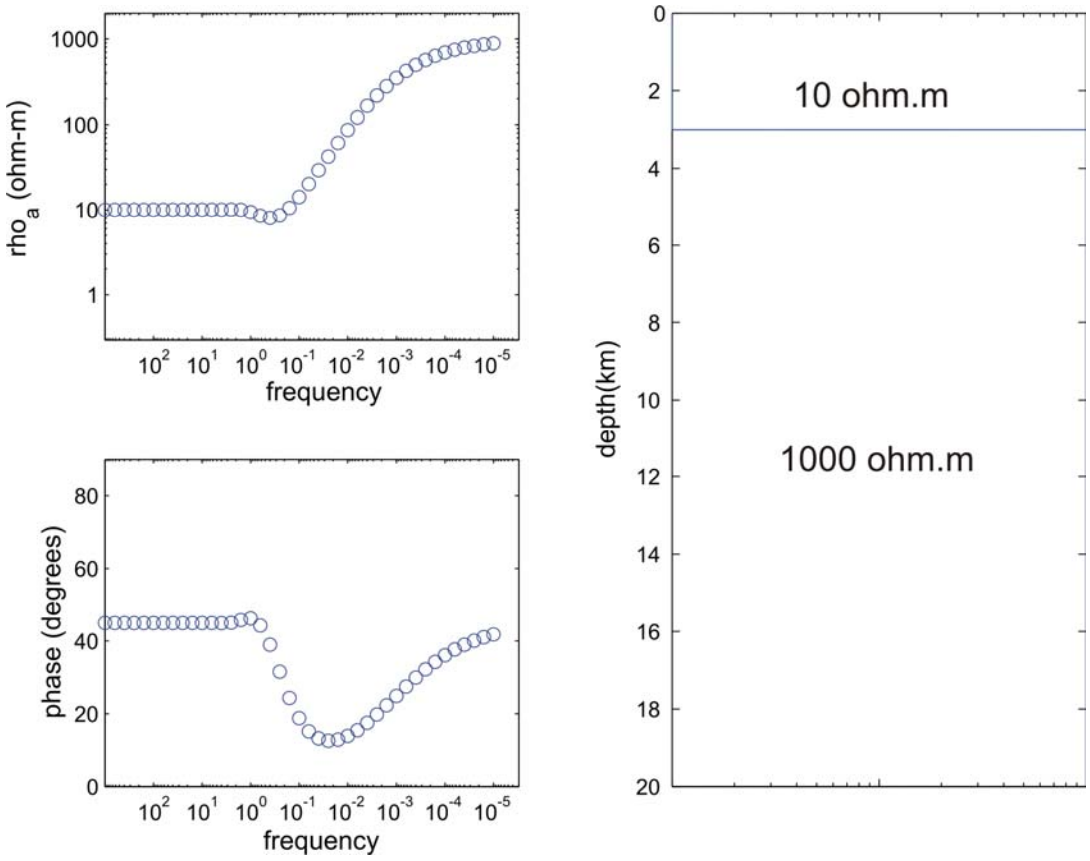

Figure 2-3: Example of apparent resistivity and phase for a 1-D MT model.

Figure 2-3 shows an example of apparent resistivity and phase data for a simple layered Earth. The resistivity of the upper layer is 10 Ωm. At high frequencies (300-1 Hz) the apparent resistivity is equal to the true resistivity of the upper layer and the phase is 45°. As the frequency decreases, the skin depth increases and the MT signal penetrate further into the Earth. The apparent resistivity rises and the phase goes below 45°. At very low frequency, the apparent resistivity approaches the resistivity of the lower layer, and the phase returns to 45°. The phase of MT data is the phase angle between electric and magnetic fields measured at Earth's surface. The apparent resistivity and phase are related through:

$$\varphi_{xy} \approx 45\left(1 - \frac{d(\log_{10}(\rho_{xy}))}{d(\log_{10}(T))}\right) \tag{2.21}$$

where T is the period of the signal ($T=1/f$) and φ is in degrees. Thus when the apparent resistivity increases with period, the phase will be less than 45°. Similarly a decrease in resistivity will correspond to a phase greater than 45°. At the very lowest frequencies, the apparent resistivity asymptotically approaches the true resistivity of the lower layer, and the phase returns to 45°. Note that since the magnetotelluric phase is dependent on changes in resistivity, it is generally more sensitive to subsurface structure (Vozoff, 1991).

After the apparent resistivity and phase are extracted from the measured data as function of frequency, a model of resistivity as a function of horizontal position and depth can be created by inversion. The inversion technique will be discussed in Chapter 5.

2.3 Two-dimensional magnetotellurics

In a uniform and horizontally layered Earth, the apparent resistivity does not depend on the direction of the measured electric and magnetic field components. If the structure is two-dimensional or three-dimensional, this is not the case. The

anisotropy of apparent resistivity results in different values of the apparent resistivity derived from the electric and magnetic field components measured in different directions over a two-dimensional or three-dimensional Earth. Thus the application of 1-D magnetotelluric data analysis in a complex geoelectric environment can give misleading results and most data sets require two-dimensional or three-dimensional analysis.

Great progress has been made in the last decade in two-dimensional and three-dimensional MT modeling and inversion (Mackie et al., 1993; Rodi and Mackie, 2001). However, if just a single profile of MT stations is available, and three-dimensional effects can be shown to be small, then two-dimensional analysis has many advantages. Consider the geometry shown in Figure 2-4, where the geological strike direction is along the x-axis. In a general three-dimensional environment all six components of the electric and magnetic field are interdependent. However in a two-dimensional Earth this situation becomes simpler when the measured EM fields are separate into two modes. The field components E_x, H_y and H_z are related to the along strike electric current. Together these three field components are called transverse electric (TE) mode with apparent resistivity computed from E_x and H_y. The TE mode is most sensitive to along strike conductors. Correspondingly, H_x, E_y and E_z field components comprise the transverse magnetic (TM) mode, with the apparent resistivity computed from E_y and H_x. In this mode, current flows across the boundaries of different resistivities, which causes electric charges to build up on the interfaces. Thus the TM mode is more effective than the TE mode in locating interfaces between regions of differing resistivity.

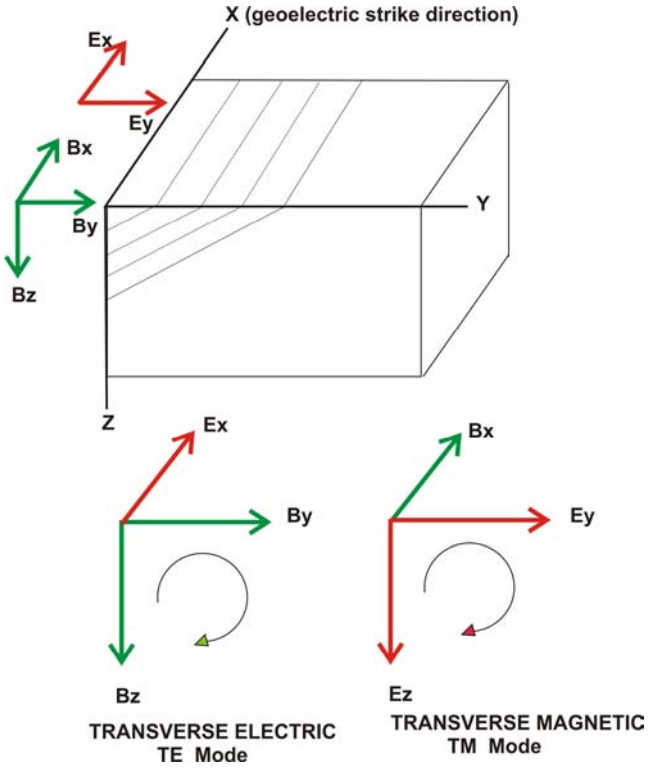

Figure 2-4: Configuration of EM fields for a two-dimensional geoelectric structure.

In addition to recording the horizontal electric and magnetic field components, most modern MT systems record simultaneous temporal variations in the vertical magnetic field. These data can be used in numbers of ways, but one of the most common is to compute the tipper, which is defined as the ratio of vertical to horizontal magnetic fields ($T=H_z/H_y$), at each MT station. Because EM waves travel vertically in the Earth and only horizontal components of electric and magnetic fields exist in the primary EM fields (this is true at most places on Earth except close to equator and poles where the plane wave assumption is not valid). So the vertical magnetic field measured in the ground is dominated by the vertical component of the magnetic field of the induced current in ground, thus the variation of the ratio can show the lateral changes in resistivity.

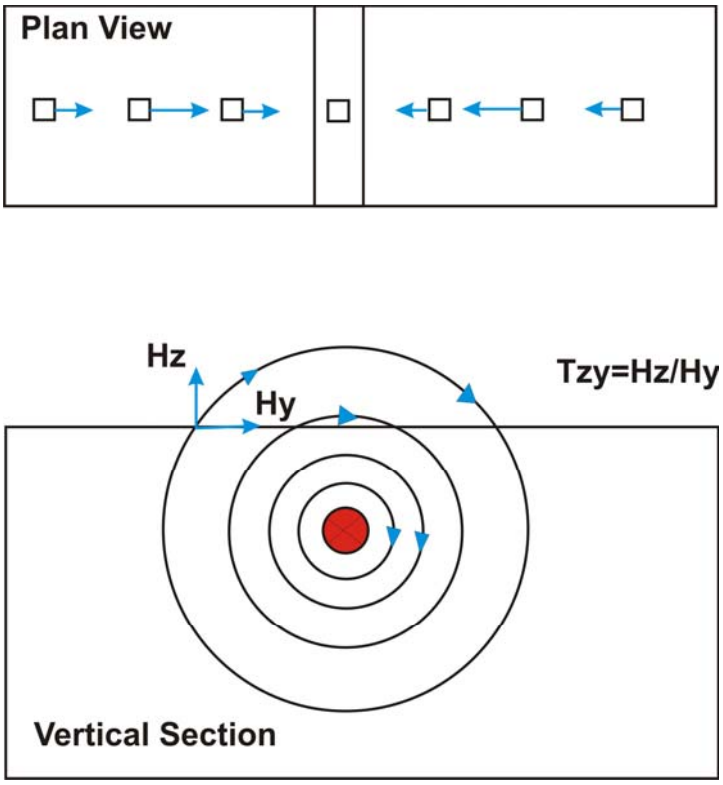

Figure 2-5: The geometry of the vertical component of magnetic fields associated with TE mode electric currents flowing in a buried low resistivity body. Arrows in plan view show the induction vectors. Arrows in vertical section show directions of magnetic field components (Martyn Unsworth, Geophysics 424, University of Alberta).

Figure 2-5 shows the geometry of the magnetic field over a low resistivity cylinder. The TE-mode current flows along the low resistivity body and generates secondary magnetic fields that are up on one side and down on the other side. Induction vectors are horizontal vectors with a magnitude equal to the ratio $T_{zy}=H_z/H_y$. Both the in-phase and quadrature components of T_{zy} are computed. In the convention used in North America, these induction vectors will point towards a low resistivity body (Parkinson, 1962).

2.4 Tensor decomposition

If an MT data set can be shown to be two-dimensional, then the analysis is greatly simplified. This requires using dimensional analysis to assess the dimensionality of the MT data.

For a horizontally layered 1-D Earth, the impedance is independent of azimuth. But in two-dimensional and three-dimensional cases, it is not the case. The concept of the impedance tensor was introduced by Cantwell and Madden (1960) to describe the relations between the electric and magnetic field components.

H_x is proportional to both E_y and E_x. Likewise H_y is related to E_x and E_y, so that at each frequency it can be written as:

$$\begin{aligned} E_x &= Z_{xx}H_x + Z_{xy}H_y \\ E_y &= Z_{yy}H_y + Z_{yx}H_x \end{aligned} \tag{2.22}$$

Note that each term is frequency dependent (Vozoff, 1991). Equation 2.22 can be written in tensor form as:

$$\begin{pmatrix} E_x \\ E_y \end{pmatrix} = \begin{pmatrix} Z_{xx} Z_{xy} \\ Z_{yx} Z_{yy} \end{pmatrix} \begin{pmatrix} H_x \\ H_y \end{pmatrix} \tag{2.23}$$

This equation was proposed by Cantwell and Madden (1960) and Rokityanski (1961). It is assumed that the electric fields are only due to magnetic fields (note that noise is not considered here). In the 1-D case, Z_{xx} and Z_{yy} are zero, and $Z_{xy} = -Z_{yx}$. Then the equations reduced to: $E_x = Z_{xy}H_y$ and $E_y = Z_{xy}H_x = -Z_{yx}H_x$. In a two-dimensional case, if the x or y axis is along the geoelectric strike then $Z_{xx} = Z_{yy} = 0$, but $Z_{xy} \neq -Z_{yx}$. If both axes are not parallel to the geoelectric strike then $Z_{xx} = -Z_{yy} \neq 0$ (Vozoff, 1991).

$Z_{xx} = Z_{yy} = 0$ means there is no relation between E_x and H_x or E_y and H_y. E_x and H_y are totally caused by the current flow in the x direction, and E_y and H_x are totally caused by the current flow in y direction. Thus the calculation of the apparent resistivity can be simplified into

$$\rho_{xy} = \frac{1}{\omega\mu_0}\left|Z_{xy}\right|^2 \text{ and } \rho_{yx} = \frac{1}{\omega\mu_0}\left|Z_{yx}\right|^2,$$

and phase is given by:

$$\varphi_{xy} = \arg(Z_{xy}) \text{ and } \varphi_{yx} = \arg(Z_{yx}).$$

The above discussion shows that in the pure two-dimensional case, if one of the axes is along the geoelectric strike, this will greatly simplify the calculation. The two-dimensional MT method is based on this concept and separates the measured fields into TE and TM modes. Thus one of the tasks in data processing is to determine the geoelectric strike and rotate the data to that coordinate frame.

One method to determine the geoelectric strike is tensor decomposition technique, which analyses the impedance tensor in different coordinates and finds the direction that gives maximum or minimum values of various combinations of Z_{ij}. In tensor decomposition analysis the rotation tensor

$$\mathbf{R} = \begin{pmatrix} \cos\theta & \sin\theta \\ -\sin\theta & \cos\theta \end{pmatrix}$$

is introduced and the vector E field is rotated through angle $+\theta$ (clockwise) to be E', then

$$\begin{pmatrix} E'_x \\ E'_y \end{pmatrix} = \begin{pmatrix} \cos\theta & \sin\theta \\ -\sin\theta & \cos\theta \end{pmatrix}\begin{pmatrix} E_x \\ E_y \end{pmatrix} \tag{2.24}$$

or

$$\mathbf{E}' = \mathbf{RE}$$

In the same way,

$$\mathbf{H}' = \mathbf{RH} \tag{2.25}$$

and

$$\mathbf{Z}' = \mathbf{R}\mathbf{Z}\mathbf{R}^T \tag{2.26}$$

where the $\mathbf{R}^T$, the transpose of $\mathbf{R}$, is $\mathbf{R}^T = \begin{pmatrix} \cos\theta & -\sin\theta \\ \sin\theta & \cos\theta \end{pmatrix}$. Several different methods have been used to find the rotation angle θ_0 between the measurement direction and the strike. The method of Swift (1967) is widely used and finds the strike angle θ_0 by finding the maximum value of

$$\left|Z'_{xy}(\theta_0)\right|^2 + \left|Z'_{yx}(\theta_0)\right|^2 \tag{2.27}$$

This gives a solution

$$4\theta_0 = \tan^{-1}\left(\frac{\left[\left(Z_{xx} - Z_{yy}\right)\left(Z_{xy} + Z_{yx}\right)^* + \left(Z_{xx} - Z_{yy}\right)^*\left(Z_{xy} + Z_{yx}\right)\right]}{\left|Z_{xx} - Z_{yy}\right|^2 - \left|Z_{xy} + Z_{yx}\right|^2}\right) \tag{2.28}$$

that maximizes $\left|Z_{xy}\right|$ and minimizes $\left|Z_{xx}\right|^2 + \left|Z_{yy}\right|^2$.

The notion of non-inductive galvanic distortion of the electric field by a three-dimensional surfacial feature was first introduced by Larsen (1977) for a 1-D subsurface (3-D/1-D), and was extended to a two-dimensional subsurface (3-D/2-D) by Richard et al. (1982). The basic distortion model can be written as

$$\mathbf{Z}_m = \mathbf{R}\mathbf{C}\mathbf{Z}_{2D}\mathbf{R}^T \tag{2.29}$$

Here **C** is a real 2×2 telluric distortion tensor that was introduced to describe the effect of distortion, and the $\boldsymbol{Z}_{2D}$ is the regional two-dimensional impedance tensor in the strike coordinates. The physical basis for this equation is given by Groom and Bahr (1992) and Chave and Smith (1994). The Groom and Bailey decomposition analysis (GB decomposition) is a widely used technique. In GB decomposition the telluric distortion tensor C is written as

$$\mathbf{C} = g\mathbf{T}\mathbf{S}\mathbf{A} \tag{2.30}$$

where g is a scalar quantity termed site gain and T, S, A are matrices termed *twist*, *shear*, and *anisotropy,* respectively (Groom and Bailey, 1989). The twist (**T**)

and shear ($\mathbf{S}$) tensors account for the determinable portion of the distortion matrix. The site gain (g) and anisotropy tensor ($\mathbf{A}$) together form the indeterminable parts of the distortion matrix that scale the apparent resistivity curves.

Absorbing the site gain g and anisotropy A into the regional impedance, equation 2.29 can be written as

$$\mathbf{Z}_m = \mathbf{RTSZ}_{reg}\mathbf{R}^T \tag{2.31}$$

where $\mathbf{Z}_m$ is the measured impedance tensor and $\mathbf{Z}_{reg}$ is the scaled regional two-dimensional impedance tensor ($g\mathbf{AZ}_{2D}$). The regional two-dimensional geoelectric strike and information about the two regional impedances can be recovered by determining $\mathbf{Z}_{reg}$ from equation 2.31.

2.5 Static shifts

Static shifts are defined as vertical displacements of the apparent resistivity sounding curves, between adjacent sites or between two curves at one site, without any other difference in either the shape of the curves or the phase (Figure 2-6). Static shifts are caused by the electric field generated from boundary charges on surfacial inhomogeneties (Vozoff, 1991).

The electric field resulting from the boundary charges reduces the measured electric field, and thus decreases the measured impedance, lowering the apparent resistivity of the low resistivity side. On the resistive side the electric field is reinforced, making the region appear even more resistive (Figure 2-7). The effect of boundary charges is observed at all frequencies. If the inhomogeneities are large enough (larger than the skin depth of the highest frequency on the MT sounding curve) it could produce a frequency-dependent response and can be recognized in both apparent resistivity and phase data.

Such bodies are usually the target of an MT survey and should be modeled as part of the interpretation. However, the small size (smaller than the skin depth of the highest frequency on the MT sounding curve) of near-surface geoelectric features in the vicinity of the measurement point will produce a frequency independent response on the apparent resistivity curve, which shifts the apparent resistivity sounding curve up or down (Torres-Verdin and Bostick, 1992). This implies that the offset is a result of a geoelectric feature at the surface that is so thin that its effect on phase has disappeared above the highest measured frequency. In other words, the sounding frequency is so low that induction effects in the surfacial inhomogeneity body have vanished. If higher frequencies could be recorded, then an observed difference would appear in the shape of both apparent resistivity and phase curves. If the MT data is recorded at more closely spaced sites the feature could be mapped and interpreted. Static shifts are due to under-sampling in both frequency and space (Vozoff, 1991).

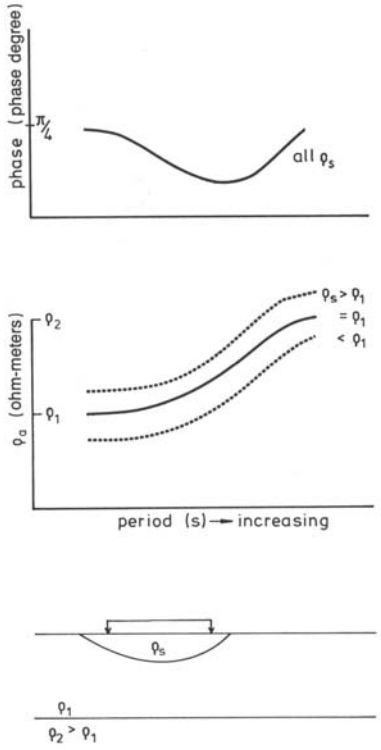

Figure 2-6: Sketch of the model used to explain static effects. The middle apparent resistivity curve is that which would be observed if the inlier had the same resistivity as the layer (Vozoff, 1991).

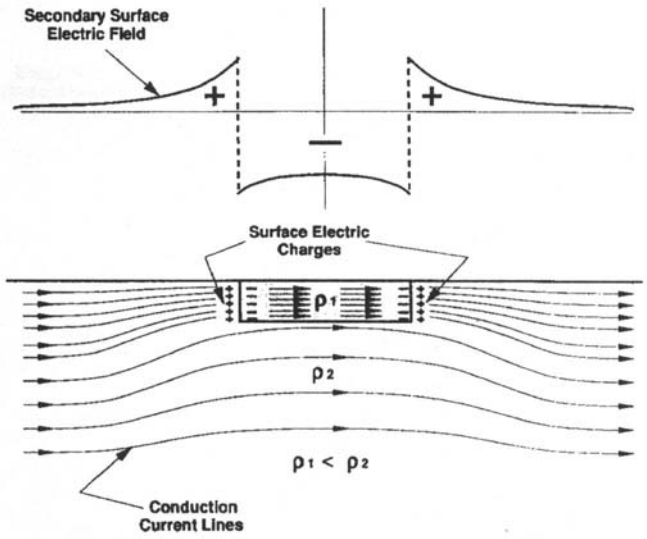

Figure 2-7: DC-limit (zero frequency) TM electric field response of the surface low resistivity body. ρ_1=0.5(Ωm), ρ_2=20(Ωm); The lower diagram depicts how a laterally uniform conduction current is bent upward and channeled through the surface low resistivity body. This channeling effect is manifested on the surface as the surge of secondary electric field with positive and negative lateral variations across the low resistivity body, as shown in the upper curve. Because of Faraday's Law, an average of these lateral variations will tend to zero as the observations of the electric field are extended infinitely away from the low resistivity body (Torres-Verdin and Bostick, 1992).

Since static shifts can severely distort MT data thus mislead the interpretation, static shifts correction is necessary in MT data processing. The details will be discussed in the Chapter 4.

Chapter 3

Application of the magnetotelluric method in hydrocarbon exploration

Due to its simple field logistics and low cost, the MT method is widely used in mineral and geothermal exploration (Christopherson, 2002; Zhang et al., 1998; and references therein). Recently, with advances in equipment, data processing and interpretation, MT is being more widely used in hydrocarbon exploration. The method is used primarily in areas where seismic exploration is difficult, such as overthrusts and where high-velocity cover such as carbonates and volcanic rocks are present.

When Tikhonov (1950) and Cagniard (1953) proposed the magnetotelluric method independently, the dependence of MT on natural EM sources quickly attracted geophysicists' attention. Requiring no power source or corresponding control system made it a cost effective exploration technique. In the past fifty years, the magnetotelluric method has developed both in theory and equipment.

The development of the MT method can be divided into two stages. The first stage was from the early 1950's to the end of the 1970's. During this period, the MT method progressed steadily with the debate on the validity of the plane wave assumption (Wait, 1954; Price, 1962; Madden and Nelson, 1964), the introduction of the concept of the impedance tensor (Cantwell and Madden, 1960), the development of remote reference technique (Gamble et al, 1979), and the application of 1-D inversion (Wu, 1968; Jupp and Vozoff, 1977; Oldenburg, 1979). The development was hindered by the lack of innovation in instrumental, data processing and interpretation techniques.

The second stage was from the end of the 1970's to the present day. MT has advanced rapidly with the revolution of digital electronics, new data processing and interpretation techniques. Multi-channel acquisition units have enhanced data quality and efficiency.

3.1 The application of the MT method in oil and gas exploration in early stage

In the early stage, due to the inherent lower resolution of MT compared to seismic and the use of 1-D analysis, MT was not suitable for imaging structures in geologically complicated areas. Rather MT was just used in imaging the depth to basement in basins. Even with these limitations, the MT method still achieved significant success in petroleum exploration in the USSR (Berdichevsky and Dmitriev, 2002).

The application of MT in oil and gas exploration in the USSR started in the 1960's. More than 10,000 MT-soundings were carried out within the USSR from the 1960's to the 1980's and the area that was covered with MT amounted to 3 million square kilometers. Because of its low cost, MT was generally used before seismic exploration. The major uses of MT were for regional geological study and basin evaluation. The MT data gave a clear image of the topography of basement and yielded enough information to distinguish the structural elements of the basins. The disagreement in the depth of crystalline basement determined by MT data and drilling was often less than 10% (Berdichevsky and Dmitriev, 2002). In Western Siberian, MT successfully detected a structural high in the Paleozoic basement topography which resulted in the discovery of Urengoy gas field, which is the largest gas field in the world (Berdichevsky and Dmitriev, 2002). However when exploration was applied to more subtle structures and stratigraphic traps, the application of MT method stopped in the mid 1980's in USSR due to the lower resolution of MT compared to seismic (Berdichevsky and Dmitriev, 2002).

3.2 Recent technique development of MT method and its application in hydrocarbon exploration

During the second stage, with the rapid development of software and instrumentation, MT has become more useful in hydrocarbon exploration. A number of technical advances have been made. The remote reference technique has greatly improved data quality (Gamble et al, 1979). Tensor decomposition can remove three-dimensional distortion (Groom and Bailey, 1989; McNeice and Jones, 2001). The Transient EM technique can effectively correct the static shift caused by surficial inhomogeneities (Pellerin and Hohmann, 1990). Two-dimensional inversion makes it practical to image structures in geologically complicated areas (deGroot-Hedlin and Constable, 1990; Smith and Booker, 1991; Mackie and Rodi, 1996). The problem of static shifts can be largely overcome by the two-dimensional regularized inversion (deGroot-Hedlin, 1991). More portable and reliable digital acquisition systems have been produced by companies such as Phoenix, EMI and Metronix. All these improvements have created a favorable environment for the application of MT in hydrocarbon exploration.

Since the late 1980's, there has been an increase in the application of MT to hydrocarbon exploration in western countries. The applications are concentrated in the overthrust zones that are difficult for seismic exploration due to the high velocity contrast beneath the thrust sheet. Due to a combination of appropriate source rocks, thermal maturation, and reservoir conditions, overthrust zones are common targets in petroleum exploration (Picha, 1996). However in many overthrust zones, the high velocity (older) rocks are thrust to surface, above lower velocity (younger) rocks. This can cause poor quality seismic reflection data in these areas (Watts and Pince, 1998; Watts et al., 2002).

Watts and Pince (1998) show an example of MT exploration in petroleum exploration in southern Turkey. In this case the relatively soft strata, low resistivity deep-sea sediments are intercalated with ophiolitic assemblages, have been thrust over the rigid and high resistivity carbonates. The allochonous sheets in this condition represent a chaotic assemblage of differing lithologies and lead to poor quality seismic data. This has resulted in a resistivity contrast with 1-10 Ωm Mesozoic ophiolitic mélange (Kocali and Karadut Formations) over 100 Ωm Martin Group carbonates. Through a comparison of seismic data and MT data, they can interpret the discontinuous seismic reflector. MT data give a clearer image of the top of the carbonates, the Mardin Group (Figure 3-1). Another example is the MT application in sub-thrust petroleum exploration in Northern Greece (Watts et al., 2002), where the quality of seismic data is also poor. The MT gave a clear image of the structures there from the resistivity contrast between the carbonates-anhydrite unit (200-2000 Ωm) and the clastic unit (20-100 Ωm). Seismic data acquisition in an area of difficult topography may cost 10 times as much as an MT survey. An MT survey in northern Greece costs 0.11 Million Euro, to cover the same area, where seismic costs 2.375 million Euro. Thus there can be a significant cost/benefit improvement by using the MT method in hydrocarbon exploration in difficult environments.

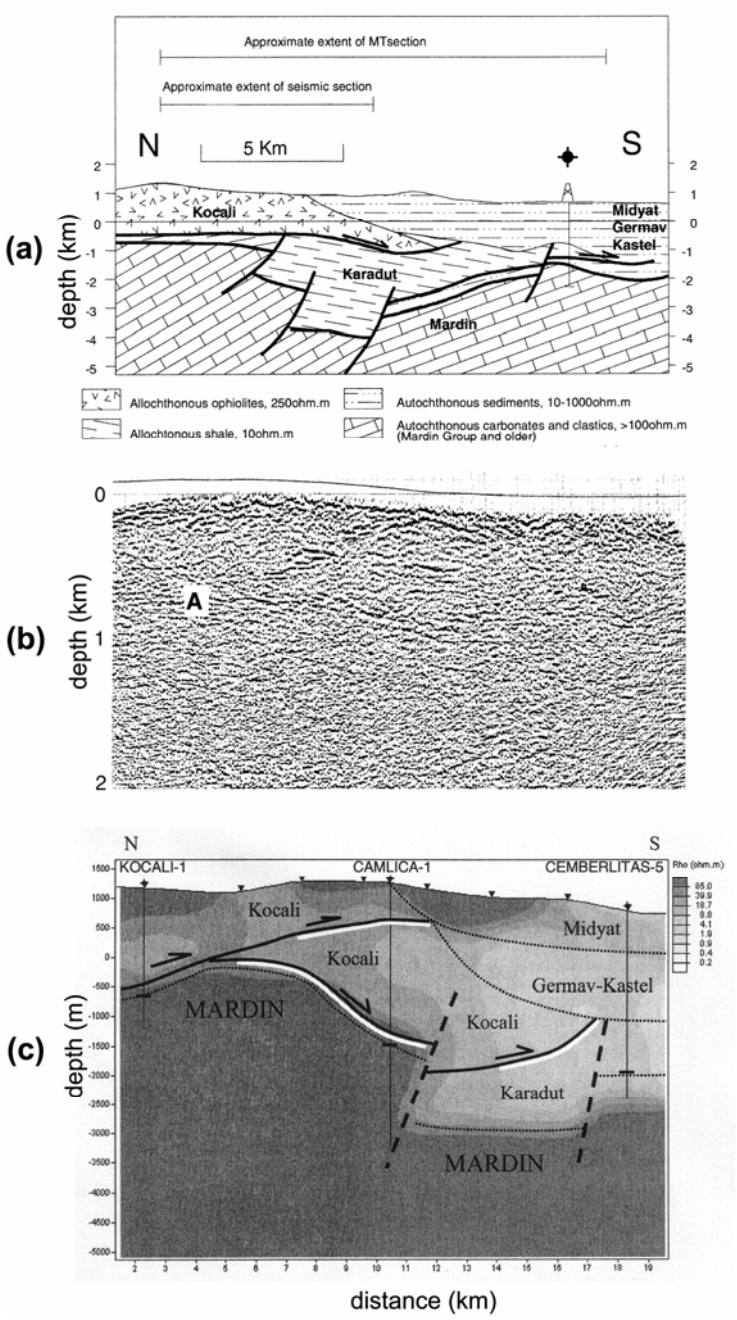

Figure 3-1: (a), Schematic cross section, based on regional well control. Elevation in kilometers. (b), Seismic section corresponding to the central part of (a). The letter A denotes the target Mardin reflector that can be identified in seismic section. (c), two-dimensional inversion of MT data (gray scale). White line represents seismic reflectors. Crossbar on well shows top of Mardin group. Inverted triangles are MT stations. Vertical scale is elevation in meters; horizontal scale is in kilometers (Watts and Pince, 1998).

The MT method has been applied in the petroleum exploration in the Papuan fold belt in New Guinea (Christopherson, 1991), where a 1000 m thick Eocene to Miocene massive limestone succession covers a Jurassic-Cretaceous clastic succession, which was the main target of hydrocarbon exploration. Due to the high velocity and karstifing of the limestone outcrop in the fold belt, the quality of seismic data was poor. However the strong resistivity contrast between the limestone and the underlying clastic succession is favorable for MT exploration. The MT surveys successfully imaged the low resistivity (2.75-7.5 Ωm) Jurassic and Cretaceous clastic succession that beneath the high resistivity (200-400 Ωm) limestone.

The MT method also has been used in oil exploration in Minami-Noshiro area in Japan (Matsuo and Negi, 1999). Thrust faults were distinguished by the rapid change of the thickness of the low resistivity layer in the two-dimensional inversion. The resistivity model also gave images of known anticlines and synclines. Three-dimensional inversion has been applied to these data.

Some tectonic studies have also shown that MT data can image thrust sheets. MT data collected in the foreland of the Daxue Shan (northeast of the Tibetan Plateau) imaged low angle thrust faults by the resistivity contrast between the overthrust crystalline basement rock (~1000 Ωm) and the underneath basin sediments (10-100 Ωm) (Bedrosian et al., 2001). The high-resolution MT profile of Park et al. (2003) yields a resistivity model with a clear image of underthrust sediments at the margin of an intermontane basin in the central Tien Shan Mountains.

MT method has also been tried in subsalt hydrocarbon exploration. Due to the high velocity of salt and the irregular shape of a salt body, it is difficult for seismic imaging beneath the salt body. But with the high resistivity contrasts of salt (20 Ωm) to its surrounding sediments (1 Ωm), MT is a good choice to mapping the

base of salt body. Some marine MT experiments for salt base mapping have been reported (Hoversten et al., 2000).

The above examples show that the MT method is mature in data acquisition equipment, data processing and interpretation techniques to image structures in overthrust region. Although it has a lower inherent resolution than seismic exploration, its low cost and low environmental impact give it some advantages. There is potential cost benefit if an MT survey is performed before a seismic survey. In an area where seismic exploration is difficult, MT can play a significant role in the reconnaissance stage of petroleum exploration.

Chapter 4

Magnetotelluric data acquisition and processing

The previous chapter showed that magnetotelluric exploration has proven to be a useful tool for imaging structures in overthrust belts. Thus the magnetotelluric method has been applied to structural imaging in the Rocky Mountain Foothills.

4.1 Magnetotelluric data collection

The MT data were collected in August and October 2002. The MT stations were located along Secondary road 752 and the Forestry Trunk Road as shown in Figure 4-1. The profile is almost 65 km long with station spacing varying from 1.7-6.1 km, and is perpendicular to the regional geological strike.

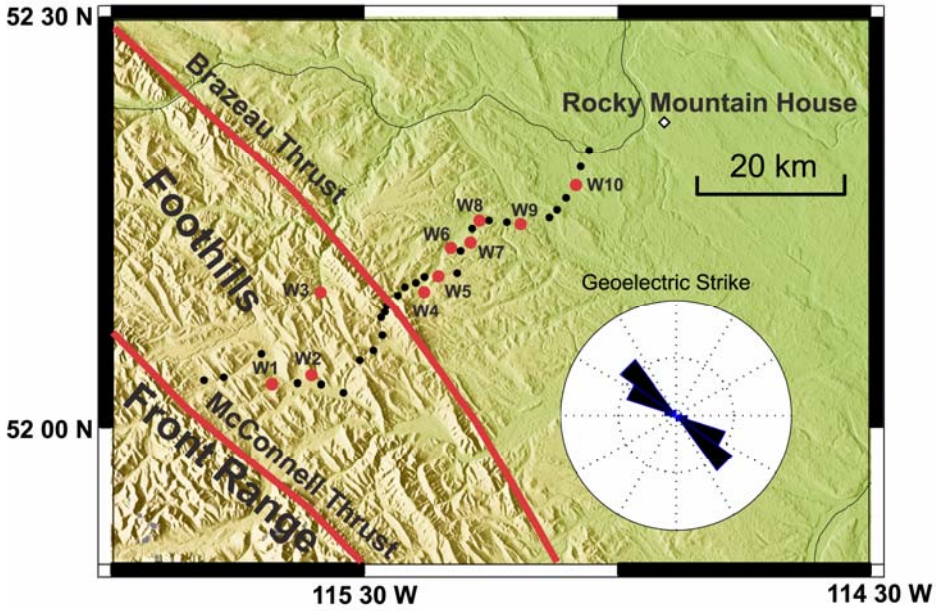

Figure 4-1: Location of MT sites and well logs used in the study. Black dots denote locations of MT sites, red dots denote locations of the well logs that are used in Chapter 6. The rose diagram shows the regional geoelectric strike (frequency band: 100-0.01 Hz) determined by tensor decomposition (McNeice and Jones, 2001).

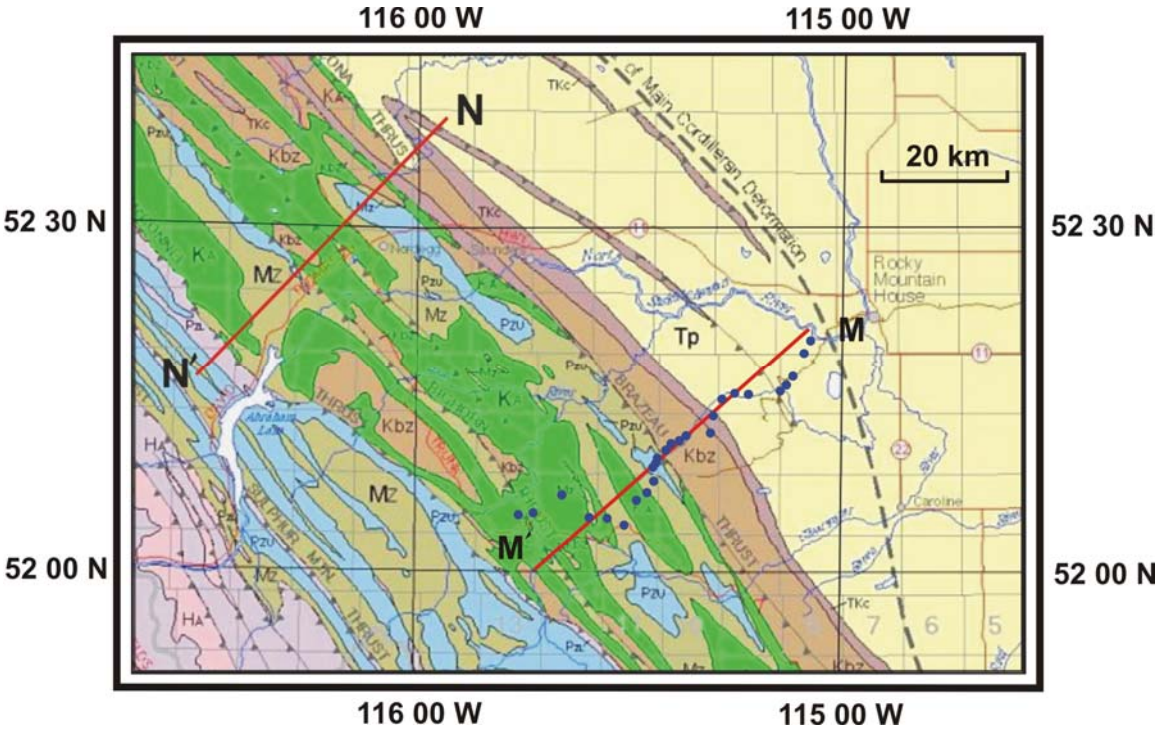

Figure 4-2: Geological map of study area. MM' shows the location of MT profile, blue dots show locations of the MT stations; NN' shows the location of the Nordegg Area Geological Cross Section used in Figure 6-1 (modified from Geological Map of Alberta, Alberta Geological Survey/Alberta Energy and Utility Board).

The MT data were collected with MTU-5 and MTU-2E systems produced by Phoenix Geophysics in Toronto. The MTU-V5 system can measure three components of the magnetic field and two components of the electric field. The MTU-2E system measures just two components of the electric field. Time synchronization is achieved with GPS (Global Positioning System) signals. A typical 5-channel site is composed of five electrodes, three magnetic sensors, an MTU-5 box, and a battery (Figure 4-3). Two electric cables, with an electrode at each end (approximately 100 m long), were laid on the ground perpendicular to each other to measure the electric field. One ground electrode was planted and connected to the center of the cables. Two magnetic sensors were buried horizontally, perpendicular to each other, and one magnetic sensor was buried vertically (Figure 4-3). The MTU box recorded the time variation of the electric

and magnetic fields and stored the data on a removable flash card. At the 2E site, the MTU-2E box was only connected to two electric cables to measure the electric fields. The magnetic field data from a neighboring 5-channel site was used in the data processing for these 2E sites. The MTU boxes recorded data in the frequency range from 384 Hz to 1/1800 Hz, with 13 frequencies per decade. Because the regional geological strike was obvious, the MT data were recorded in the regional geological strike frame, N30°W, at all stations.

During the three weeks of fieldwork, MT data were collected at 26 stations. This included ten 5-channel stations and sixteen 2E stations. The MT data were recorded overnight at all stations. At all times, there were two 5-channel stations running simultaneously to provide the synchronized signal for remote reference processing (Gamble et al, 1979).

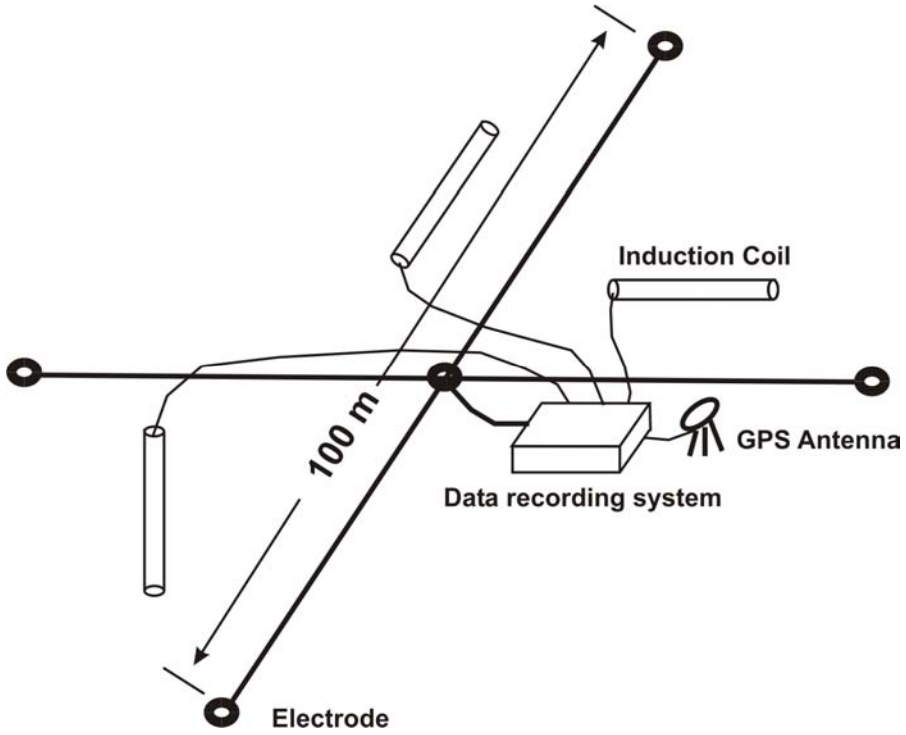

Figure 4-3: Configuration of a broadband MT recording system.

To obtain high quality data, a lot of attention must be paid to the selection of MT site locations. In field data acquisition, there are many sources of electromagnetic noise. Ground motion can move the magnetic sensors and thus

cause noise in the magnetic field components. Power lines and radio transmitters can also create EM noise. The electric current from irrigation pumps, electric fence or cathodic pipeline protection can severely distort the electric field. Thus in site location selection, these noise sources should be avoided. In the Foothills, ground motion, power-lines, and cathodic protection of pipelines or gas well were the dominant sources of noise. A lot of effort was spent on site selection to find open areas in the forest, and in avoiding roads, power lines, pipelines or gas wells. Animals can be a danger to MT data acquisition. The cables at one MT stations were severely chewed by a herd of cows. This caused very bad MT data quality at that station.

4.2 Magnetotelluric time series analysis

In MT data processing, the apparent resistivity and the phase information were extracted as a function of frequency from the recorded time series. To do this, the time domain data were transformed into the frequency domain by Fourier transformation to calculate the impedance (equation 2.18). The apparent resistivity and phase were then calculated from the impedance (equation 2.19, 2.20). The remote reference technique was used to suppress bias (Gamble et al, 1979).

The time series were processed to yield estimates of apparent resistivity and phase data using the robust cascade decimation scheme of Jones and Jodicke (1984). In this robust cascade decimation scheme, the time series is divided into many short windows, with the length chosen to obtain the desired frequencies by Fast Fourier Transform (FFT). Then multiple solutions of the impedance equations are obtained at the desired frequencies. These solutions are stacked to estimate the impedance (Vozoff, 1991). Stacking must be done with autopowers or crosspowers since they will not sum to zero. Because only the random signals will stack to their long-term mean value of zero, the repetitive signals from radar, reflection seismic, power-line and etc, will not cancel out by

stacking. That is why these types of signals are considered as coherent noise in an MT survey.

One of the concerns in MT data processing is the suppression of noise. Although the data acquisition was carried out carefully, not all the stations are noise free, and noise-suppression techniques need to be used. The remote magnetic reference technique is based on the idea that the sum of the cross-products of two sets of incoherent random values will be zero. So if there is no correlation between the noise at two sites, multiplying the equations relating the Fourier components of electric and magnetic fields by a component of the magnetic field from the remote reference site, noise free estimates of impedance tensor can be obtained (Gamble et al., 1979).

By stacking the crosspower with a remote magnetic reference, all stations gave satisfactory apparent resistivity data up to a period of 100 seconds. Some gave good data to 1000 seconds, but data at the stations close to pipelines or gas well were significantly contaminated with noise. So the data was edited before inverting and modeling.

4.3 Tensor Decomposition

The tensor decomposition method used in the data processing is the multisite, multifrequency tensor decomposition technique of McNeice and Jones (2001). It is based on the Groom-Bailey decomposition (GB decomposition) analysis discussed in Chapter 2. In GB decomposition, by minimizing the least-squared misfit between the GB decomposition model factorization parameters and the measured data, the regional strike (θ), twist (T) and shear (S) can be estimated from equation 2.31. This recovers the regional two-dimensional geoelectric strike and then the MT data can be rotated to the geoelectric strike coordinate frame. In the multisite, multifrequency tensor decomposition technique, the decomposition analysis is extended from a single site and single frequency calculation to

statistically fit an entire dataset simultaneously. In this way the estimates of regional geoelectric strike can be improved and the regional geoelectric strike can be obtained (McNeice and Jones, 2001).

In practice a regional geoelectric strike for either the whole frequency band or just for a narrow frequency band can be calculated. In the Foothills, a geoelectric strike of N30°W is required by the multisite, multifrequency tensor decomposition analysis for all 26 stations over the whole frequency band. It agrees well with the regional geological strike (Figure 4-1). The resolved geoelectric strike, twist and shear of the whole frequency band data of each station are shown in Figures 4-4 and 4-5.

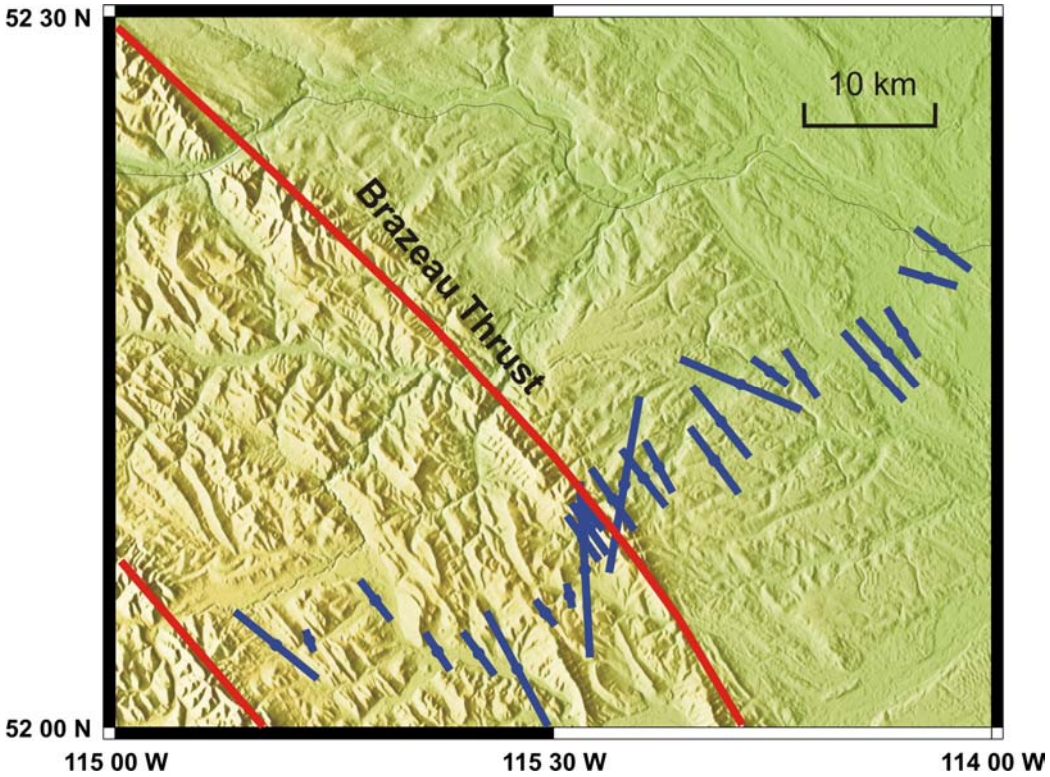

Figure 4-4: The geoelectric strike of the whole frequency band data at each station from the decomposition analysis. Red line shows the location of the Brazeau Thrust Fault. Dots show site locations, length of lines is inversely proportional to r.m.s misfit.

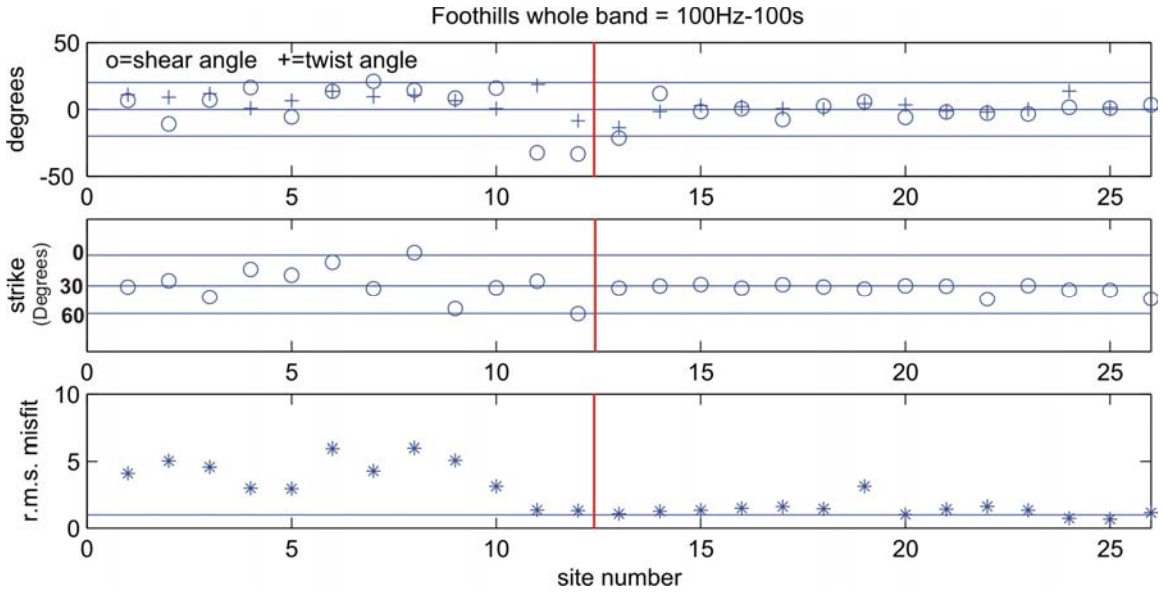

Figure 4-5: Shear angle, twist angle, geoelectric strike and r.m.s. misfit from the decomposition analysis of the whole frequency band of each station. The angles are in degrees clockwise from North. The red line shows the location of the Brazeau Thrust Fault.

Figure 4-4 shows that the geoelectric strikes of the MT stations are reasonably consistent along the profile. Figure 4-5 shows that the shear angle, twist angle and misfit are not high, which indicates that the geoelectric structure is approximately two-dimensional. The stations on the east side of the Brazeau Thrust Fault exhibit lower shear and twist angles and misfit than the stations to the west. This is consistent with the regional geological structure. East of the Brazeau Thrust is the Alberta Basin where the strata are less deformed and relatively two-dimensional. Thrust faults have developed west of Brazeau Thrust and cause severe deformation of the strata. Consequently the geological structure is more three-dimensional.

Figure 4-6 shows examples of the MT data before and after tensor decomposition. Stations FH003 and FH016 are located west of the Brazeau Thrust Fault. Changes between the data can be seen clearly. The stations FH015 and FH012 are located east of the Brazeau Thrust Fault. There is almost

no change between the data before and after decomposition and rotation. This is because the geological structure is very two-dimensional and the data were measured in the regional geological strike coordinate frame.

As previously discussed, the twist (*T*) and shear (*S*) tensors account for the determinable portion of the distortion matrix and can be resolved from the tensor decomposition analysis. When the data is rotated to the regional geoelectric strike coordinate frame, this part of the distortion can be recovered. The indeterminable parts of the distortion matrix, which are denoted as site gain (*g*) and anisotropy tensor (*A*) in equation 2.31, are unresolvable and are absorbed in the new impedance tensor, the regional two-dimensional impedance tensor Z_{reg}. So part of the static shifts can be corrected after the data is rotated by tensor decomposition, but the data still contain some distortion. From Figure 4-8(a) it can be observed that after the data is rotated to the regional geoelectric strike coordinate, the static shifts around the Brazeau thrust fault are still large in the pseudo section of both TE and TM modes. The residual static shifts will be removed in next step by static shifts correction.

4.4 MT sounding curves and pseusosections

Figures 4-7 show the MT sounding curves for all stations. At the MT sites in the Alberta Basin, (FH008 to FH026 in Figure 5-1), almost all TE apparent resistivity curves have the same shape, with constant apparent resistivity at high frequency, a small decrease from 1-0.3 Hz, and an increase below 0.3 Hz. This behavior shows that there are three resistivity layers in the Alberta Basin. i.e. a layer with medium resistivity at the top, an intermediate layer with low resistivity, and basement layer with high resistivity. The apparent resistivity shows the overall resistivity of all strata within a skin depth of the surface. The apparent resistivity curve is flat from 100-1 Hz and shows that down to the depth of the skin depth at 1 Hz the true resistivity of the strata is nearly constant. The frequency independent apparent resistivity causes a constant phase of 45°. The

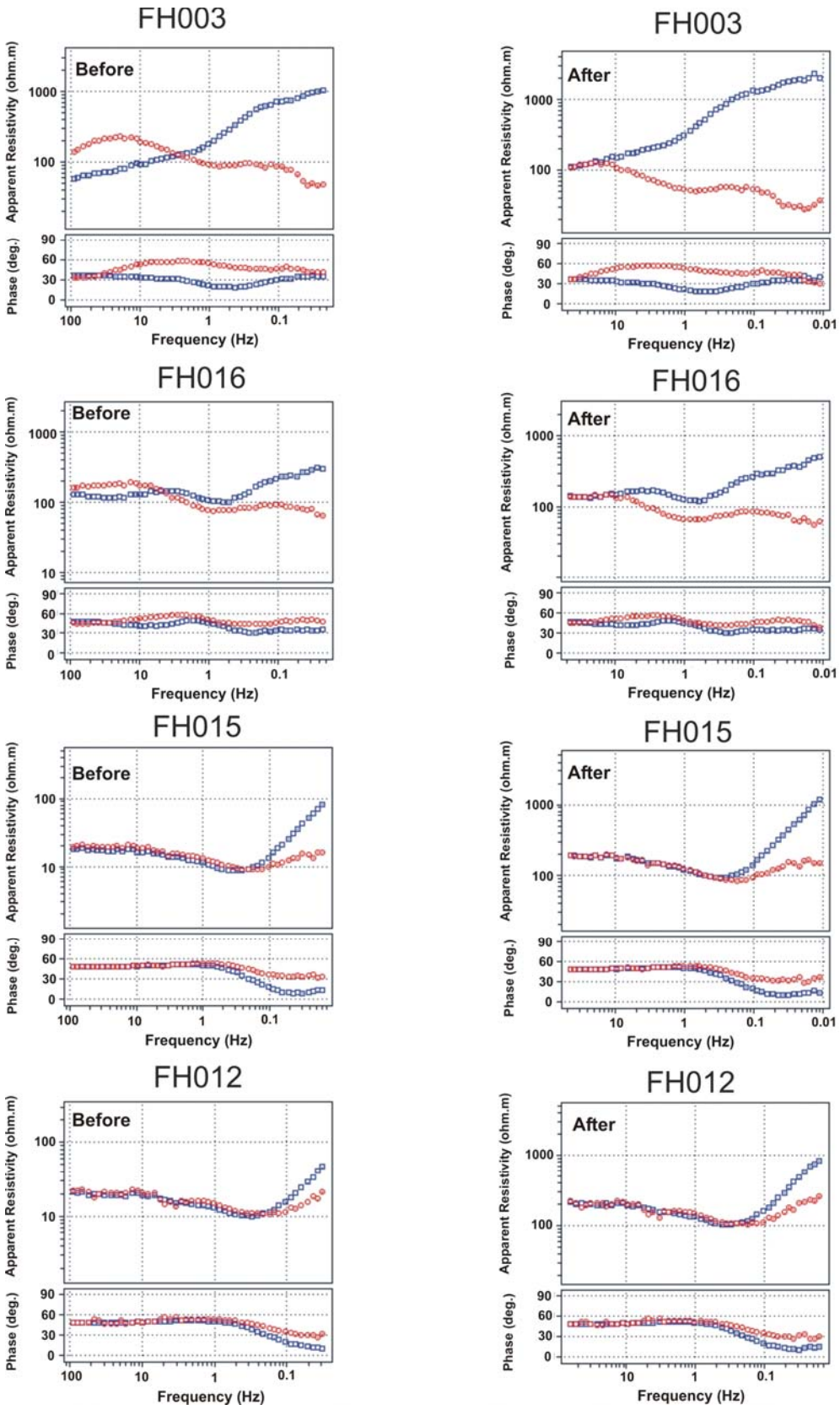

Figure 4-6: Comparison of MT data before and after tensor decomposition.

decrease of apparent resistivity between 1 Hz to 0.3 Hz shows that below the skin depth at 1 Hz more low resistivity strata are present, so the overall resisitivity goes down. The decrease in apparent resistivity causes the phase to increase. When the apparent resistivity increases at 0.3 Hz, this shows that below the skin depth at that frequency more high resistivity strata is present, and consequently decreases the phase.

Stations FH018-FH006 (locations shown in Figure 5-1) show a different shape of TE mode apparent resistivity curve with a low resistivity layer embedded between two high resistive layers. All these curves show a significant drop from above 100 Ωm to 10 Ωm and then an increase to above 100 Ωm. The variation of the frequency at which the apparent resistivity begins to decrease indicates that the depth of the low resistivity layer varies with horizontal position.

The apparent resistivity of station FH021, FH014, FH019 and FH020 (locations shown in Figure 5-1) are obviously distorted by static shifts. The apparent resistivity at high frequency jumps from around 100 Ωm to more than 1000 Ωm. The phase curves are not affected. These features can also be seen on the pseudosections (Figure 4-8(a)). The TE mode pseudosection clearly shows the large static shift around the Brazeau Thrust Fault. The pseudosection also shows the low resistivity nature of the Alberta Basin and the geometry of the low resistivity layer west of the Brazeau Thrust Fault. The TM mode pseudosection also shows the low resistivity Alberta Basin and the large static shifts around the Brazeau Thrust Fault. The TM mode pesudosection also indicates the presence of a resistive body between stations FH016 and FH018.

Due to the ground conditions in the Rocky Mountain Foothills, it is very difficult to dig a 1.5 m vertical hole for the vertical magnetic field component measurement. Thus vertical magnetic field data were recorded at just ten stations, and consequently the vertical magnetic field was not used in the data analysis.

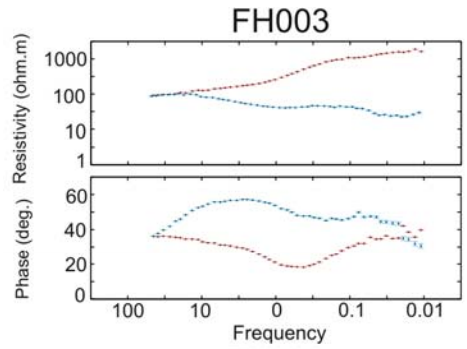
FH003
Resistivity (ohm.m)
1000
100
10
1
Phase (deg.)
60
40
20
0
100
10
0
0.1
0.01
Frequency

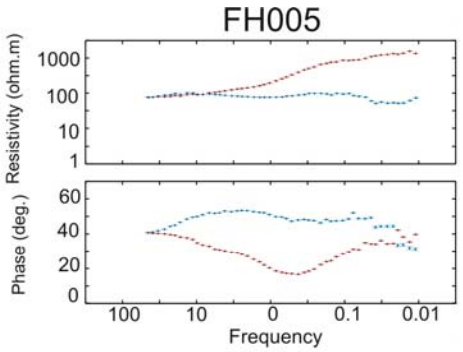
FH005
Resistivity (ohm.m)
1000
100
10
1
Phase (deg.)
60
40
20
0
100
10
0
0.1
0.01
Frequency

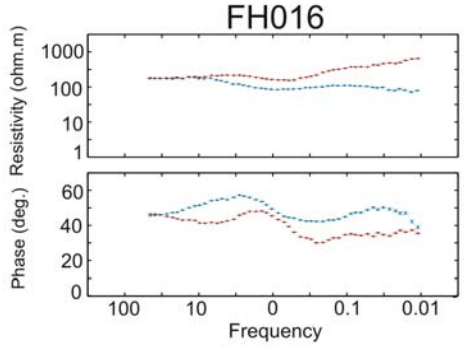
FH016
Resistivity (ohm.m)
1000
100
10
1
Phase (deg.)
60
40
20
0
100
10
0
0.1
0.01
Frequency

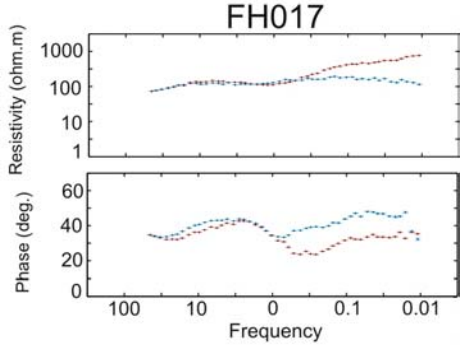
FH017
Resistivity (ohm.m)
1000
100
10
1
Phase (deg.)
60
40
20
0
100
10
0
0.1
0.01
Frequency

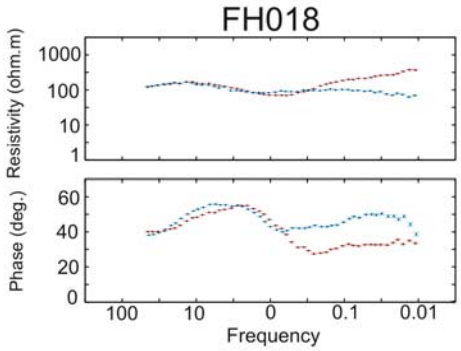
FH018
Resistivity (ohm.m)
1000
100
10
1
Phase (deg.)
60
40
20
0
100
10
0
0.1
0.01
Frequency

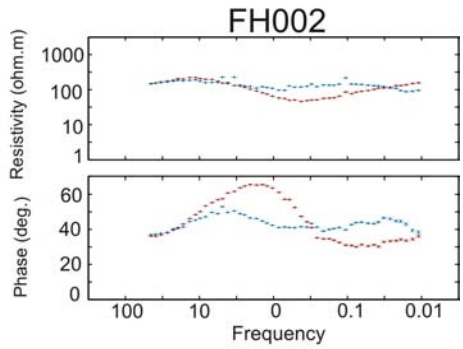
FH002
Resistivity (ohm.m)
1000
100
10
1
Phase (deg.)
60
40
20
0
100
10
0
0.1
0.01
Frequency

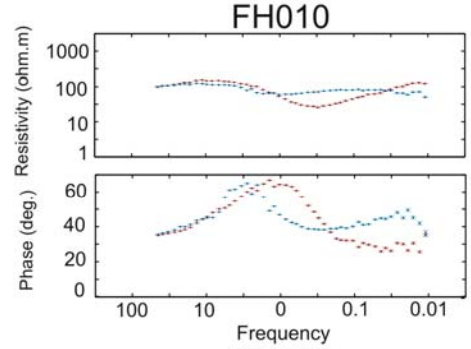
FH010
Resistivity (ohm.m)
1000
100
10
1
Phase (deg.)
60
40
20
0
100
10
0
0.1
0.01
Frequency

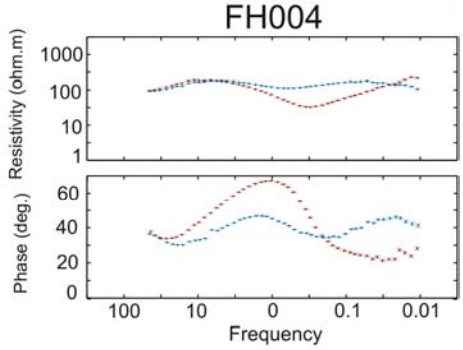
FH004
Resistivity (ohm.m)
1000
100
10
1
Phase (deg.)
60
40
20
0
100
10
0
0.1
0.01
Frequency

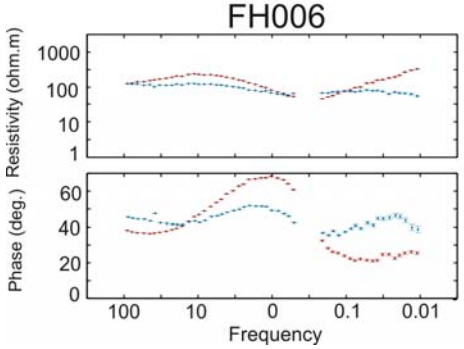
FH006
Resistivity (ohm.m)
1000
100
10
1
Phase (deg.)
60
40
20
0
100
10
0
0.1
0.01
Frequency

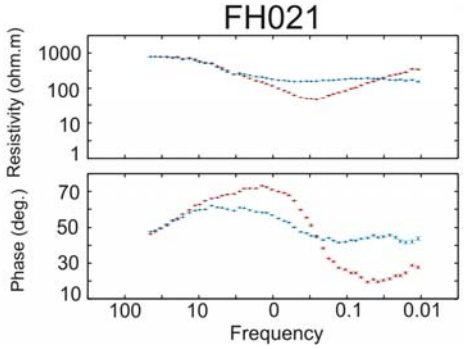
FH021
Resistivity (ohm.m)
1000
100
10
1
Phase (deg.)
70
50
30
10
100
10
0
0.1
0.01
Frequency

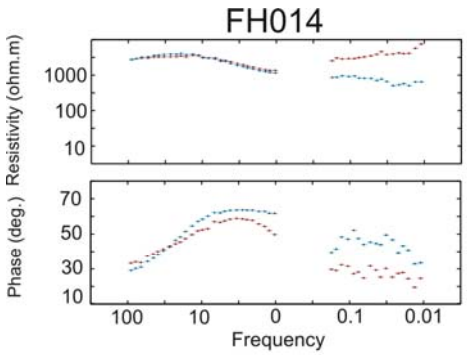
FH014
Resistivity (ohm.m)
1000
100
10
Phase (deg.)
70
50
30
10
100
10
0
0.1
0.01
Frequency

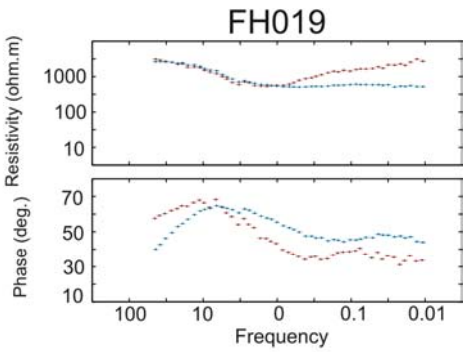
FH019
Resistivity (ohm.m)
1000
100
10
Phase (deg.)
70
50
30
10
100
10
0
0.1
0.01
Frequency

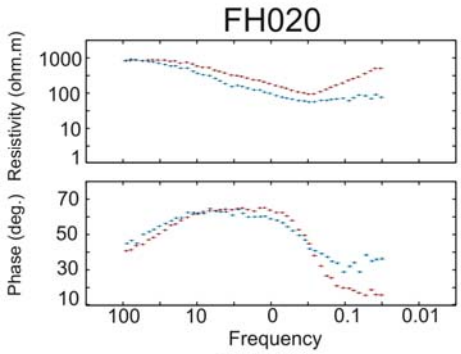
FH020
Resistivity (ohm.m)
1000
100
10
1
Phase (deg.)
70
50
30
10
100
10
0
0.1
0.01
Frequency

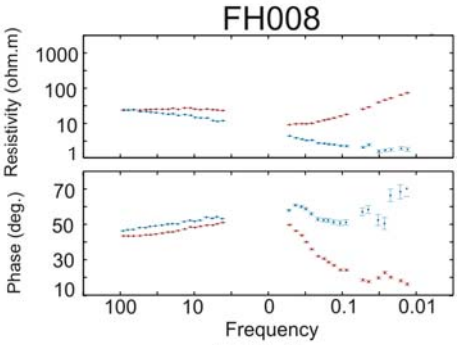
FH008
Resistivity (ohm.m)
1000
100
10
1
Phase (deg.)
70
50
30
10
100
10
0
0.1
0.01
Frequency

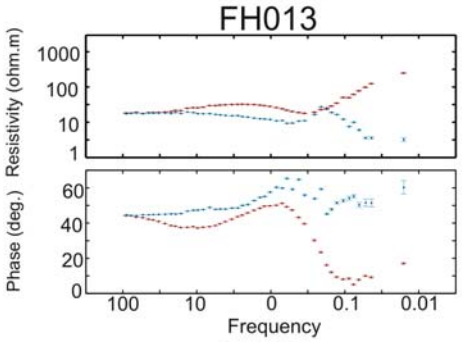
FH013
Resistivity (ohm.m)
1000
100
10
1
Phase (deg.)
60
40
20
0
100
10
0
0.1
0.01
Frequency

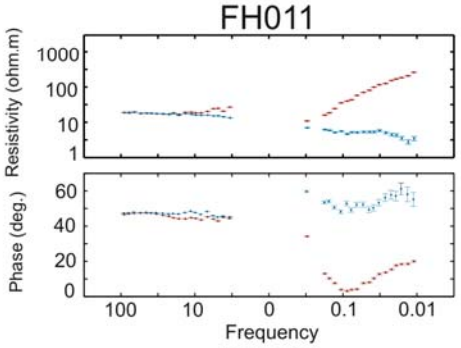
FH011
Resistivity (ohm.m)
1000
100
10
1
Phase (deg.)
60
40
20
0
100
10
0
0.1
0.01
Frequency

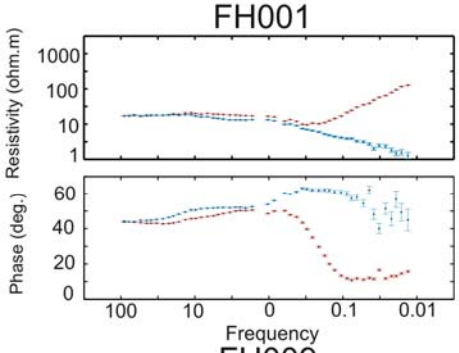
FH001
Resistivity (ohm.m)
1000
100
10
1
Phase (deg.)
60
40
20
0
100
10
0
0.1
0.01
Frequency

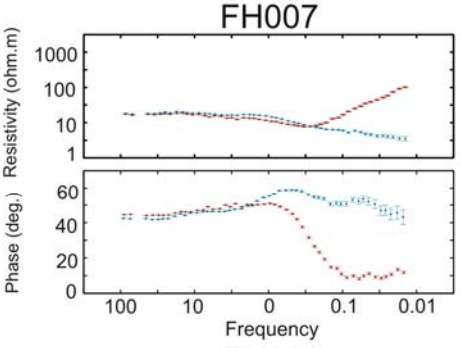
FH007
Resistivity (ohm.m)
1000
100
10
1
Phase (deg.)
60
40
20
0
100
10
0
0.1
0.01
Frequency

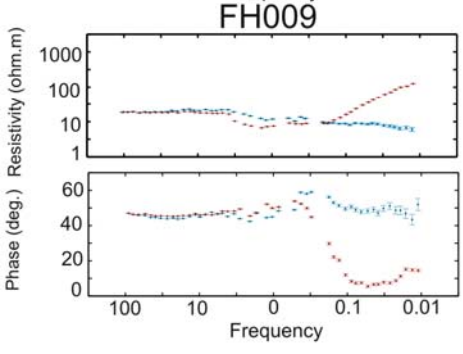
FH009
Resistivity (ohm.m)
1000
100
10
1
Phase (deg.)
60
40
20
0
100
10
0
0.1
0.01
Frequency

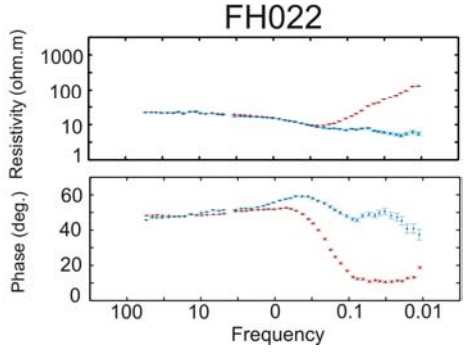
FH022
Resistivity (ohm.m)
1000
100
10
1
Phase (deg.)
60
40
20
0
100
10
0
0.1
0.01
Frequency

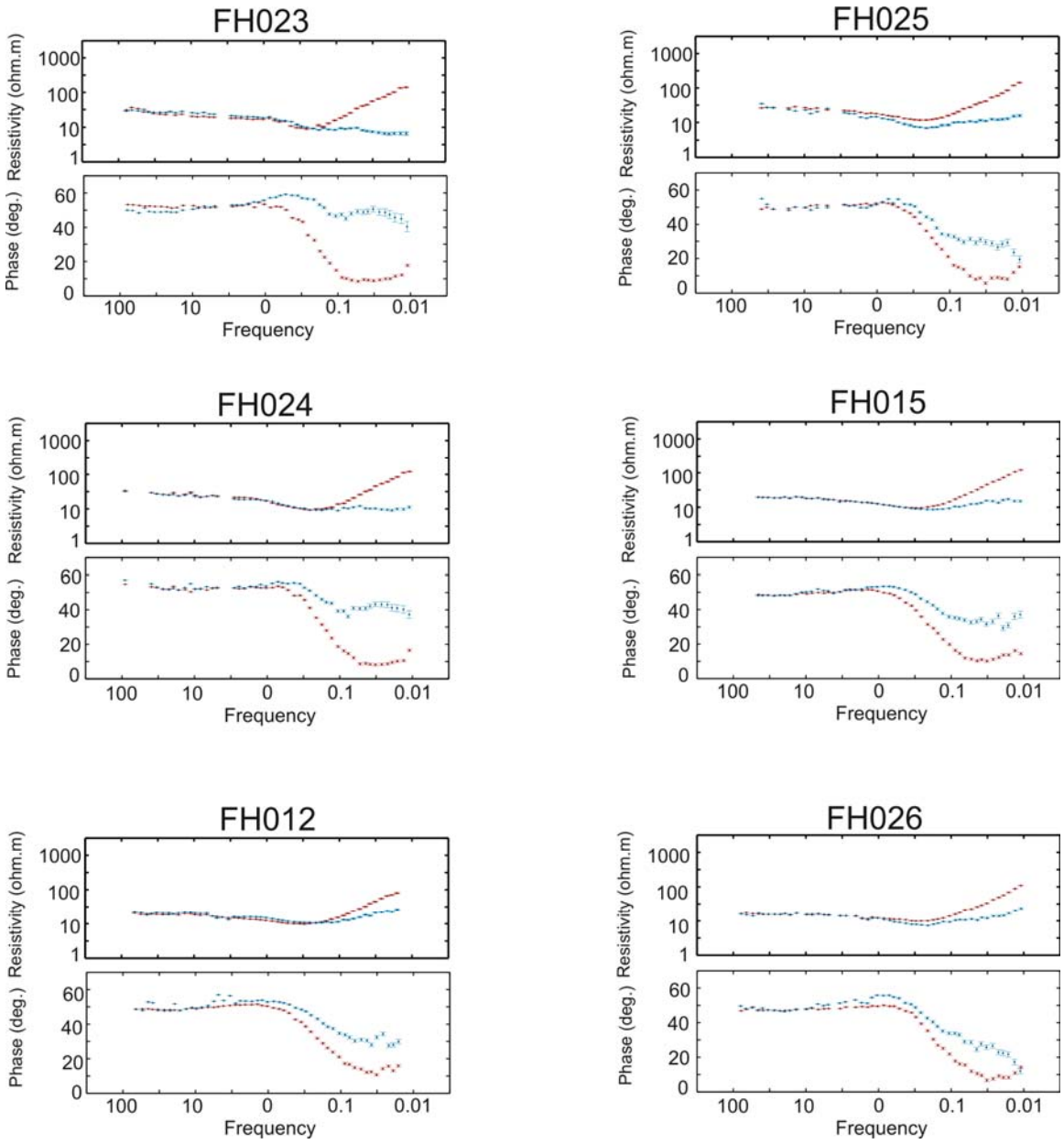

Figure 4-7: MT data after decomposition and rotation. TE mode data are shown in red and TM mode data are shown in blue.

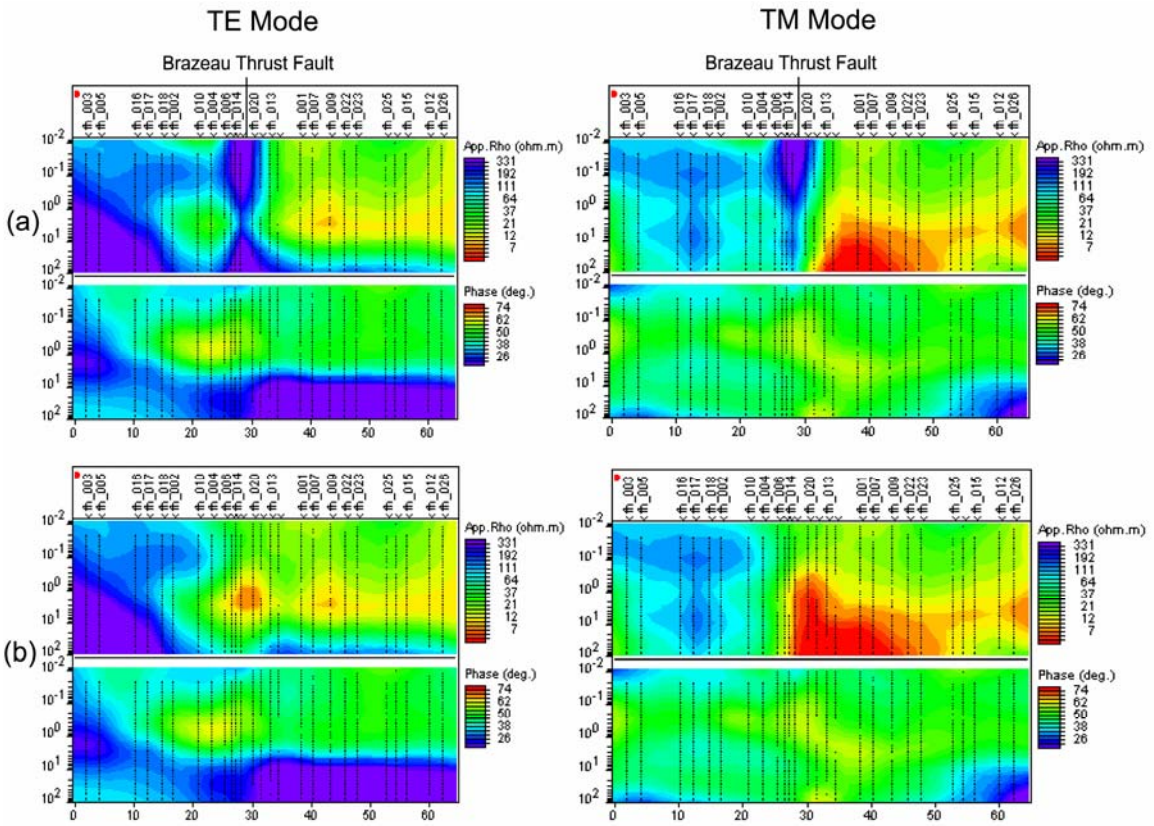

Figure 4-8: Comparison of pseudosections of TE and TM modes. (a): Pseudosections of data after tensor decomposition but before static shifts correction. (b): data after tensor decomposition and static shift correction.

4.5 Static Shift Correction

From Figures 4-8(a) it can be seen that there are large static shifts in both modes around the Brazeau Thrust Fault. As discussed in Chapter 2, the static shifts are caused by the electric field generated from boundary charges on surfacial inhomogeneties. The high resistivity contrast (1000 Ωm to 10 Ωm) between the carbonate thrust sheet and the Mesozoic clastic sediments could cause strong galvanic effects around the outcrop of the Brazeau Thrust Fault. Three-dimensional structure and topography might also contribute to the strong galvanic effect here. The four stations (FH021, FH014, FH019, FH020) are located in a narrow valley that cuts through the mountain at right angle to the regional geology strike. The along strike electric current could cause charges to

build up on the sides of the valley. The formation of the valley might be related to a fault with a strike perpendicular to the regional geological strike. This could also distort the MT data. These might be the reasons why such large static shifts are observed at this location.

Static shifts are routinely observed in field MT data. Many methods have been tried to remove the static shift from MT data. Some authors have tried to calculate the static shift from buried surface inhomogeneities using a theoretical calculation (Berdichevsky and Dmitriev, 1976; Larsen, 1977; Wannamaker et al., 1984). The theoretical calculation can provide a physical insight into the static shift of simple bodies, but there is rarely sufficient information about the near surface inhomogeneities in the survey area to adequately define a model. Thus it is difficult to apply such an approach to field MT data. Electro-Magnetic Array Profiling (Torres-Verdin and Bostick, 1992) and other averaging techniques based on the concept of spatial filtering were also developed to suppress static shifts. These techniques apply filters to an array of continuous electric field dipoles to average the electric field, and can suppress the galvanic effect in the electric fields. Such an approach could be used in the Foothills, but would require extra logistics for continuous MT profiling.

The most widespread technique used to correct static shift is the Transient Electromagnetic Inversion (Sternberg et al., 1988). The galvanic effect can severely distort the electric field, but the magnetic field is relatively unaffected. Transient ElectroMagnetic (TEM) sounding is a controlled-source time domain transient EM method. Because the transmitter signal strength is known, the apparent resistivity can be determined from a measurement of the magnetic field. The TEM data can be inverted to create a 1-D resistivity model. Then the predicted apparent resistivity curve of this model can be calculated by forward modeling. This curve can be used as a reference for static shift correction for the MT data collected at the same location as the TEM sounding. This method has

been used in many MT surveys (Pellerin and Hohmann,1990; Watts and Pince., 1998).

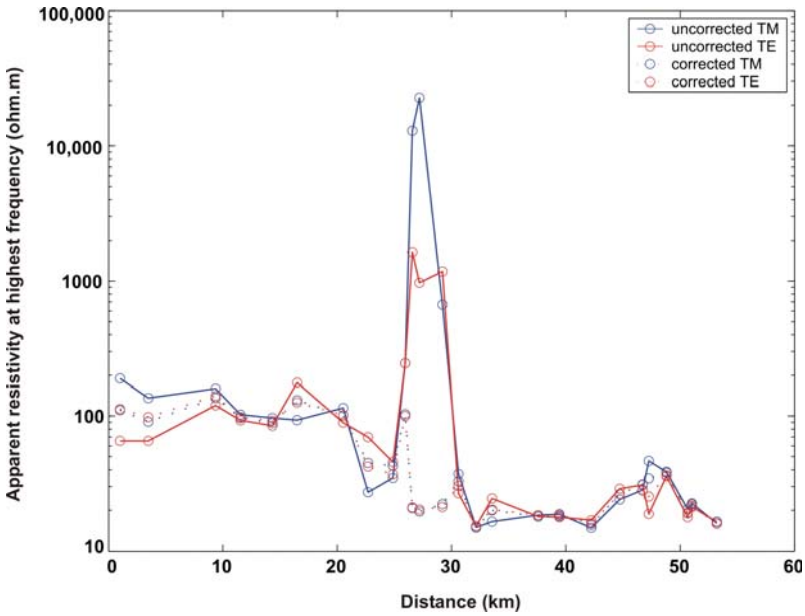

Figure 4-9: Comparison of apparent resistivity at the highest frequency (100 Hz). Solid line shows the apparent resistivity of highest frequency of the data before rotated to the regional geoelectric strike coordinate frame and static shift correction; Dashed line shows the apparent resistivity of highest frequency of the data after rotation to the regional geoelectric strike coordinate frame and static shift correction. The corrected MT data has been first rotated by tensor decomposition analysis.

The static shifts in this MT survey were corrected in two steps by an alternative method:

1. Based on the regional geology, the large static shifts around Brazeau thrust fault were corrected manually. From regional geological data and the pseudosection (Figure 4-8) of the MT data, the surface resistivity of Cretaceous clastic strata that outcrop at the east side of the Brazeau thrust fault is around 20 Ωm. The hanging wall is composed of carbonate strata, mainly Devonian, with a resistivity range from 100 to 200 Ωm. Thus the apparent resistivity curves of the 4 stations were shifted down to the same order as the neighboring stations. Figure 4-9 shows a comparison of

the apparent resistivity at the highest frequency (100 Hz), before and after correction.

2. Then the regularized inversion determines the small-scale static shifts. By allowing the static shifts to be free parameters, smooth inversion solves simultaneously for the resistivities and static shifts thus ensure that structures appearing in the models are not simply due to the incorrect removal of static shift (deGroot-Hedlin, 1991).

The analysis in this chapter shows that the quality of the MT data collected in this survey is good and the data are relatively two-dimensional, which matches the assumption of 2D MT analysis. Next a resistivity model will be created by two-dimensional MT inversion of the corrected MT data.

Chapter 5

Inversion of MT data and sensitivity tests

In the previous chapter, the MT data collected in the Rocky Mountain Foothills were described and it was shown that a two-dimensional analysis is appropriate. To fully interpret the MT data, it is necessary to convert the frequency domain apparent resistivity and phase into a model of electrical resistivity as a function of horizontal position and depth.

5.1 Inversion of MT data

If ***m*** is used to denote the model (the distribution of physical properties), ***F*** denotes the kernel function (a mathematical description of the physical process under study), ***d'*** denotes the predicted data (the responses caused by the model), then the forward modeling can be written as:

$$d' = Fm.$$

If the measured data is ***d,*** then the fit of the model to the data can be judged by comparing ***d*** and ***d'***. This trial and forward modeling is one way to interpret geophysical data.

In field studies, it is usual to start with the observed data (***d***) and a method is sought to obtain the model ***m***. Inversion is the mathematical procedure used to obtain the distribution of true physical properties from observed data. This inversion problem can be written as

$$m = F^{-1} d$$

For the forward problem, a unique solution ***d'*** can always be found. However, the inverse problem does not always give a unique answer for **m**. If a sufficient amount of accurate data could be obtained, then a unique solution to the inverse

problem could be found. In reality, the quantity of measured data is always finite and contains noise. In this situation, the inversion is a non-unique problem, which means many solutions can be found to fit the data. This was shown to be the case for electromagnetic data by Parker (1980). To overcome non-uniqueness and select a preferred model, additional constraints must be imposed on the model solution.

As the MT method has developed into an effective and economical geophysical exploration method, the solution of the MT inverse problem has attracted the attention of many geophysicists. Under ideal conditions, with an infinite amount of noise free data, Tikhonov (1965) showed that unique solution could be derived. However, with real MT data, the inversion of MT data is non-unique, i.e. a finite set of magnetotelluric data containing noise can yield an infinite number of geoelectric models. To overcome non-uniqueness additional constraints must be added to the solution. This procedure was termed regularization by Tikhonov (1977). The constraint used here is to seek the smoothest model in a spatial sense that fits the data. It means that the resistivity model should be as spatially smooth as possible, but also fit the observed MT data. This approach is suitable for MT data since it reflects the diffusive nature with which MT signals travel in the Earth.

The fit of the measured MT data (ρ^{data}, φ^{data}) to the calculated response (ρ^{resp}, φ^{resp}) of the inversion model can be quantified by evaluating the root-mean-square (r.m.s.) misfit. If apparent resistivity and phase data are available at N sites and M frequencies, the r.m.s. misfit, *m*, is defined as:

$$m = \sqrt{\frac{1}{2NM}\sum_{j=1}^{M}\sum_{i=1}^{N}\frac{\left(\rho_{ij}^{data}-\rho_{ij}^{resp}\right)^2}{e^{r}{}_{ij}^{2}}+\frac{1}{2NM}\sum_{j=1}^{M}\sum_{i=1}^{N}\frac{\left(\varphi_{ij}^{data}-\varphi_{ij}^{resp}\right)^2}{e^{p}{}_{ij}^{2}}} \qquad (5.1)$$

where e^r and e^p are the standard error associated with the resistivity and phase data respectively. In practice an error floor is used to give a more uniform fit to a data set with variable errors.

An r.m.s. misfit significantly larger than one indicates that the inversion is incapable of fitting the MT data. It can also indicate that the noise in the data is larger than the defined errors or that three-dimensional effects are presented in the data, which cannot be physically reproduced by a two-dimensional inversion algorithm. A misfit significantly less than one indicates either that the errors are too large, or that the data is being over fit. In the second scenario, the resistivity model usually appears very rough. Generally an r.m.s misfit between 1 and 2 is optimal.

Tikhonov (1977) defined a regularized solution to the MT inverse problem as finding the model $\mathbf{m}$ that minimizes the objective function:

$$S(\mathbf{m}) = (\mathbf{d} - F(\mathbf{m}))^T \hat{R}_{dd}^{-1} (\mathbf{d} - F(\mathbf{m})) + \tau \| L(\mathbf{m} - \mathbf{m}_o) \|^2 \qquad (5.2)$$

where **d** is the observed data vector, *F* is the forward modeling operator, **m** is the unknown model vector, $\hat{R}_{dd}$ is the error covariance matrix, *L* is a linear operator, $\mathbf{m}_o$ is the reference model, and τ is the user defined regularization parameter. In equation 5.2, the first term represents the data misfit and the second term measures the acceptability of the model in terms of spatial smoothness and closeness to the reference model. The smoothness of inversion model can be controlled by changing the regularization parameter τ.

5.2 Inversion of the Foothills MT data

After the MT data were rotated to a N30°W coordinate frame and the static shifts were corrected, the frequency domain MT data were then converted into a two-dimensional geoelectric model with the nonlinear conjugate gradient (NLCG) inversion code of Rodi and Mackie (2001). This algorithm minimizes the Tikhonov regularization objective function and solves for a smooth model that fits the MT data. The input data were the apparent resistivity and phase for both

modes in the frequency range from 100 Hz to 0.01 Hz. Topography is explicitly modeled in the inversion.

The decision to only use data in the frequency band 100-0.01 Hz was based on the data quality and the target of this research. As stated in Chapter 4, the overnight recording provides estimates to a frequency of 0.001 Hz, but at many stations the data quality is poor below 0.01 Hz. The purpose of this research is to image the structures in the thrust and fold belt, and thus imaging to a depth of 10 km is adequate. According to Figure 2-2 and the geoelectric structure of the Foothills, 0.01 Hz is low enough to image to a depth of 10 km.

After trying many combinations of inversion parameters, the model in Figure 5-1 (a) was obtained and gives a good balance between fitting the MT data and being smooth. The inversion parameters for the inversion to produce this model are listed in the Table 5-1.

Table 5-1 **Model Inversion parameters**

Input data	Apparent resistivity and phase data for TE and TM modes. Static shifts corrected. 100 Hz to 0.01 Hz; 13 frequencies per decade.
Parameters for Smooth Inversion	Solve for Smoothest model: Regularization Laplacian=Standard grid Laplacian operator; Regularization order=minimize integral of $\|\text{Laplacian}\|^2$
Error floor	20% for apparent resistivity and 10% for phase of both modes
τ for smoothing operator	τ=30
Weight function	α=5 β=1
r.m.s.	Initial: 6.927; Final: 1.706 ;
Iterations	129

Error floors were used in the inversion. They replace the data errors when the data errors are smaller than the error floor. The error floor is the estimated noise level for the data. A change in the error floor can influence the final r.m.s. misfit of the inversion model. If the estimated error floor is much smaller than the actual noise level of the data, the data are hard to fit and a high r.m.s. misfit is observed. If the estimated error floor is much larger than the actual noise level of the data, the inversion model produces a low misfit but might lose some information through under fitting the data. In practice first several inversions are run with different error floors until the model achieves a misfit between 1 and 1.5. Then other parameters are adjusted to get a smoother model. α is the factor that multiplies horizontal derivatives. Increasing α can increase the horizontal smoothness, and this was found to be necessary in this study.

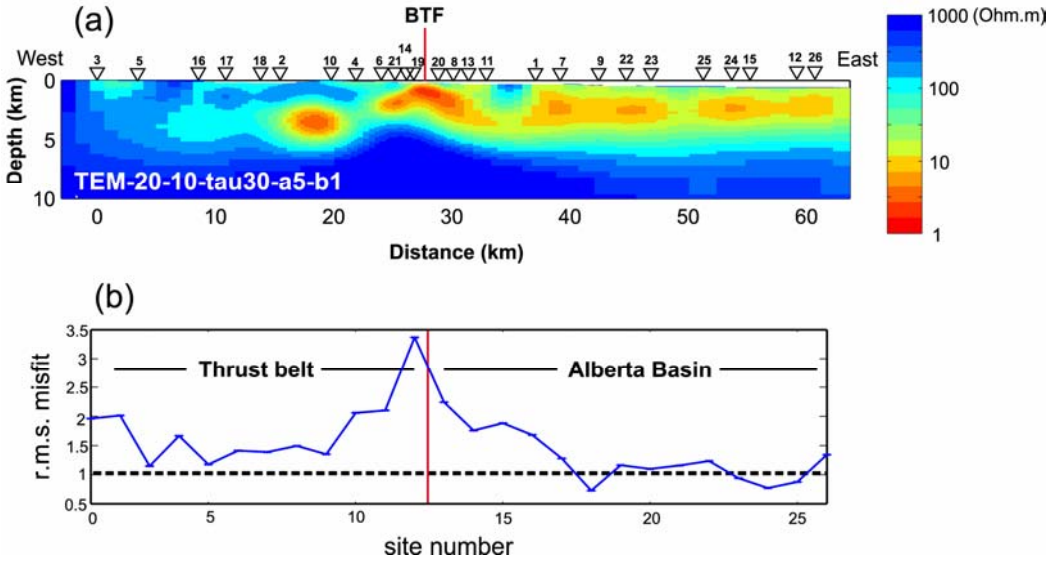

Figure 5-1: (a) The optimal inversion model. Triangles at the surface with numbers on the top indicate the location of MT sites. BTF=Brazeau Thrust Fault. (b) r.m.s. misfit as a function of station number. Dashed line shows the ideal fit, red line shows location of the Brazeau Thrust Fault.

Figure 5-1(b) shows the r.m.s. misfit at each MT station. The misfit is generally satisfactory, with a better fit in the eastern part of the model. This is consistent with the tensor decomposition analysis. The highest misfits are observed close to

Brazeau Thrust Fault (021, 014, 019 and 020) that might be affected by surfacial three-dimensional inhomogeneity. The fit to the three-dimensional data is poor for a two-dimensional inversion. Thus lower r.m.s. misfit in the east indicates a relatively two-dimensional structure.

Figures 5-2 (a) and (b) show the response of apparent resistivity and phase data for all sites. These figures show that the responses fit the data quite well and generally the apparent resistivity fits better than the phase. Although the response at many sites are not within the error bars, they generally recover the shape satisfactorily. The stations close to Brazeau Thrust Fault (FH021, FH014, FH019 and FH020) have a poor fit to the TE mode data. The fits to the TM mode data are generally better. This is as expected because the TE mode does not include the physics of the galvanic effect. Thus three-dimensional features have more influence on the TE mode data (Wannamaker et al., 1984; Berdichevsky et al., 1998). The response curve of apparent resistivity for the TE mode at FH021 generally recovered the shape of the data. The fit of the TE mode apparent resistivity at station FH014 is good above 1 Hz, but below 1 Hz the fit becomes poor. The fit of the TE mode data at station 19 is poor, the response is very different from the data. The fit of the TE mode at station FH020 is better and the apparent resistivity response recovers the shape of the data curve. The other two stations that the inversion model does not fit well are FH003 and FH005, which are close to the Front Ranges. The TE mode fit at these two stations is also poor, but the fit of the TM mode is satisfactory.

Figure 5-3 shows the fit of data in pseudosection format. It can be seen that the fit of apparent resitivity and phase data is generally good, but the phase residuals appears quite rough. The reason for this is that the phase is sensitive to the change of apparent resistivity and a smaller standard error was used in the residual calculation. As observed in Figure 5-3 (b) and (c) the shape is well recovered but the amplitude is not recovered well. The situation for the TM mode is similar to the TE mode.

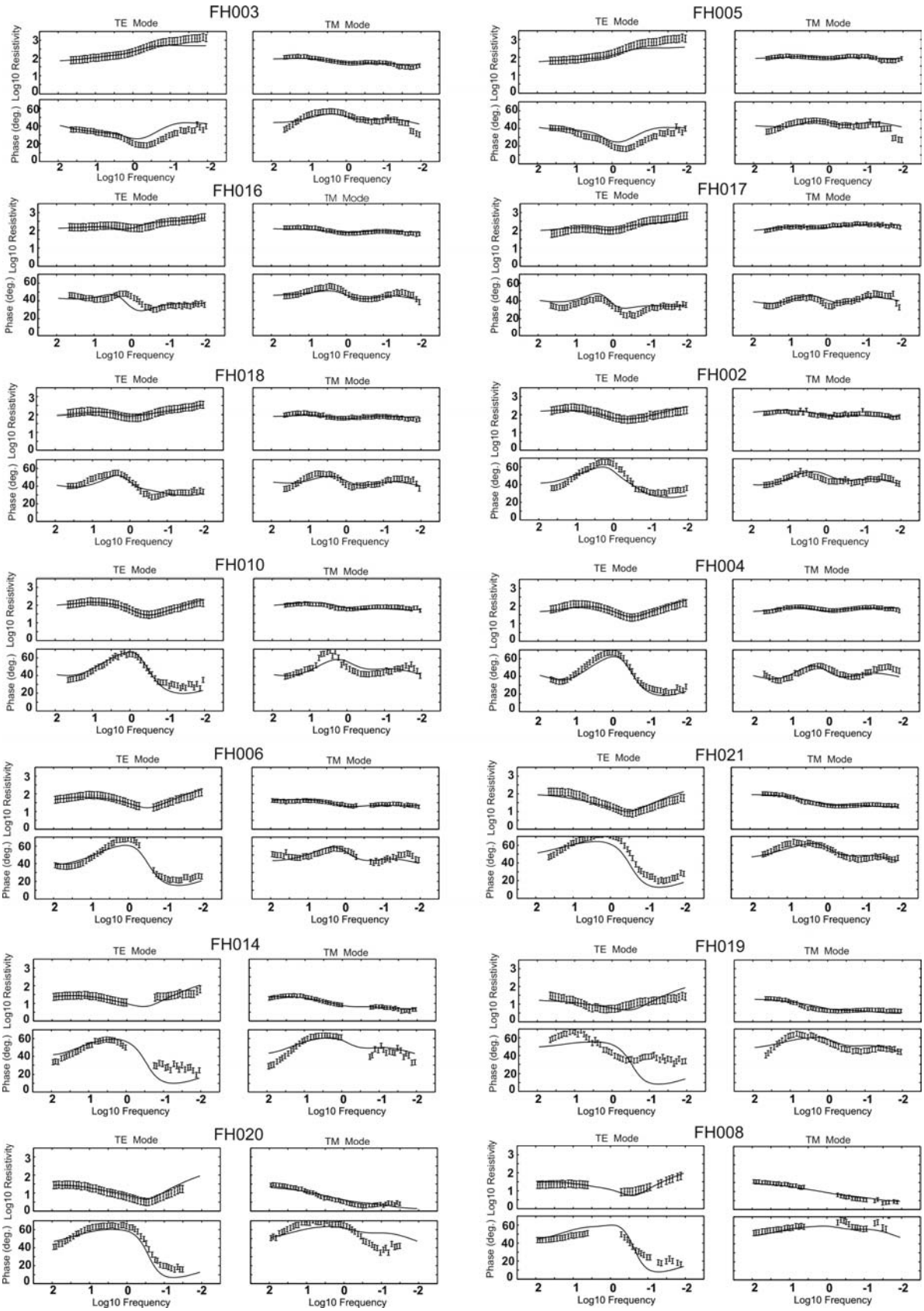
FH003
FH005
FH016
FH017
FH018
FH002
FH010
FH004
FH006
FH021
FH014
FH019
FH020
FH008
TE Mode
TM Mode
Log10 Resistivity
Phase (deg.)
Log10 Frequency

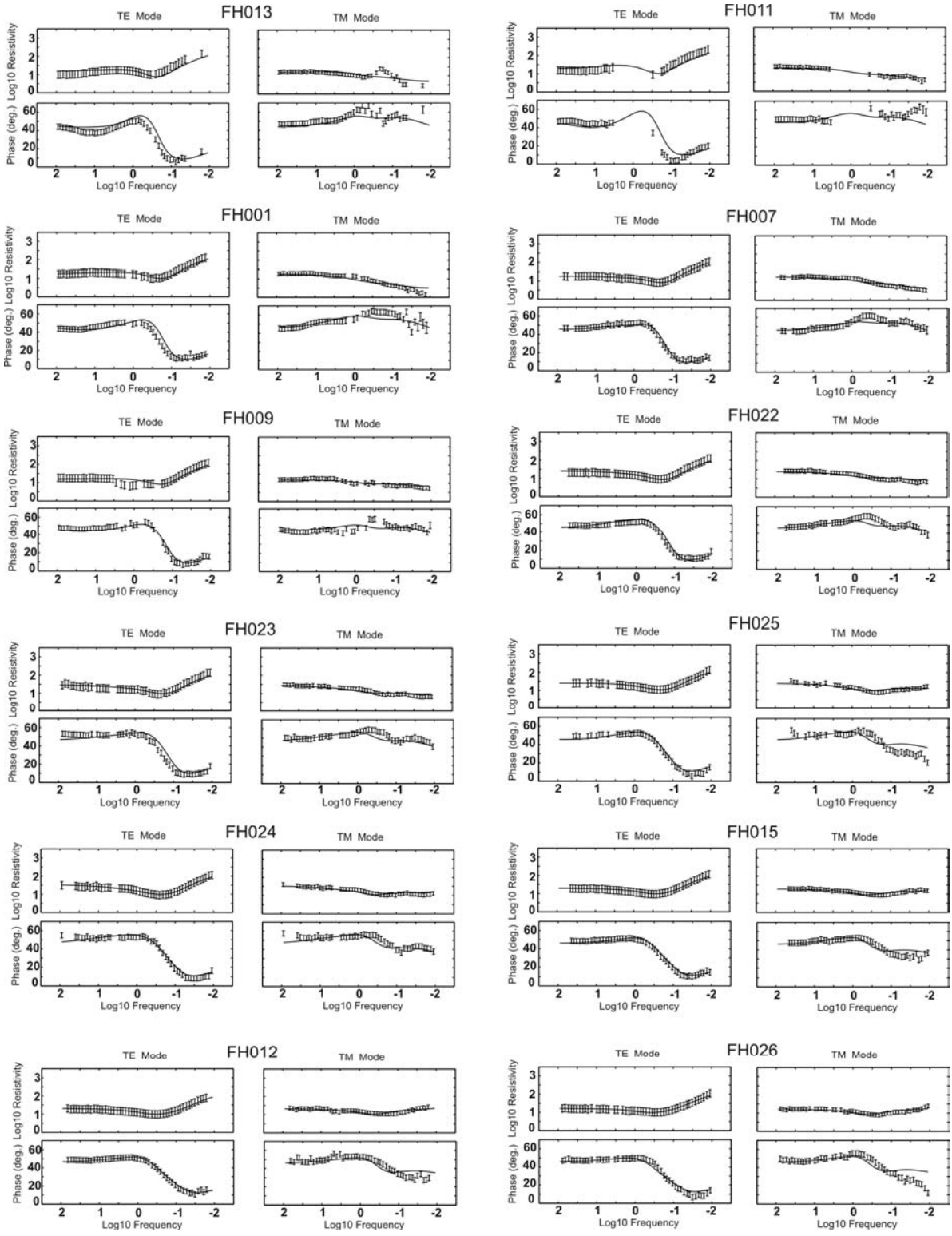

Figure 5-2: Sounding curves and model response of MT stations. Solid line shows the model response, and dots with error bars show the observed data.

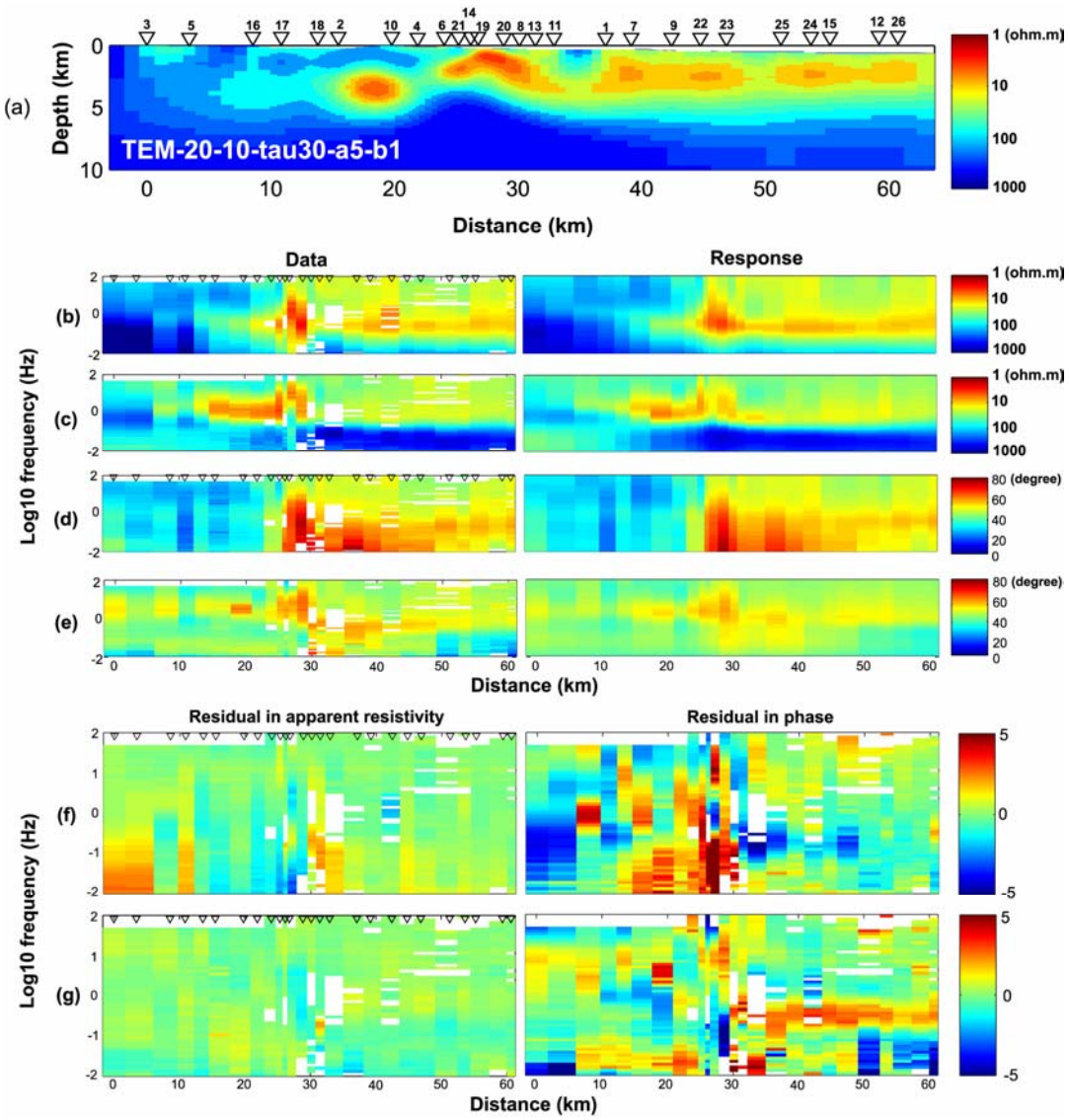

Figure 5-3: (a), the inversion model; (b), the apparent resistivity data and the inversion model response of the TE mode; (c), the phase data and the inversion model response of the TE mode; (d), the apparent resistivity data and the inversion model response of the TM mode; (e), the phase data and the inversion model response of the TM mode. (f), the residuals in the TE mode apparent resistivity and phase data; (g), the residuals in TM mode apparent resistivity and phase data. The residual is the difference between the model response and the data normalized by the standard error. The white blocks indicate where there is no data.

From the above discussion, it can be seen that the inversion model gives a good fit to the observed data. Another feature of the inversion model is to determine if the inversion model is too rough or too smooth. To answer this question, several inversions were run with different values of τ.

5.3 inversion model smoothness test

The MT inversion code generates a smooth model by minimizing the objective function S (equation 5.2). The trade-off between data misfit and model smoothness is controlled by the regularization parameter τ. The NLCG algorithm does not determine τ automatically, so several inversions were run with different values of τ to find the optimal model that gives the best compromise between spatial smoothness and the r.m.s. misfit.

Figure 5-5 shows that as τ increases, the r.m.s. misfit also increases. Figure 5-4 shows the inversion models for different values of τ. From these models, it can be seen that with the increase of τ, the model become smoother. Once τ>30, there is no significant difference between the models. So the inversion model with τ=30 was chosen as the preferred solution.

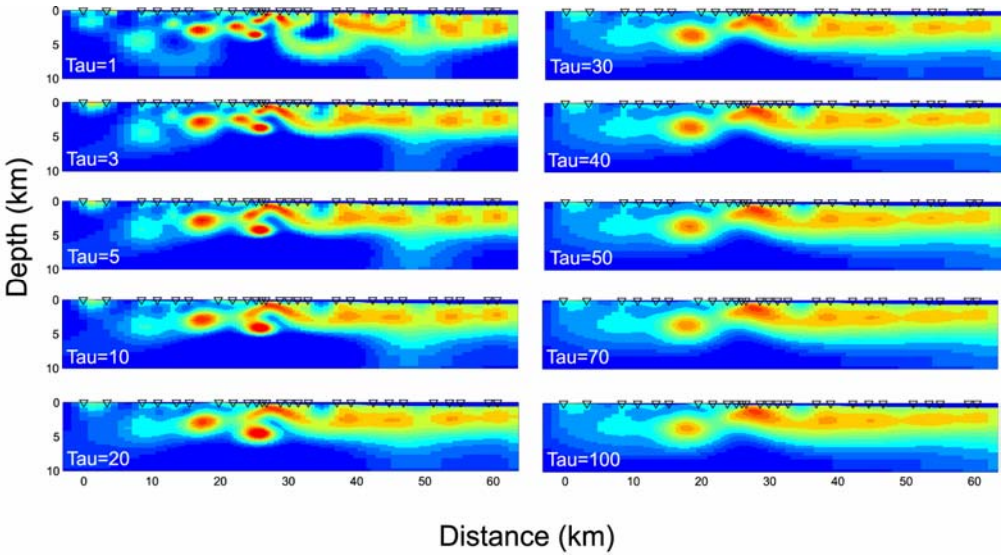

Figure 5-4: Inversion models with different τ values

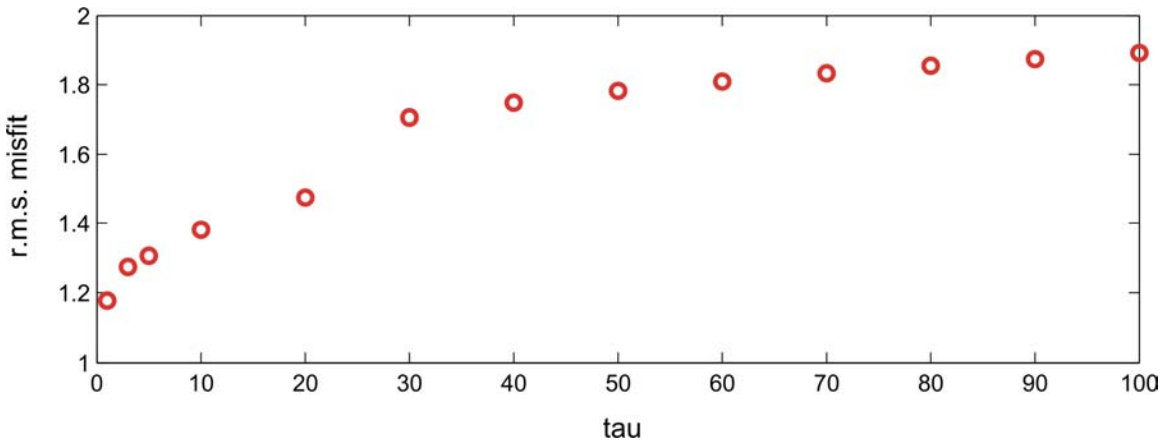

Figure 5-5: Variation of r.m.s. misfit with τ

5.4 Other inversion models

In addition to the inversion model shown in Figure 5-1, many inversions with different combinations of inversion parameters were tried. Figure 5-6 shows some typical inversion models. All these inversion models used a standard grid Laplacian operator as the regularization Laplacian to solve for the smoothest model. The weight functions in the inversion were the same: alpha=5, beta=1.

Dataset 1	MT data after static shifts correction and tensor decomposition
Dataset 2	MT data after tensor decomposition; no static shifts correction
Dataset 3	MT data without tensor decomposition; no static shifts correction

Other inversion parameters are shown in the Table 5-2.

Table 5-2 **Model Inversion parameters**

Model name	Input data	TE, TM ρ_a error floor	TE, TM φ error floor	τ	Initial r.m.s.	Final r.m.s.	Iterations
TEM-20-10-tau30-a5-b1	TE and TM mode of dataset 1	20%	10%	30	6.927	1.706	129
TE-20-10-tau30-a5-b1	TE mode of dataset 1	20%	10%	30	6.944	1.543	199
TM-20-10-tau30-a5-b1	TM mode of dataset 1	20%	10%	30	6.910	1.027	163
Data2-TEM-20-10-tau30-a5-b1	TE and TM modes of dataset 2	20%	10%	30	6.958	2.546	84
Data2-TE-20-10-tau30-a5-b1	TE mode of dataset 2	20%	10%	30	7.231	3.135	109
Data2-TM-20-10-tau30-a5-b1	TE mode of dataset 2	20%	10%	30	6.673	0.993	101
TEM-20-10-tau30-a5-b1	TE and TM mode of dataset 1	30%	15%	30	4.621	1.224	120

The inversions (b) and (c) used the same inversion parameters as the preferred model shown in Figure 5-1, but the input data were different. The inversion model for just the TE mode is quite rough. The TM mode data is relatively easy to fit, but it doesn't give a good image of the low resistivity body between distance 14-21 km at depth 2-4 km. This is because the TM mode is somewhat insensitive to the presence of a low resistivity body. The models (d), (e) and (f) used data in which the static shifts have not been corrected and are obviously perturbed around the Brazeau Thrust Fault. The model F used a larger error floor than the preferred model and obtained a smaller misfit, but this does not represent a better fit to the data. The decrease in misfit is caused by the increase of error floor, which also causes a smaller initial misfit. It can be observed that the model is as smooth as the model with tau=70 in Figure 5-4.

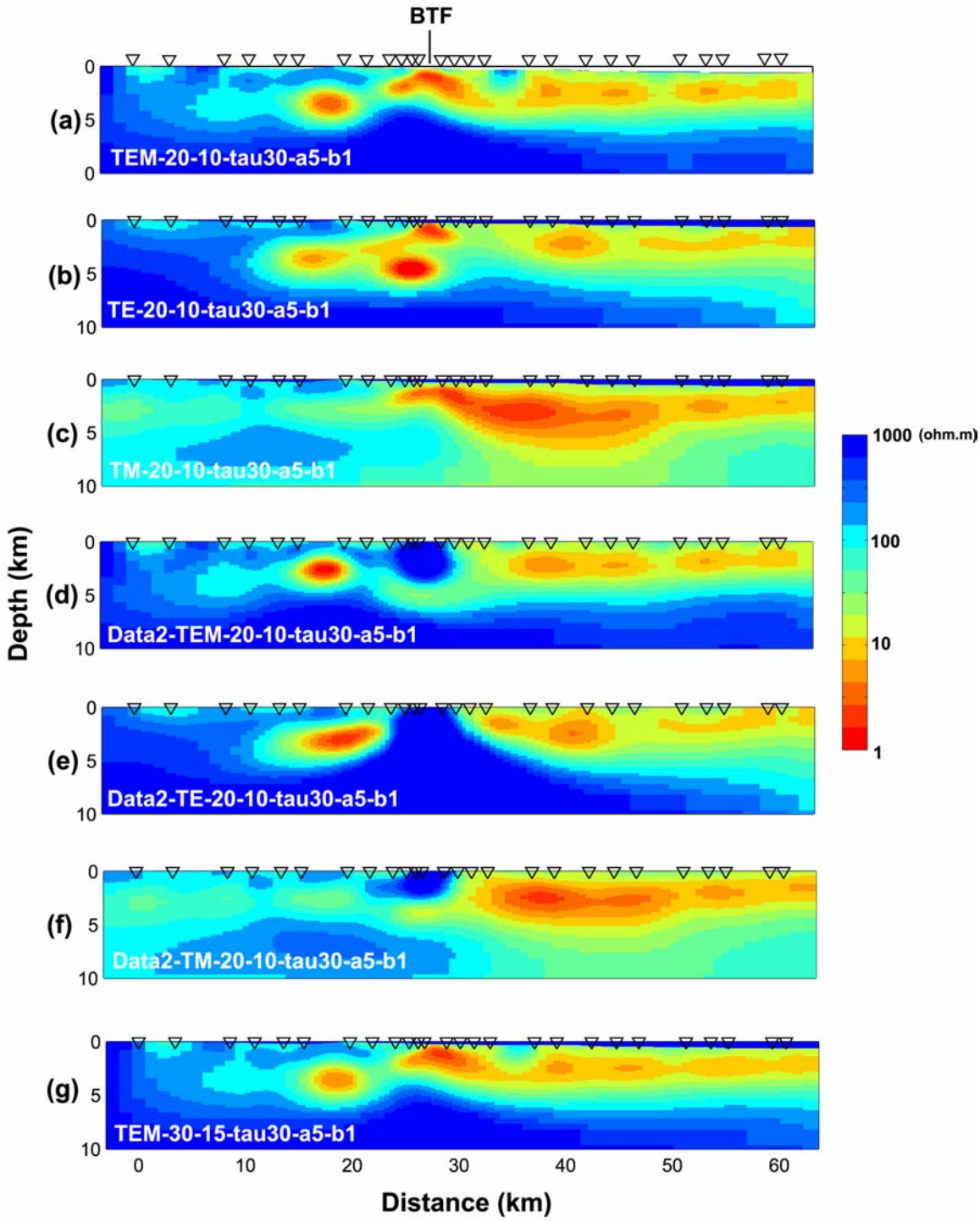

Figure 5-6: Comparison of inversion models with different control parameters. BTF=Brazeau Thrust Fault. (a) is the prefered model that will be used in the interpretation.

5.5 Testing of features in the inversion model

Some distinct features (B, C, D and E in Figure 5-7) can be observed in the inversion model. These features could be real resistivity structures. However the spacing of MT stations is not ideal and these features could be artifacts of the station spacing. Before interpreting these features, it is important to establish if they are required by the MT data.

In the forward modeling, various features in the inversion model were modified and the response of the changed model was calculated. The comparison of the fit of the responses of the inversion model and the forward model to the data can clarify if the feature is required by the data.

Figures 5-8 shows that when the high resistivity feature D is removed, the data fit at adjacent stations gets worse, especially at station FH001. This shows that this high resistivity gap (feature D) is required by the MT data. Figure 5-9 show that feature C is required by the data, since removing feature C degrades the fit to the data. In Forward Model B (Figure 5-10) the high resistivity gap (feature B), was replaced by low resistivity layer, so that the low resistivity layer is continuous. The responses at the three adjacent stations show a significantly worse fit to the data. Thus Feature B appears to be required by the MT data. The Forward model E (Figure 5-11) was generated to test the sensitivity of the MT data to the resistivity of the Cretaceous strata between FH016 and FH018 at depths. The forward model shows data fit is significantly worse when the resistivity of this feature is decreased. Thus the resistivity at this part is higher than feature C.

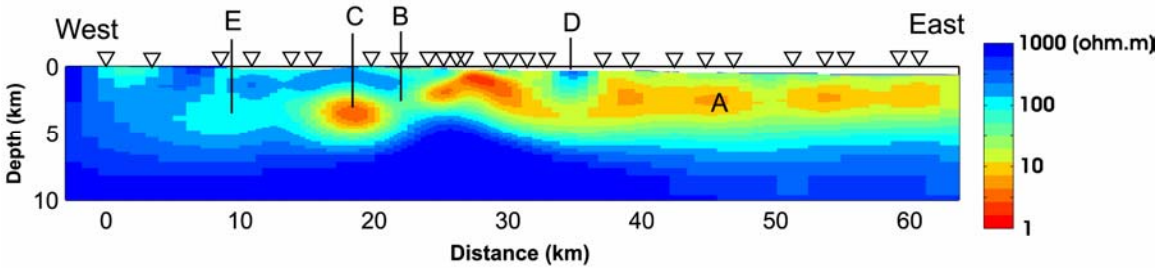

Figure 5-7: The distinct resistivity features in the MT Inversion model.

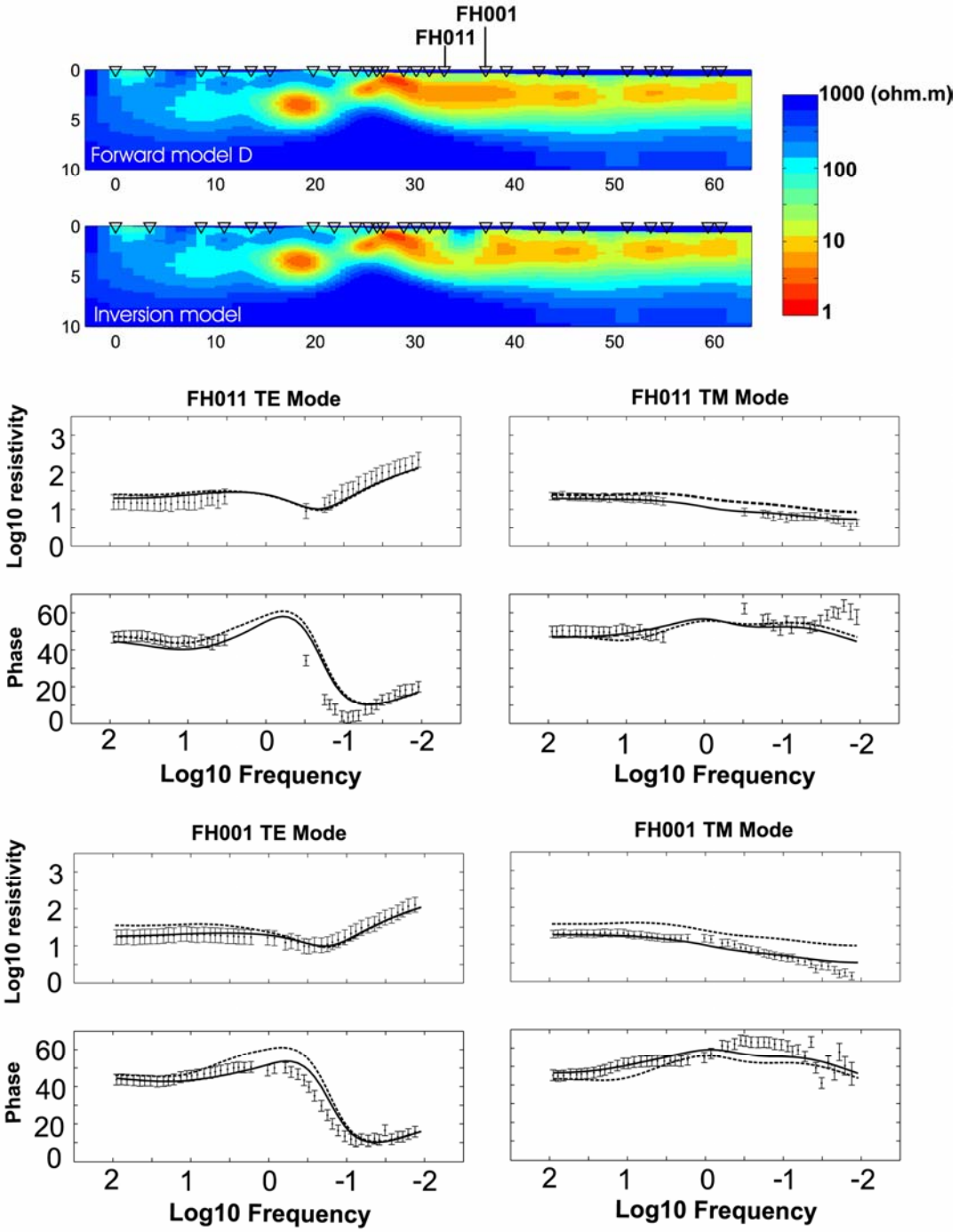

Figure 5-8: Comparison between Forward Model D and the inversion model. Solid line is the responses of the inversion model, dash line is the responses of the forward model D. Dots with error bar is the measured MT data. The r.m.s misfit of station FH011 increases from 1.68 to 2.06. The r.m.s misfit of station FH001 increases from 1.28 to 2.95.

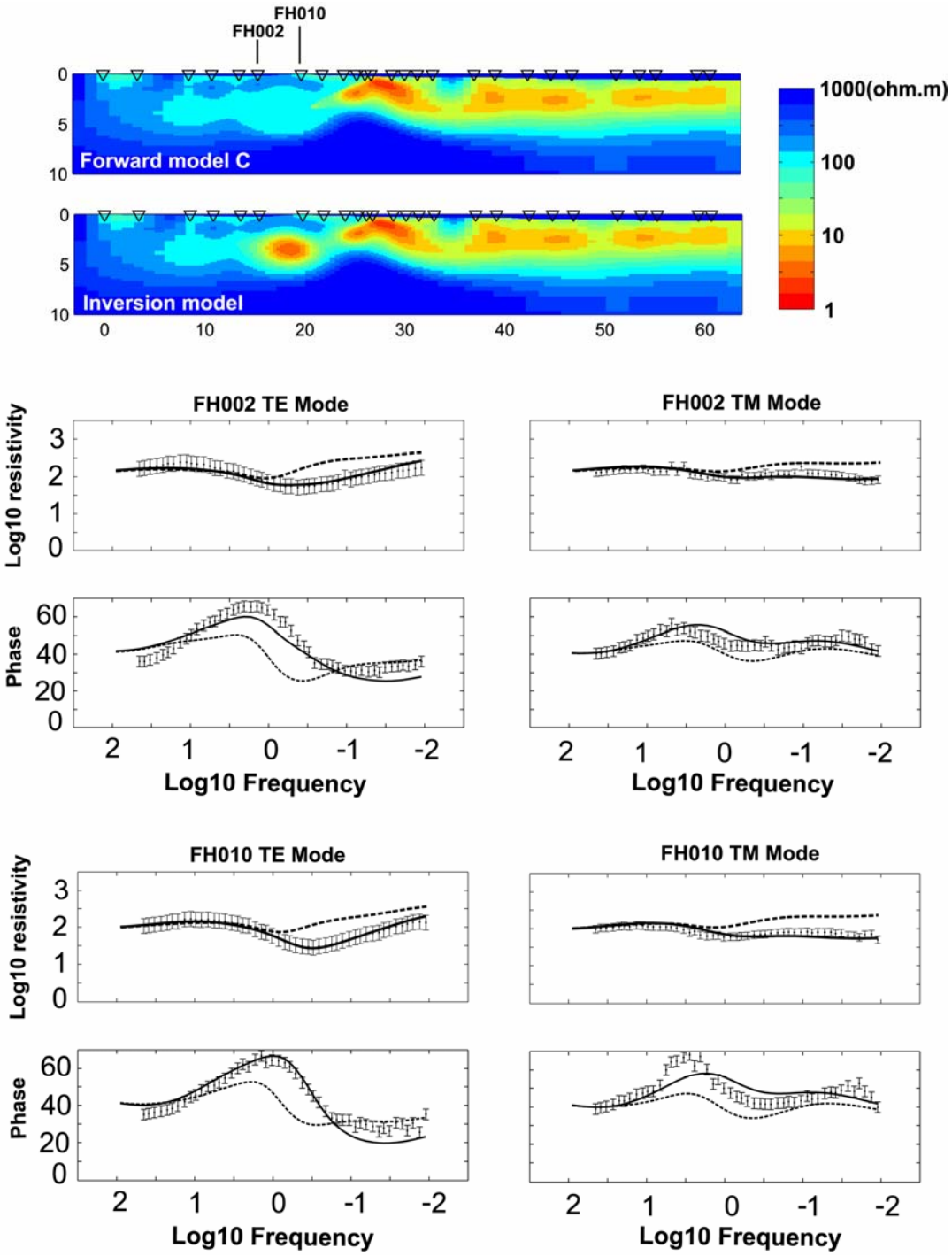

Figure 5-9: Comparison between Forward Model C and the inversion model. Solid line is the responses of the inversion model, dash line is the responses of the forward model C. Dots with error bar is the measured MT data. The r.m.s misfit of station FH002 increases from 1.41 to 3.57. The r.m.s misfit of station FH010 increases from 1.39 to 3.61.

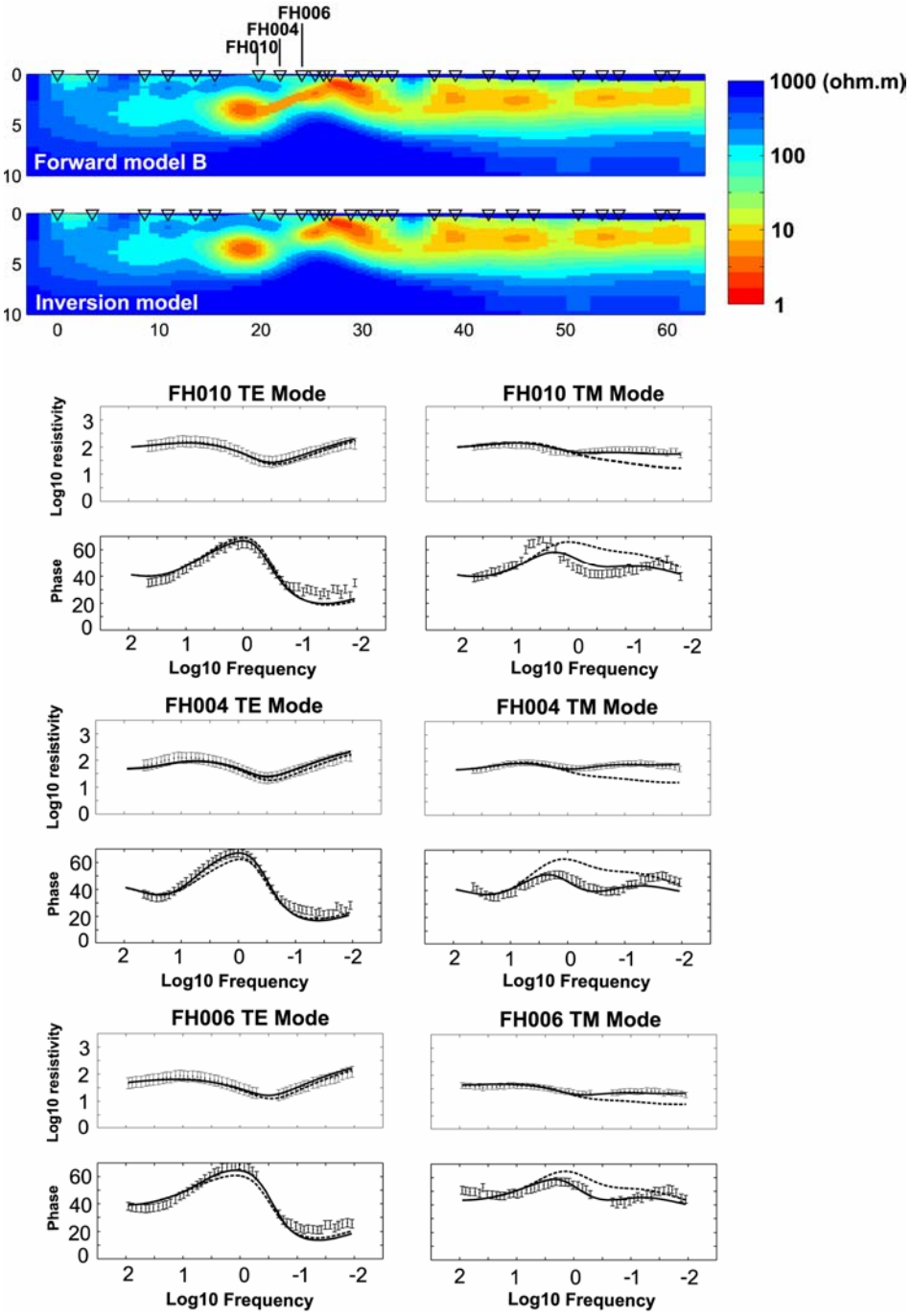

Figure 5-10: Comparison between Forward Model B and the inversion model. Solid line is the responses of the inversion model, dash line is the responses of the forward model B. Dots with error bar is the measured MT data. The r.m.s misfit of station FH010 increases from 1.39 to 2.89. The r.m.s misfit of station FH004 increases from 1.49 to 2.73. The r.m.s misfit of station FH006 increases from 1.35 to 1.97.

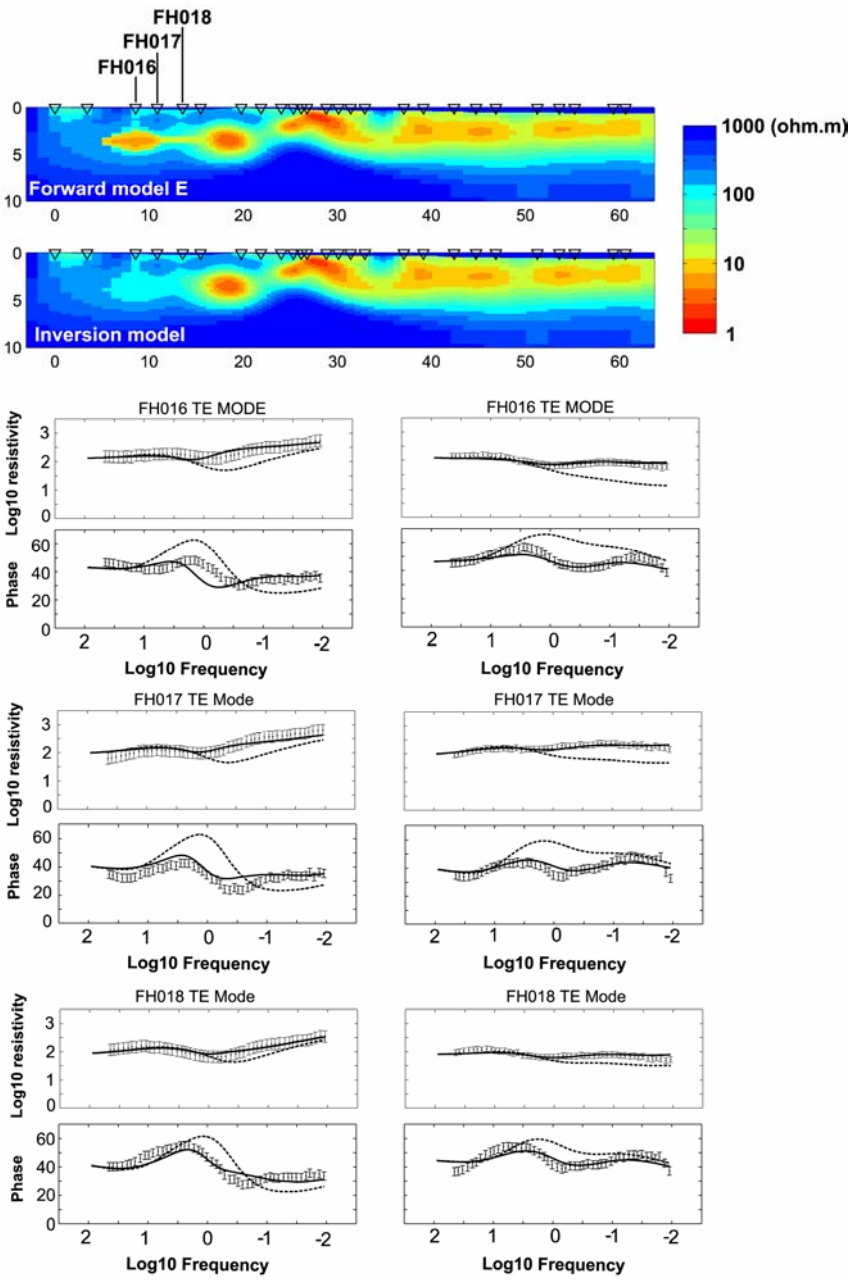

Figure 5-11: Comparison between Forward Model E and the inversion model. Solid line is the responses of the inversion model, dash line is the responses of the forward model E. Dots with error bar is the measured MT data. The r.m.s misfit of station FH016 increases from 1.41 to 3.57. The r.m.s misfit of station FH017 increases from 1.39 to 4.70. The r.m.s misfit of station FH018 increases from 1.49 to 2.32. The decrease of the fit of model responses to data with the decrease of the resistivity of feature E in the forward model shows that the feature E in the inversion model is reliable.

In this chapter, it has been shown that the preferred inversion model has a good fit to the MT data and is adequately smooth. In the next chapter a geological interpretation of the model is described.

Chapter 6

Interpretation of the Foothills MT resistivity model

In this chapter a geological interpretation of the MT inversion model will be presented. It will be shown that the inversion model agrees well with regional geological and geophysical data. Please note that the word 'model' or 'inversion model' used in this chapter refers to the resistivity structure recovered by a 2D MT inversion algorithm.

6.1 Introduction

The MT profile extends from the Alberta Basin, crosses the Rocky Mountain Foothills and terminates on the east side of the Front Ranges (Figure 4-1). Figure 6-1 shows a comparison of the MT inversion model with geological and well log information close to the MT profile. Figure 6-2 shows a seismic time section close to the MT profile, which was provided by Husky Energy.

6.1.1 Regional Geology

The regional geological information (Figure 6-1 (a)) is taken from the Nordegg area cross section of Langenberg and Kubll (2002). This section is located 40–50 km northwest of the MT profile (Figure 4-2).

The eastern part of this cross section shows the stratigraphic sequence in the western Alberta Basin. At the surface, the 600-700 m thick Tertiary Paskapoo Formation is present. Below it are 2800 m of Mesozoic strata, underlain by a ~2000 m thick Paleozoic succession. From the section it can be seen that the undeformed strata dip gently to the west. The Paleozoic succession is primarily composed of marine carbonate sedimentary rocks. The Mesozoic succession is composed of shales, siltstone, sandstones and other clastic sedimentary rocks. Drilling data (Table 6-1) show that the Mesozoic succession in this area is mainly

composed of Cretaceous units with the thickness of Jurassic sedimentary rocks only 100 m.

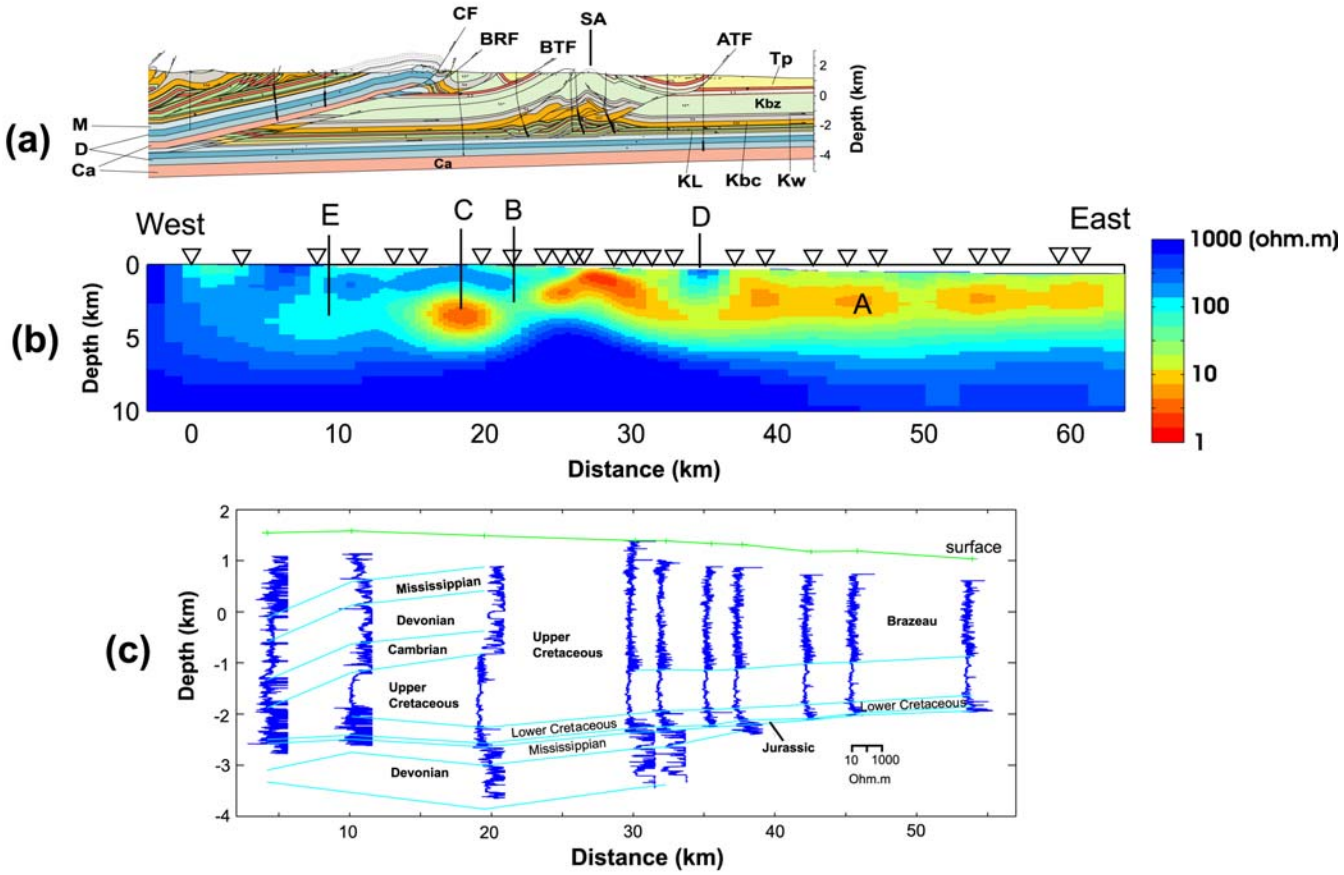

Figure 6-1: Comparison of the geological cross section, MT inversion model and well logs. (a): Nordegg area cross section from Langenberg and Kubll (2002); CF=Coliseum Fault; BRF=Brazeau Range Fault; BTF=Brazeau Thrust Fault; ATF= Ancona Trust Fault; SA= Stolberg Anticline; Tp=Paskapoo Formation; Kw=Wapiabi Formation; Kbc=Blackstone and Cardium Formations; KL=Lower Cretaceous; M=Mississippian; D=Devonian; Ca=Cambrian; (b): A, B, C, D and E denote resistivity features in the MT inversion model that are discussed in this chapter. (c): well data from Alberta Energy and Utility Board (EUB). Geological divisions are based on Geowell General Well Standard Report from EUB; actual data are shown in Table 6-1.

Table 6-1 Geological divisions of well logs (data show the depth of the bottom of the geological units in meters).

Well number	Brazeau Formation	Upper Cretaceous	Lower Cretaceous	Jurassic	Mississippian	Devonian	Cambrian
W1: 00/06-32-035-12W500			20.4	-114	-594.3	-1334.7	-1878.4
			-2497	-2577.5	-3092.8	-3328.1	
W2: 00/11-02-036-12W500				588.4	129.1	-630.2	-1189.8
		-2048.8	-2411.9	-2492.4	-2745.5		
W3: 00/05-13-037-12W500				877.1	410.2	-376.6	-817.5
	-1366.5	-2264.2	-2569.1	-2640.9	-3004.1	-3855.5	
W4: 00/07-09-037-10W500	-1143.6	-1996.1	-2273.8	-2358.2	-2677.1	-3446.4	
W5: 00/10-16-037-10W500	-1132.0	-1932.4	-2247.3	-2328.7	-2646	-3383.6	
W6: 00/10-23-037-10W500	1145.9	-1914.4	-2218.9	-2257.9			
W7: 00/11-25-037-10W500	-1117.7	-1883.2	-2120.2	-2217.2	-2330.7		
W8: 00/08-07-038-09W500	-1012.0	-1811.8	-2087.4	-2115.4			
W9: 00/16-03-038-09W500	-987.2	-1761.2	-1980.7	-2024.2			
W10: 00/08-20-038-08W500	-869.5	-1634.5	-1855.5	-1936.5			

The Brazeau Thrust Fault is located on the west side of the Stolberg Anticline, and is a major thrust fault that dominates the western portion of the cross section. The main frontal ramp of the Brazeau Thrust is interpreted to have

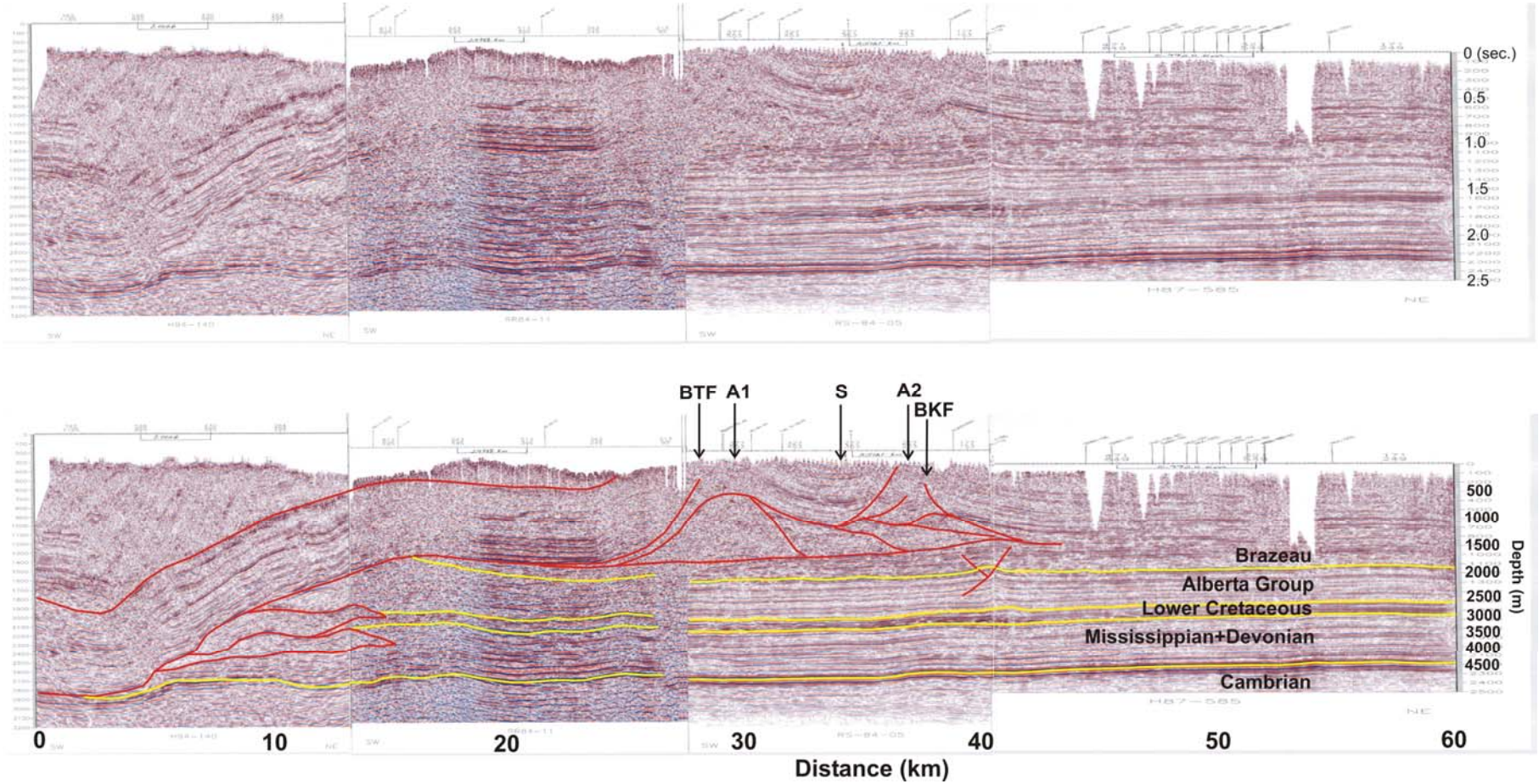

Figure 6-2: Seismic time section. Red lines denote faults; yellow lines denote interface between geological units. BTF=Brazeau Thrust Fault; BKF=Back Thrust Fault; A1=Anticline 1; A2=Anticline 2; S=Syncline. The depth in seismic section is converted from time with the velocity model from Lawton et al. (1996).

climbed from the Cambrian to the lower part of the Tertiary Paskapoo Formation with a displacement of 20 km at the Paleozoic level (Langenberg et al., 2002). The hanging wall of Brazeau Thrust Fault contains almost the whole set of Paleozoic strata, which is around 1700 m thick. The Cretaceous section extends west more than 10 km beneath the thrust sheet. The Ancona Fault is located on the east side of Stolberg Anticline, and a syncline has formed above it.

6.1.2 Well logs and seismic data

Figure 6-1(c) shows ten resistivity well logs close to the MT profile. The well locations are shown in Figure 4-1. The data of strata division of the wells can be seen in Table 6-1. The resistivity logs show that the formation resistivity of Paleozoic strata is generally one to two orders of magnitude higher than Mesozoic strata. Within the Cretaceous succession, below the bottom of the Brazeau formation, the resistivity is obviously lower than in the upper part.

Figure 6-2 shows a seismic time section close to the MT profile. A simple geological interpretation based on drilling data and a gross velocity model is shown on the section. It shows that the Brazeau Thrust Fault in this area climbs up from the top of the Cambrian to the lower part of the Brazeau Formation, then moves horizontally about 12 km and finally rise up to surface at the west side of the Anticline (A1). The strata shortening and accretion developed in the Brazeau formation accounts for the formation of the anticlines (A1 and A2). A syncline (S) can be observed between the anticlines. A detailed comparison with the MT inversion model and seismic section will be presented later in this chapter.

6.2 Comparison with well logs

Figure 6-3 shows a comparison of the resistivity logs in four wells with the resistivity derived from the MT inversion model. The curves from the model contain the main features of the well logs, although they are smoother than the

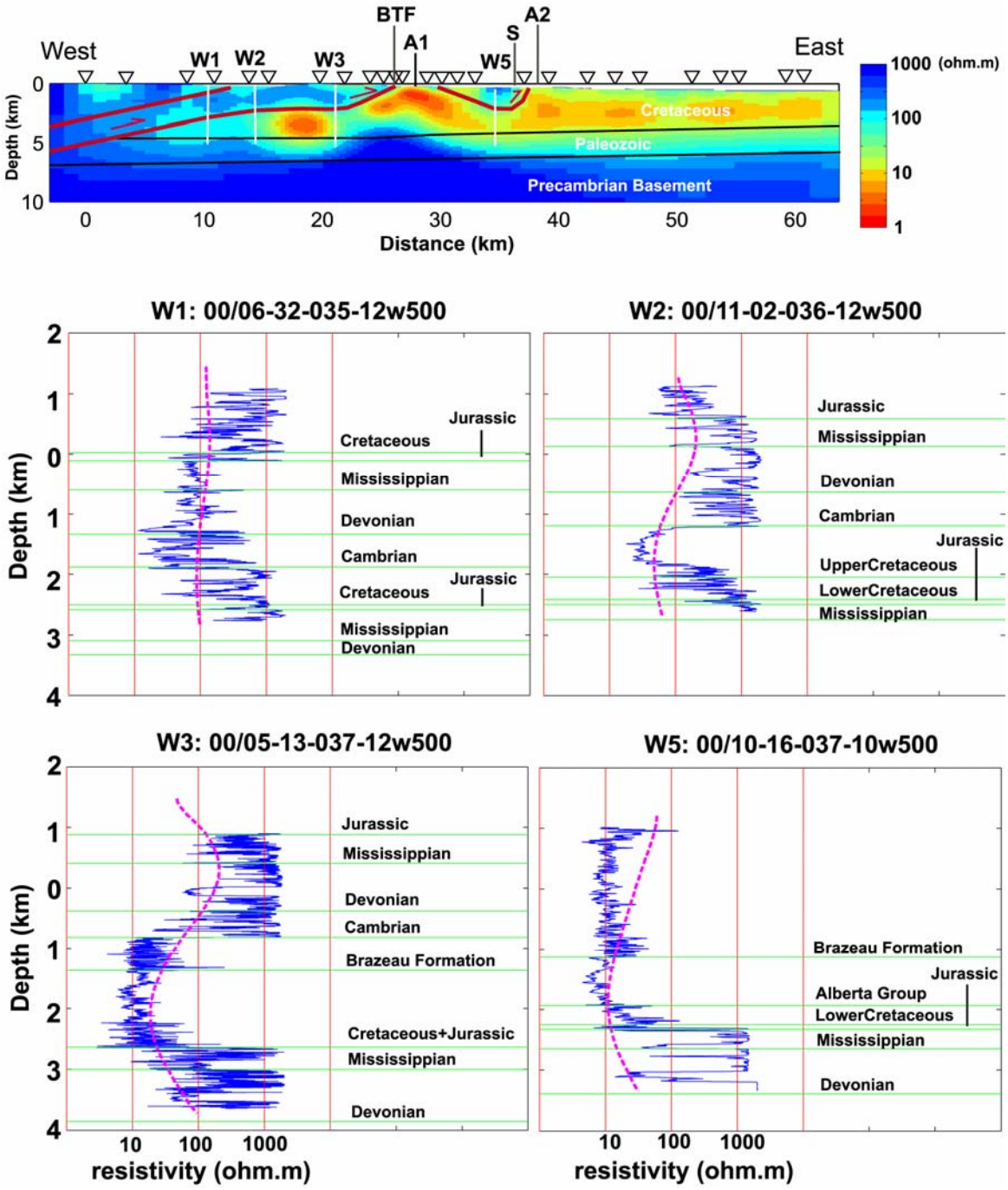

Figure 6-3: Comparison of resistivity logs (solid lines) and the MT derived resistivity model (dashed lines) at four wells. The depth is relative to sea level. White lines in the inversion model show the locations of the wells. BTF=Brazeau Thrust Fault; A1= Anticline 1; A2= Anticline 2; S= Syncline.

resistivity log curves and do not recover the full amplitude of the resistivity variation. This arises from the smoothing imposed in the MT inversion process, and reflects the fact that MT measurements use long spatial wavelengths that average short spatial wavelength variations in electrical resistivity. From the comparison, the lowest resistivity of the model responses are always just above the bottom of the Cretaceous units. This correlation can be used to locate the bottom of the Cretaceous units in the interpretation.

6.3 Interpretation

6.3.1 Alberta Basin

The eastern part of the MT profile is within the Alberta Basin. In the inversion model, the resistivity structure is dominated by a low resistivity layer (Feature A in Figure 6-1 (b)). From distances 40 to 65 km, this low resistivity layer (10 to 50 Ωm) is located above the high resistivity layer (100-1000 Ωm), which dips gently west. The low resistivity layer can be divided into two parts. The upper part has a resistivity 20-50 Ωm and the lower part has a resistivity of 10 Ωm. This feature agrees well with the resistivity structure observed in the resistivity logs, which is controlled by the hydrogeology. The low resistivity Cretaceous strata overly the resistive Paleozoic succession and within the Cretaceous succession the lower part exhibits lower resistivity. Well W5 in Figure 6-3 shows that the lowest resistivity in the inversion model is located just above the base of the Cretaceous, so the base of the Cretaceous can be located using this information. Here the interface between the Cretaceous succession and the Paleozoic succession was interpreted at the bottom of the low resistivity layer. It is around a depth of 3000 m in the east part of the MT profile and can be traced to the west.

The interface between the Paleozoic units and the crystalline basement could also be inferred by locating the top of the highest resistivity layer in the inversion

model, at a depth around 6000 m. This depth agrees well with the geological section of Langenberg and Kubll (2002).

6.3.2 Triangle zone

Figure 6-4 shows a detailed comparison of the inversion model and the seismic time section between distances 20-50 km. A triangle zone can be observed in the seismic section (Figure 6-4 (b)). The basal detachment is close to the bottom of Brazeau Formation. Strata accretion and shortening above the basal detachment has caused the formation of two anticlines (A1, A2) and a syncline (S) between the Brazeau Thrust Fault and the back thrust fault (Figure 6-2).

In the inversion model (Figure 6-4 (a)), the high resistivity layer (located west of BTF) is interpreted as the thrust sheet of the Brazeau Thrust Fault, which contains 1700 m of high resistivity Paleozoic strata. The uplift of the low resistivity layer east of the Brazeau Thrust Fault is interpreted as the anticline A1, which reaches the surface at distance 28-29 km, and then dips west to a depth of 3 km. The high resistivity gap S (feature D in Figure 5-7) has been proven to be a true resistivity structure by forward model D (Figure 5-8), and is interpreted as a syncline and the small uplift of the low resistivity layer east of S is interpreted as the anticline A2. The tension at the top of anticline can cause fractures thus increase permeability and decrease resistivity. The compressive force at the axis of a syncline could decrease the permeability and porosity, and thus increase the resistivity and cause the high resistivity gap S observed in the inversion model. These four resistivity features agree well with the seismic time section (Figure 6-4 (b)).

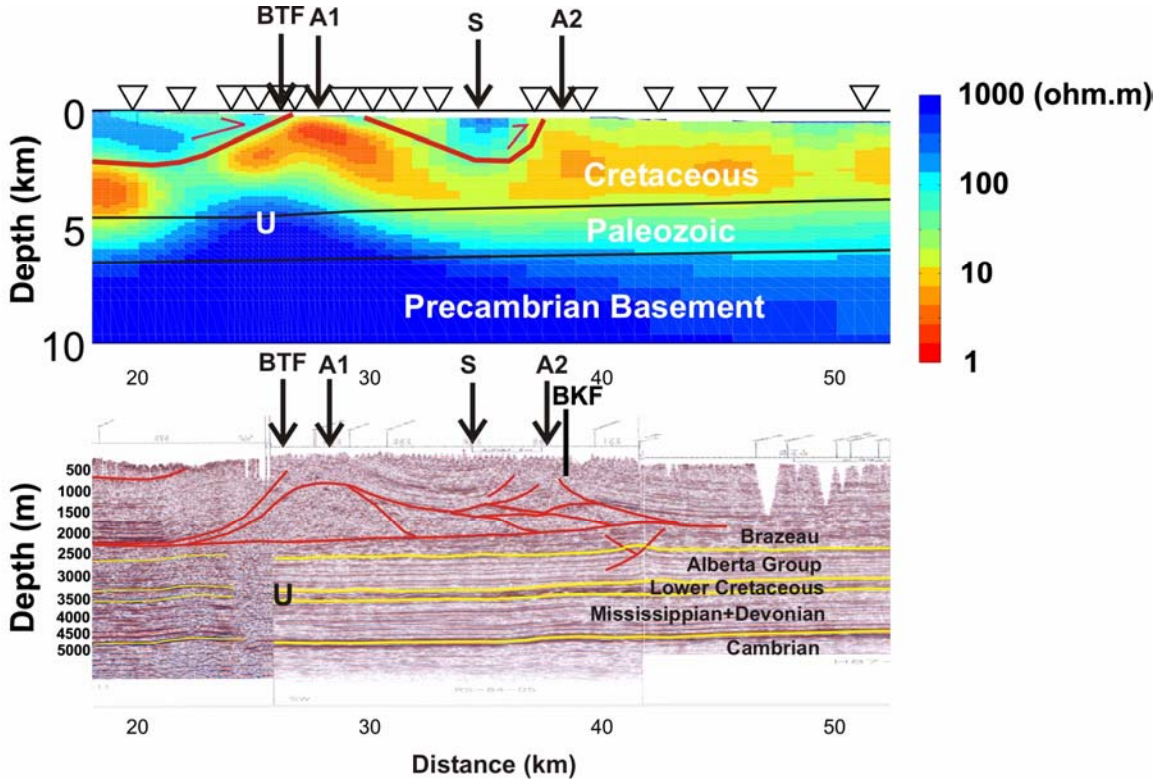

Figure 6-4: Detailed comparison between Inversion model and seismic time section-Triangle Zone. BTF=Brazeau Thrust Fault; BKF=Back Thrust Fault; A1= Anticline 1; A2= Anticline 2; S= Syncline; Red lines denote faults, yellow lines denote interfaces between geological units. The depth in seismic section is converted from time by the velocity model from Lawton et al. (1996).

An uplift of the highest resistivity layer can be observed below the anticline A1 in the inversion model (feature U in the Figure 6-4 (a)). This does not agree with the seismic data. In the seismic section the strata at this location are flat. The synthetic model in Figure 6-5 shows that beneath the low resistivity anticline A1, the resolution of the model is poor. Models with resistivity value of 30 Ωm and 300 Ωm give the same inversion result. So the feature U could be an artifact of the inversion process. Thus a flat base for the Mesozoic succession and the Paleozoic succession is consistent with the MT data.

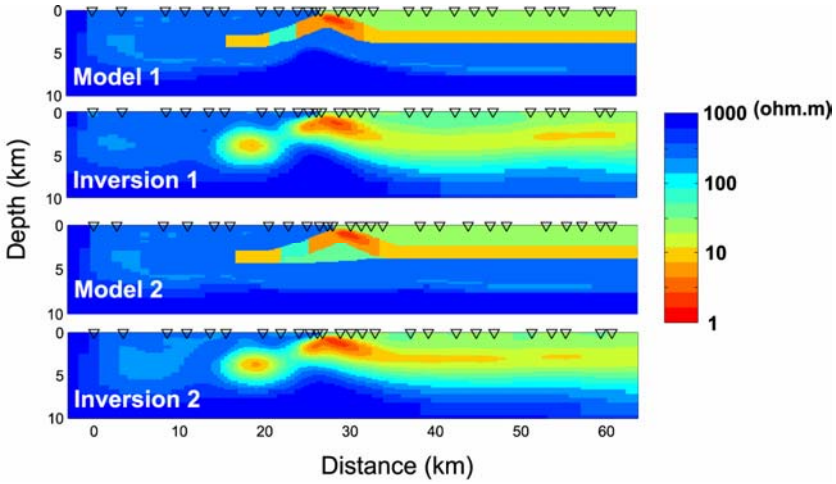

Figure 6-5: Synthetic test for model sensitivity below the low resistivity anticline A1. Different values of resistivity were used in the model beneath the low resistivity anticline. 5% Gaussian noise was added to the forward model responses. The r.m.s. misfits are: model 1: initial: 15.03; final: 0.882; model 2: initial: 11.91; Final: 0.897. The inversion results show that resolution of the model below the anticline A1 is poor.

6.3.3 Brazeau Thrust Fault

As described in the previous section, the resistive layer west of the anticline is the Brazeau thrust sheet, which contains around 1700 m of Paleozoic strata (Langenberg and Kubll, 2002). The low resistivity footwall layer can be traced from the anticline and dips westward beneath the resistive thrust sheet. The top of this low resistivity layer dips westward at an angle of ~30°, in agreement with Langenberg and Kubll (2002). This low resistivity layer is not continuous in the inversion model, and a high resistivity gap (50-70 Ωm) is observed at distance 24-21 km (feature B in Figure 6-6 (a)). The layer becomes low resistivity again west of feature B at distance 21-14 km (feature C in Figure 6-6 (a)). Further west, the resistivity of the footwall layer increases again to above 100 Ωm (feature E in Figure 6-6 (a)). In section 5.5, forward modeling was used to show that feature B, C and E are required by the MT data.

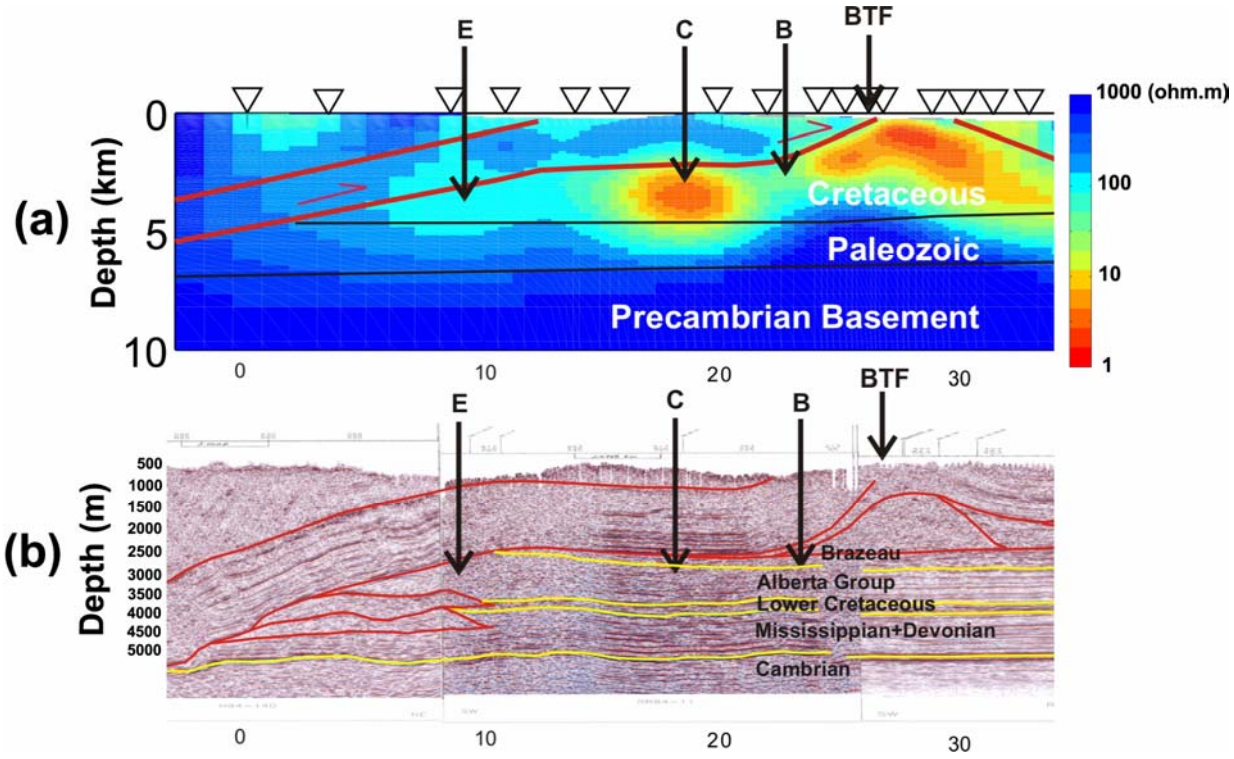

Figure 6-6: Detailed comparison between MT inversion model and seismic time section. BTF=Brazeau Thrust Fault; Red lines denote faults, yellow lines denote interfaces between geological units.

A synthetic inversion was also used to test the sensitivity of the MT data to the angle of the thrust fault. Figures 6-7 show the synthetic resistivity model and the inversion result derived from their responses. The synthetic models (Figure 6-7) have the same resistivity structure except for the angle of the thrust fault. The inversion results show that the inversion model is sensitive to the angle of the low resistivity layer. Thus the angle of the thrust fault (~30°) in the inversion model can be considered reliable. Note that the seismic time section has a larger scale in vertical than horizontal so that the fault dip angle is not real.

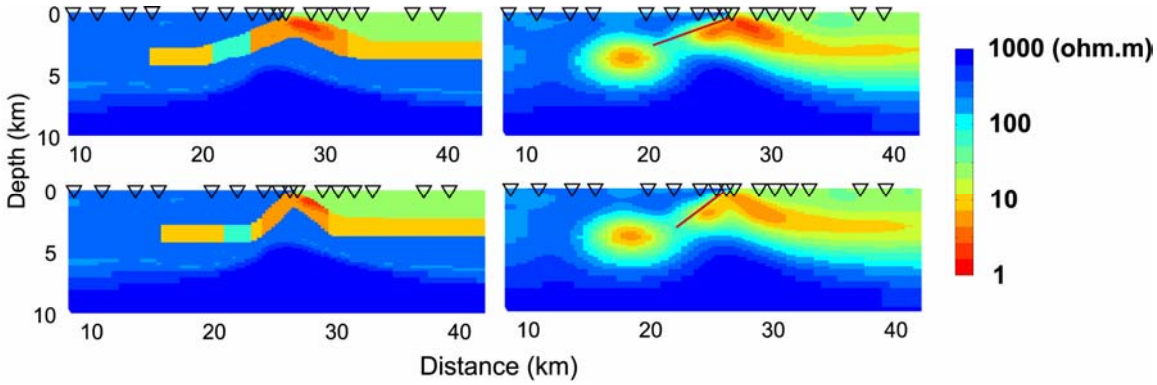

Figure 6-7: Synthetic test for the dip angle of the Brazeau thrust fault. Left-synthetic resistivity models with different dips; Right-inversion results. Noise was added into the forward responses of the synthetic resistivity models before inversion. Red line shows the actual dip angle of the thrust fault in the synthetic models. R.m.s. misfit of 30° dipping anglemodel: initial: 5.03; final: 0.882. R.m.s. misfit of 45° dipping angle model: initial: 14.71; final: 0.985. The inversion results show that the inversion recovers the dip angle of the thrust fault reliably.

According to well logs (W3, W2 and W1 in Figure 6-3) and the seismic data (Figure 6-6), the low resistivity feature C and the high resistivity feature E in the footwall layer are both Cretaceous strata. This appears contradictory, but it is real. The feature C agrees well with well logs W3 and W2, and the well log W1 shows that the resistivity of Cretaceous strata at that part is quite high. This good agreement between the inversion model and well logs proves that the inversion model successfully recover the resistivity structures beneath the thrust sheet. The possible reason for this contradictory phenomenon could be reservoir characteristics (permeability, porosity) change caused by lithological change or the escape of high salinity formation fluid during thrusting.

In the interpretation, the bottom of the thrust sheet and the Cretaceous succession are distinguished by the top and bottom of the low resistivity feature C respectively. 10 Ωm was used to identify the boundary of feature C, thus the top is at a depth of around 2400 m and the bottom is around 4500 m. From well log W3 (Figure 6-7), the bottom of thrust sheet is at a depth of 2313 m and the

bottom of Mesozoic is at a depth of 4137 m (the bottom of Cretaceous is at a depth of 4065 m). The difference of the depth data between the inversion model and well log is within 10%.

The high resistivity feature B observed east of the feature C in the inversion model (Figure 6-6) is somewhat difficult to interpret since there is no well control. Forward modeling (Figure 5-10) showed that this feature is required by the MT data. The reason for the increase of resistivity at this part might be a porosity or permeability decrease of the strata or a decrease of the formation fluid salinity. The porosity or permeability decrease could result from the increased compaction with depth. The escape of high salinity formation fluid during thrusting or mixing with meteoric water could also decrease the formation fluid salinity and thus increase the overall formation resistivity.

The above comparisons show that the resistivity structures in the MT inversion model generally recover the main features in the seismic section (the two anticlines, the syncline, and the geometry of the Brazeau thrust sheet). The top and bottom of the Cretaceous unit beneath the thrust sheet could also be identified by the top and bottom of the Feature C. Thus the resistivity model generally images the geological structure and even gives a better image than the seismic data of the thrust sheet at shallow depth. So in this study the MT resistivity model is useful to the interpretation of the seismic section.

However the resistivity structure is not totally controlled by geological structure, as it is also related to the salinity of formation water and reservoir characteristics. Thus it is reasonable that there are some difference between the resistivity structure and geological structure, and these differences might provide useful hydrogeology or reservoir information for hydrocarbon exploration.

Feature D in the resistivity model (Figure 6-4(a)) shows that the resistivity might be sensitive to permeability and porosity changes. The resistivity increase could

be caused by the permeability and porosity decrease due to the compressive environment of the syncline ‘S’. Meteoric water sinking into the formation could decrease the formation water salinity, and be another reason for an increased resistivity.

The above discussions indicate that the observed resistivity structures are closely related to hydrogeology, since the resisitivity of sedimentary rocks is dominated by the resistivity of the pore fluids. Hydrogeology studies have shown the existence of high salinity formation water in the Foothills and Alberta Basin (Machel et al., 2001). The formation water chemistry shows that the Devonian succession contains two distinct brine types: light brine (100-175 g/l) and heavy brine (200-300 g/l) (Machel et al., 2001). The heavy brine might be the residual Middle Devonian evaporitic brine or could have originated from partial dissolution of thick, laterally extensive Middle Devonian evaporite deposits. The formation of light brine could have resulted from mixing heavy brines with meteoric or metamorphic water (Michael et al., 2003). Hydrogeology studies in south-central Alberta Basin by Anfort et al (2001) suggested that the relatively high salinity formation water in the Lower Cretaceous is formed by the mixing of high salinity Devonian water and meteoric water. The model of Oliver (1986) suggested that the formation fluid in the sediments beneath the thrust sheet could be expelled and flowed toward the foreland basin. This process was called squeegee flow. Machel et al. (2001) provided geochemical evidence that this squeegee flow may have occured in the Devonian aquifers in the Rocky Mountain Foothills. Is it possible that the Devonian brine discharged from Devonian units and has flowed into Cretaceous units through the faults and fractures formed during the thrusting? The high salinity water that now exists in the Cretaceous strata causes the decrease of the formation resistivity. As shown in Figure 6-1(a), the Brazeau formation, which is just above the Wapiabi formation, outcrops at the surface in the Stolberg Anticline, thus meteoric water may sink into it and mix with the brine from the Devonian. This may be a reason why relatively higher resistivities are observed in the Brazeau formation. The fact that heavy brine stays at the bottom

of the aquifer due to its higher density could be another explanation for the observed relatively lower resistivity at the lower part of Cretaceous succession. According to Archie's Law (Archie, 1942), lower porosity and permeability of the strata causes a higher formation resistivity. So the lithological character of the strata could also play a significant role in determining resistivity.

In summary, possible explanations for the observed resistivity structure include:

1. If the whole Cretaceous unit forms a single aquifer, the heavy brine will stay at bottom of the aquifer and causes the observed resistivity structure.
2. If the Brazeau Formation has a lower porosity and permeability, or forms an aquitard, the higher resistivity observed in the Brazeau Formation compared to the Cretaceous unit below it could be hydrogeologically controlled.
3. If the Brazeau Formation has a higher porosity and permeability, then the meteoric water can sink into it easily thus causes the decrease of the formation fluid salinity. This could also increase the resistivity of Brazeau Formation.

The gross porosity of the Cretaceous units can be estimated from its resistivity by Archie's Law. According to Block (2001), a brine with a total dissolved solid value of 300 g/l implies a water resistivity from 0.2 to 0.25 Ωm. Then using a water saturation of 30% from a Cretaceous reservoir and using the 10 Ωm resistivity of the Cretaceous from the MT inversion model, an overall porosity of 22% to 28% can be calculated. The porosity calculated by this way is approximate, but in the early stage of exploration it might be useful.

The above discussion has shown that the inversion model agrees quite well with other geological and geophysical data. This study has shown that structural imaging in the Rocky Mountain Foothills is feasible with magnetotelluric data. In addition, the magnetotelluric data provide complementary information about the hydrogeology.

Chapter 7

Conclusion, discussion, and future work

In this thesis, modern MT exploration has been applied to structural imaging in the Rocky Mountain Foothills. The results have shown that with state-of-the-art of MT methodology, useful structural information can be obtained.

The two-dimensional inversion of the MT data gives a model that agrees well with the regional geology, well logs and a seismic section. The Cretaceous units and the Brazeau Thrust Fault are clearly imaged in the geoelectric model. The bottom of the Cretaceous section could be interpreted at a depth of 3000 m at east end of the profile (in the Alberta Syncline) and 4500 m beneath the thrust sheet, which is within 10% difference of the depth from the well log. The model also gives a good image of the anticline.

Like any geophysical method, MT requires a contrast in material properties to image structures. In the study area, the low resistivity Cretaceous section provides a major contrast in resistivity with the high resistivity Paleozoic section. In other locations, this might not be the case. However, underthrust sedimentary sections are usually lower in resistivity than overthrust carbonates, or older units as demonstrated in other MT studies of similar tectonic settings (Watts and Pince, 1998; Watts et al., 2002).

In the model a high resistivity gap was observed within the Cretaceous low resistivity layer on the west ramp of the anticline, which is not shown on seismic section. This is because the resistivity structure is not totally controlled by geological structure, as it is also related to the salinity of formation water and reservoir characteristics. Possible reasons are porosity and permeability

decrease of the strata, or a decrease of the formation fluid salinity at that location.

In addition to structural imaging, the MT data provide hydrogeology information. The low resistivity feature C in the model not only shows the existence of Cretaceous strata beneath the thrust sheet, but might also indicates that the old high salinity water has not been replaced by meteoric water, which might be a favorable sign for oil and gas migration and accumulation.

In terms of future work, the following tasks should be the focus of future research:

1. To investigate three dimensional structures, it would be useful to make a new MT profile about 10-20 km away and parallel to this profile. The two surveys could constrain along strike changes of the resistivity structure.
2. The large spacing between some MT stations on the profile might give some artifacts in the inversion. Although the key features on the inversion model have been tested by modeling and inversion studies, these gaps may be significant. Some new measurements should be made in these gaps in future.
3. The vertical magnetic field component were only collected at 10 stations and not used in the inversions. A synthetic model should be made to test if the vertical magnetic field data is useful in the structural imaging.

In summary, this study shows that MT can contribute to structural imaging in the Rocky Mountain Foothills. While MT cannot image detailed structure in the same detail as seismic reflection, it can image the structural style and work as a reconnaissance tool in exploration. In addition, it can provide information for reservoir characterization that is complementary to other geophysical methods.

BIBLIOGRAPHY

Abaco, C. I., Lawton, D.C., and Spratt, D. A., 2002, Mapping magnetic properties of post-Wapiabi sandstones from south-central Alberta Foothills, 75th Anniversary of Canadian Society of Petroleum Geologist.

Anfort, S.J., Bachu, S., and Bentley, L.R., 2001, Regional-scale hydrogeology of Upper Devonian-Lower Cretaceous sedimentary succession, south-central Alberta Basin, Canada, AAPG Bulletin, v.85, no.4, p.637-660.

Archie, G.E., 1942, The electric resistivity log as an aid in determining some reservoir characteristics, Trans. Am. Inst. Min. Metall. Petr. Eng., 146, 54-62.

Berdichevsky, M.N., and Dmitriev, V.I., 1976, Distortions of magnetic and electrical fields by near surface inhomogeneities, Acta Geodaet. Geophys. Et Mantanist. Acad. Sci. Hung., v.11, p.447-483.

Berdichevsky, M.N., Dmitriev, V.I., and Pozdnjakova, E.E., 1998, On two-dimensional interpretation of magnetotelluric soundings, Geophys. J. Int., v.133, p.585-606.

Berdichevsky, M., and Dmitriev, V., 2002, Magnetotelluric in the context of the theory of ill posed problems: 12.2 Magnetotelluric in exploration for oil and gas, edited by Keller, G.V., published by Society of Exploration Geophysicists.

Bedrosian, P.A., Unsworth, M.J., and Wang, F., 2001, Structure of the Altyn Tagh Fault and Daxue Shan from magnetotelluric surveys: Implications for faulting associated with the rise of the Tibetan Plateau, Tectonics v. 20, No. 4, p. 474-486.

Block, D., 2001, Water Resistivity Atlas of Western Canada Abstract, paper presented at Rock the Foundation Convention of Canadian Society of Petroleum Geologists, June 18-22, Calgary.

Boerner, D.E., Kurtz, R.D., Craven, J.A., Rondenay, S., and Qian, W., 1995, Buried proterozoic foredeep under the Western Canada Sedimentary Basin, Geology, v.23, No.4, p.297-300.

Boerner, D.E., Kurtz, R.D., Craven, Ross, G.M., and Jones, F.W., 2000, A synthesis of electromagnetic studies in the Lithoprobe Alberta Basement Transect: constraints on Paleoproterozoic indentation tectonic, Can. J. Earth Si., v.37, p. 1509-1534.

Burrowes, A., Marsh, R., Ramdin, H., and Sadler, K., 2003, Alberta's reserves 2002 and supply/demand outlook 2003-2012, Alberta Utility and Energy Board Statistical series 2003-98.

Cagniard, L., 1953, Basic theory of the magneto-telluric method of geophysical prospecting, Geophysics, v.18, p.605-635.

Cantwell, T., and Madden, T.R., 1960, Preliminary report on crustal magnetotelluric measurements, J. Geophys. Res., v.65, No.12, p.4202-4205.

Chave, A.D., and Smith, T.J., 1994, On electric and magnetic galvanic distortion tensor decompositions, J. geophys. Res. v.99, p. 4669-4682.

Christopherson, K.R., 1991, Applications of Magnetotellurics to petroleum exploration in Papua New Guinea: A model for frontier areas, The Leading Edge Of Exploration, April, 1991.

Christopherson, K.R., 2002, EM in the 21st Century-Looking for oil, gas and water, 16th Workshop on Electromagnetic Induction in the Earth, Santa Fe.

deGroot-Hedlin, C., and Constable, S.C., 1990, Occam's Inversion to generate smooth, two-dimensional models from magnetotelluric data, Geophysics, v.55, p.1613-1624.

deGroot-Hedlin, C., 1991, Short note: Removal of Static shift in tow dimensions by regularized inversion, Geophysics, v.56, p.2102-2136.

Fox F.G., 1959, Structure and Accumulation of Hydrocarbons in Southern Foothills, Alberta, Canada, Bulletin of the American Association of Petroleum Geologists, v. 43, p. 992-1025.

Gabrielse, H. and Taylor, G.C., 1982, Geological maps and cross-sections of the Cordillera from near Fort Nelson, British Columbia to Gravina Island, southeastern Alaska. Geological Survey of Canada, Open File Report 864.

Gamble, T.D., Goubau, W.M., and Clark, J., 1979, Magnetotelluric with a remote magnetic reference, Geophysics, v.44, p.53-68.

Geological Map of Alberta, 1999, scale: 1:1,000,000, Alberta Geological Survey/Alberta Energy and Utility Board

Gordy, P.L. and Frey, F.R. 1975, Structural cross section enclosure, In: Structural Geology of the Foothills between Savanna Creek and Panther River, S.W. Alberta, Canada, H.J. Evers and J.E. Thorpe (eds.), Guidebook, Canadian Society of Petroleum Geologists and Canadian Society of Exploration Geophysicists.

Greiner, G., and Chi, B., 1995, chapter-Canada, Regional petroleum geology of the world-part 2, published by Gebrüder Borntraeger, Berlin, Stuttgart, p.279-334.

Groom R.W., and Bailey, R.C., 1989, Decomposition of magnetotelluric impedance tensor in the presence of local three-dimensional galvanic distortion, J. Geophys. Res. v.94, p.1913-1925.

Groom, R.W., and Bahr, K., 1992, Correstion of near surface effects: Decomposition of magnetotelluric impedance tensor and scaling correction for regional resistivities, Geophysics, v.13, p.341-380.

Hoversten, G.M., Constable, S.C., and Morrison, H.F., 2000, Marine magnetotellurics for Base-of –salt mapping: Gulf of Mexico field test at the Gemini Structure., Geophysics, v.65, No.5, p.1476-1488.

Hutton, V.R.S., Gough, D.I., Dawes, G.J.K., and Travassos, 1987, Magnetotelluric soundings in the Canadian Rocky Mountains, Geophys. J.R. Astr. Soc. v.90, p.245-263.

Jones, P.B. 1982. Oil and gas beneath east-dipping underthrust faults in the Alberta Foothills. In: Studies of the Cordilleran Thrust Belt. R.B. Powers (ed.). Rocky Mountain Association of Geologists, p. 61-74.

Jones, A.G. and Jodicke, H., 1984, Magnetotelluric transfer function estimation improvement by a coherence-based rejection technique, paper presented at 54th Annual International Meeting, Society of Exploration Geophysicists, Atianta, Dec. 2-6, 1984.

Jupp D.L.P., and Vozoff, K., 1977, Two dimensional magnetotelluric inversion, Geophysical Journal of Royal Astronomical Society, v.50, p.333-352.

Langenberg, C.W., Beaton, A., and Berhane, H., 2002, Regional evaluation of the coalbed methane potential of the Foothills/Mountains of Alberta (second edition), EUB/AGS Earth Science Report 2002-05.

Lagenberg, C.W., and Kubll, T. E., 2002, Cross Section: Nordegg Area, Regional Evaluation of the Coalbed Methane Potential of the Foothills/Mountains of Alberta (second Edition), published by Alberta Geological Survey.

Larsen, J.C., 1977, Removal of local surface conductivity effects from low frequency mantle reponse curves, Acta Geodaet. Geophys. Et Mantanist. Acad. Sci. Hung., v.12, p.183-186.

Lawton, D.C., Sukaramongkol, C., and Spratt, D.A., 1996, Seismic characterization of a “compound tectonic wedge” beneath the Rocky Mountain foreland basin, Alberta, Bulletin of Canadian Petroleum Geology, v.44, No.2, p.258-268.

Ledo, J. and Jones, G., 2001, Regional electrical resistivity structure of the southern Canadian Cordillera and its physical interpretation, Journal of Geophysical Research, v.106, No.12, p.30755-30769.

Madden, T.R. and Nelson P., 1964, A defense of Cagniard's magnetotelluric method, in Magnetotelluric Methode, edit by Vozoff, K., Society of Exploration Geophysicists., Tulsa.

Machel, H.G., Buschkuehle, B.E., and Michael, K., 2001, Squeegee flow in Devonian carbonate aquifers in Alberta, Canada, Cidu. R. (ed.), Water-Rock Interaction, v.1 Proceedings of the Tenth International Symposium on Water-Rock-Intercation WRI-10, Villasimius, Italy, p.631-634.

Mackie R.L., Madden, T.R., and Wannamaker, P.E., 1993, Three-dimensional magnetotelluric modeling using difference equations—Theory and comparisons to integral equation solutions, Geophysics, v.58, No.2, p.215-226.

Mackie, R. L. and Rodi, W., 1996, A nonlinear conjugate gradients algorithm for 2-D magnetotelluric inversion: paper presented at Fall Meeting of the American Geophysical Union, San Francisco, Califonia.

Matsuo K., and Negi, T., 1999, Oil exploration in difficult Minami-Noshiro area-Park two: Magnetotelluric Survey, The Leading Edge Of Exploration, December 1999.

McNeice, G.W., and Jones, A.G., 2001, Multisite, multifrequency tensor decomposition of magnetotelluric data, Geophysics, v.66, No.1, p.158-173.

Michael, K., Machel, H. G., and Bachu, S., 2003, New insight into the origin and migration of brines in deep Devonian aquifers, Alberta, Canada, Journal of Geocheminal Exploration, v. 80, p.193-219.

Oldenburg, D.W., 1979, One dimensional inversion of natural source magnetotelluric observations, Geophysics, v.44, p.1218-1244.

Oliver, J., 1986, Fluids expelled tectonically from orogenic belts: their role in hedrocarbon migration and other geological phenomena, Geology, v.14, p.99-102.

Park, S.k., Thompsom, S.C., Rybin, A., Batalev, V., and Bielinski, 2003, Structural constraints in neotectonic studies of thrust faults from the magnetotelluric method, Kochkor Bain, Kyrgyz Republic, Tectonics, v.22, No.2, p.1013.

Parker, R.L., 1980, The inverse problem of electromagnetic induction: Existence and construction of solutions based on incomplete data, J. Geophys. Res. v.85, No.B8, p.4421-4428.

Parkinson, W.D., The influence of continents and oceans on geomagnetic variations, Geophysical Journal of Royal Astronomical Society, v.6, No.4 , 441-449, 1962.

Peirce, J.W., Sander, S., Charpters, R. A., and Lavoie, V., 2002, Turner valley, Canada-A case history in contemporary airborne gravity, 2002 Canadian Society of Exploration Geophysicists National Convention Abstract.

Pellerin, L., and Hohmann, G.W., 1990, Transient electromagnetic inversion: A remedy for magnetotelluric static shifts, Geophysics, v.55, No.9, p. 1242-1250.

Picha, F.J., 1996, Exploration for hydrocarbon under thrust belts – a challenging new frontier in the Carpathians: AAPG Bulletin, v.80, No.10, p.1547-1564.

Price, A.T., 1962, The theory of magnetotelluric methods when the source field is considered, J. Geophys. Res., v.67, No.5, p. 1907-1918.

Price R.A., 1994, Cordilleran Tectonics and the Evolution of the Western Canada Sedimentary Basin, Geological Atlas of the Western Canada Sedimentary Basin - Chapter 2, published by Canadian Society of Petroleum geologist and the Alberta Research Council.

Reddy, I.K., and Rankin, D., 1971, Magnetotelluric measurements in central Alberta, Geophysics, v.36, No.4, p.739-753.

Richard, M.L., Schmucker, U., and Steveling, E., 1982, Entzerrung der Impedanzkurven von magnetotellurischen Messungen in der Schewäbischen Alb, in Protokol über das Kolloquium “Elektromagnetische Tiefenforschung,” 27-40.

Rodi, W., and Mackie, R., 2001, Nonlinear conjugate gradient algorithm for two-dimensional magnetotelluric inversion, Geophysics, 66, No.1, p.174-187.

Rokityansky, I.I., 1961, On the application of magnetotelluric method to anisotropic and inhomogeneous masses, Izvestia, v.11, p.1607-1613.

Smith, J.T., and Booker, J.R., 1991, Rapid inversion of two and three-dimensional magnetotelluric data, J. Geophys. Res., v.96, p.3905-3922.

Sternberg, B.K., Washburne, J.C., and Pellerin, L., 1988, Correction for the static shift in magnetotellurics using transient electromagnetic soundings, Geophysics, v.53, No.11, p.1459-1468.

Stockmal, G.S., Osadetz, K.G., Lebel, D., and Hannigan, P.K., 2001, Structure and hydrocarbon occurrence, Rocky Mountain Foothills and Front Ranges, Turner Valley to Waterton Lakes, Alberta, Geological Survey of Canada (Calgary) Open File 4111.

Swift, C.M., 1967, A magnetotelluric investigation of a electric conductivity anomaly in the southwestern United States, PHD thesis, Mass. Inst. Tech.

Torres-Verdin, C. and Bostick, F.X., 1992, Principles of spatial surface electric field filtering in magnetotellurics: Electromagnetic array profiling (EMAP), Geophysics, v.57, No.4, p.603-622.

Telford, W.M., Geldart, L.P., and Sheriff R.E., 1990, Applied Geophysics, Second Edition, published by the Press Syndicate of the University of Cambridge.

Tikhonov, A.N., 1950, Determination of the electrical characteristics of the deep state of the earth's crust, Dok. Akad. Nauk, USSR, v.73, No.2, 295-297.

Tikhonov, A.N., 1965, Mathematical basis of the theory of magnetotelluric soundings, USSR Comput. Math. Math. Phys,, v.5, p.207.

Tikhonov, A.N., and Arsenin, V.Y., 1977, Solutions of ill-posed problems, published by V. H. Winston and Sons.

Vestrum, R.W., and Lawton, D.C., 1999, Anisotropic depth migration: reducing lateral-position uncertainty of subsurface structures in the thrust-belt environment, Society of Exploration Geophysicist Annual Meeting, Houston, Texas.

Vozoff, K., Hasegawa, H., and Ellis, R.M., 1963, Results and limitation of magnetotelluric surveys in simple geologic situation, Geophysics, v.28, p.778

Vozoff, K., and Ellis, R., 1966, Magnetotelluric measurements in southern Alberta, Geophysics, v.31, No.6, p. 1153-1157.

Vozoff, K., 1991, The Magnetotellruic Method, Chapter 8, Electromagnetic method in applied geophysics-Applications part A and part B, edit by Corbett, J.D., published by Scociety of Exploration Geophysicists, p.641-711.

Wait, J.R., 1954, On the relation between telluric currents and the Earth's magnetic field, Geophysics, v.19, p.281-289.

Wannamaker, P.E., Hohmann, G.W., and Ward, S.H. 1984, Magnetotelluric responses of three-dimensional bodies in layered Earths, Geophysics, v.49, p.1517-1533.

Watts, M.D., and Pince, A., 1998, Petroleum exploration in overthrust area using magnetotelluric and seismic data, SEG expanded abstract, New Orleans.

Watts M.D., Alexandros, S., Eleni, K., and Mackie, R., 2002, Magnetotelluric applied to sub-thrust petroleum exploration in Northern Greece, Work package report to European Commission Research Directorate-General.

Wright G.N., McMechan M.E., and Potter D.E.G., 1994, Structure and Architecture of the Western Canada Sedimentary Basin, Geological Atlas of the Western Canada Sedimentary Basin, Chapter 3, published by Canadian Society of Petroleum geologist and the Alberta Research Council.

Wu, F.T., 1968, The inverse problem of magnetotelluric sounding, Geophysics, v.33, No.6, p.972-979.

Yan, L., and Lines, L.R. 2001, Seimic imaging and velocity analysis for an Alberta Foothills seismic survey, Geophysics, 66, p. 721-732

Zhang, P., King, A., and Watts, D., 1998, Using Magnetotellurics for Mineral Exploration, SEG Workshop on MT in Mining: Abstract #6.